# Modelling Laser-Plasma Interactions for the Next Generation of High-Power Laser Experiments







Alex Savin

Lady Margaret Hall

University of Oxford

A thesis submitted for the degree of

*Doctor of Philosophy*

Trinity Term 2019

This thesis is dedicated to:
my parents, who kept me sane;
and James, who kept me smiling.

# Acknowledgements

There are several people I want and need to thank for all of their support over the past few years that led to me writing this thesis. First of all, I'd like to thank my supervisor, Peter Norreys, for his support, guidance, and the opportunities he's afforded me over the course of both my undergraduate and postgraduate studies. Peter introduced me to the world of scientific research when I was still a woefully naive and inexperienced undergraduate student at Lady Margaret Hall and it is due to his encouragement and support that I have had the good fortune to pursue research as a DPhil student.

While speaking of LMH, I want thank my tutors, who later became my teaching colleagues: Todd, Niranjan, and Gianluca who all have amusing stories from teaching me (I supposedly look utterly gormless when I'm confused) have been fantastic informal advisers and colleagues. The opportunity they gave me to teach the course I studied as an undergraduate to the next generation of LMH physicists led to some of my fondest memories (and most popular Facebook posts!) of my time in Oxford.

I'd also like to acknowledge the members of my research group: Ramy, Marko, Robin, and Ben, for all of the advice, insights and good humour they brought to my time working with them. Past members, in particular Luke and Kevin have been a constant support; without their impromptu pub trips and professional advice I would have not enjoyed my time here anywhere near as much as I did.

Outside of my group, Olly and Gabriel have been the best friends one could ask to work with. Despite our incredibly chaotic travel arrangements we have managed, over the past three years, to keep tabs on one another, travel around the world together and, most commonly, trade stories and offer advice over a pint[1].

[1] or several

Others I've collaborated with, Charlotte, Laura, both Toms, Patrick and the UCSD crew have brought an enormous wealth of advice, both professional and personal, and fun to my time researching in Oxford. For that I am immensely grateful.

Away from science, there are a few other people that must be mentioned. Dean kept me sane during some of the less fruitful periods of research - our "interdepartmental collaboration meetings" drinking coffee and eating cake in St. John's were often the highlight of the working week.

Francine and Rob, who have been the best of friends for my entire time in Oxford, have endured the overwhelming brunt of my jet-lagged ravings and frustrations when they've occurred. More than any other of my friends, I have been exceptionally lucky to have them on hand to rant at, laugh with, and generally enjoy our shared amusement with the world.

Thanks must go to my family who have been an unwavering bedrock of support. My parents, Ann and Dave, who bravely[2] agreed to proof-read this thesis and have had my back in every endeavour, no matter how foolhardy, I've ever pursued. Possibly unconventionally, an honourable mention must go to the "Dog Savins": Chewie and Monty who have always brought a smile to my face and made me instantly forget anything that might be troubling me. Chewie, who regularly "helped" with my studies and research by sitting on whatever I was writing or reading; and Monty, who recently decided to claim my thesis as his own in the most caninely territorial way imaginable.

Finally, to James. From meeting him at the Central Laser Facility in the first few weeks of my DPhil studies to today, he has been my most enthusiastic supporter[3], and my best friend. More than anything else, meeting him has been the best moment of my time in Oxford as a postgraduate and I can't wait to support him in the same unwavering way he has supported me[4].

[2]and possibly foolishly

[3]usually expressed with an unholy quantity of cookies

[4]Disclaimer: maybe I can wait... He's the next to write a thesis and I'm not sure I can go through this again!

# Abstract

Investigating new regimes of laser-plasma interactions requires advances in at least two technologies: targets and laser systems. Exploring these regimes includes developing diagnostics to obtain more information about complex systems such as inertial confinement implosions and constructing models that consider entirely novel and unexplored phenomena.

This thesis initially considers implementing state-of-the-art "mid-density" targets made of foam on current petawatt-class laser systems; particularly the application of foams to ion acceleration. It is highlighted that foam targets potentially pave the way for laser systems to realise collisionless shock acceleration as a high energy quasimonoenergetic ion source. A theoretical approach modelling the predicted energy distribution function for shock-accelerated ions is presented with both classical and relativistic formulations. The full, albeit narrow, parameter space for collisionless shock acceleration is mapped and it is shown that there are several pre-existing laser systems that could realise high-energy narrow-band proton beams.

Impending multipetawatt laser systems are then considered but it is immediately highlighted that the absorption processes in this new regime may not be fully understood. Therefore, the thesis segues into developing a theory that models absorption in the newly dubbed "post-ponderomotive" regime. One absorption mechanism, the Zero Vector Potential process is given a complete description, the predictions of which are validated through numerical simulations.

This discussion then considers the limit of the post-ponderomotive regime where quantum electrodynamic effects are predicted to be perturbations. The theory is modified to include the effects of electron-positron pair production and, again, a simulation campaign verifies the theory.

Applications of the Zero Vector Potential mechanism to coherent x-ray generation are also explored, and in particular their potential use generating warm dense matter. Finally, given that no scientific hypothesis can be considered valid until it has been tested through experiment, three experimental designs are proposed that could test the theories and hypotheses presented herein.

# Contents

**List of Publications** **v**

**List of Figures** **vii**

**List of Tables** **ix**

**List of Symbols and Abbreviations** **xi**

**1 Introduction** **1**

1.1 Laser-Plasma Interactions . . . . . 2
1.2 Low-Density Solid Laser Targets . . . . . 3
1.3 Multi-Petawatt Laser Systems . . . . . 5
1.4 Modelling Laser-Plasma Interactions . . . . . 9
1.4.1 Hydrodynamics Codes . . . . . 10
1.4.2 Particle-in-Cell Codes . . . . . 12
1.5 Role of the Author & Collaborators . . . . . 14
1.6 Structure of the Thesis . . . . . 16
1.7 Summary . . . . . 18

**2 Laser Energy Absorption & Laser-Driven Particle Acceleration** **19**

2.1 Laser Energy Absorption in Non-Ionised Material . . . . . 20
2.2 Defining a Plasma . . . . . 22
2.2.1 The Plasma Frequency . . . . . 22
2.2.2 The Debye Length . . . . . 23
2.2.3 The Plasma Parameter . . . . . 24
2.3 Inverse Bremsstrahlung . . . . . 25
2.3.1 The Ponderomotive Energy . . . . . 26
2.3.2 Electron-Ion Collision Frequency . . . . . 26
2.4 Resonance Absorption . . . . . 29

2.4.1 The Critical Density Surface . . . 29
2.4.2 Reflection of an Obliquely Incident Pulse . . . 30
2.4.3 Transferring Energy from Laser to Plasma . . . 32
2.4.4 Anharmonic Resonant Absorption of Femtosecond-Class Pulses 35
2.5 Brunel Heating (a.k.a. Vacuum Heating) . . . 36
2.6 Relativistic $\vec{j} \times \vec{B}$ Heating . . . 39
2.6.1 Classical Ponderomotive Force . . . 39
2.6.2 Relativistic Ponderomotive Force . . . 41
2.7 High Harmonic Generation . . . 42
2.8 Laser-Driven Ion Acceleration . . . 45
2.8.1 Target Normal Sheath Acceleration . . . 46
2.8.2 Radiation Pressure Acceleration . . . 48
2.8.3 Breakout Afterburner . . . 50
2.9 Summary . . . 51

**3 Particle Acceleration in "Mid-Density" Plasma 53**
3.1 Collisionless Shock Acceleration . . . 54
3.1.1 Comparing Experimental Data of Radiation Pressure Acceleration to Collisionless Shock Acceleration . . . 54
3.1.2 A Model for Collisionless Shock Acceleration . . . 56
3.2 Modelling Electrostatic Shocks with a Sagdeev Potential . . . 59
3.3 Obtaining the Energy Distribution from Collisionless Shock Acceleration 66
3.3.1 Non-Relativistic Distribution . . . 68
3.3.2 Relativistic Distribution . . . 69
3.4 Mapping the Parameter Space of Collisionless Shock Acceleration . . 73
3.5 Proposed Measurement of Collisionless Shock Acceleration . . . 76
3.5.1 Target Parameters . . . 76
3.5.2 Laser Parameters . . . 79
3.5.3 Diagnostics . . . 79
3.5.4 Target Chamber & Campaign Design . . . 80
3.6 Summary . . . 82

**4 Beyond the Ponderomotive Regime - the Zero Vector Potential Absorption Mechanism 85**
4.1 The Post-Ponderomotive Regime . . . 86
4.2 Propagating Vector Potential "Zeroes" . . . 87
4.3 Interaction of Electrons with Vector Potential "Zeroes" . . . 93

4.3.1 Generating Fast Electrons . . . 93
4.3.2 Electron Energy Scaling Relations . . . 95
4.3.3 N-Dimensional Energy Scaling . . . 98
4.4 Numerical Validation of the Zero Vector Potential Theory . . . 99
4.4.1 Simulation Setup . . . 99
4.4.2 High-Momentum Phase-Space Spikes . . . 101
4.4.3 Energy Scaling Relations . . . 107
4.5 Efficiency of the Zero Vector Potential Mechanism . . . 110
4.6 Proposed Measurement of Zero Vector Potential Absorption . . . 113
4.6.1 Target Parameters . . . 114
4.6.2 Laser Parameters . . . 115
4.6.3 Diagnostics . . . 115
4.6.4 Target Chamber & Campaign Design . . . 115
4.7 Summary . . . 117

**5 Applications and Extremes of the Zero Vector Potential Mechanism 119**
5.1 Relativistic Generalisation of the Zero Vector Potential Mechanism . 120
5.2 Entering a Quantum Electrodynamic Regime . . . 122
5.2.1 Radiation Reaction . . . 123
5.2.2 Pair Production – the Breit-Wheeler Process . . . 124
5.2.3 Alternative Routes to Pair Production – the Trident and Bethe-Heitler Processes . . . 126
5.3 Combining ZVP & QED . . . 127
5.4 New Energy Scaling . . . 128
5.5 Numerical Validation of the QED-ZVP Model . . . 132
5.5.1 Simulation Setup . . . 133
5.5.2 Extracted Energy Scaling . . . 134
5.6 Exploiting High-Intensity HHG XUV Radiation . . . 139
5.6.1 Target Profile . . . 140
5.6.2 Harmonic Profile . . . 140
5.6.3 Hydrodynamics Simulations . . . 141
5.7 Proposed Measurement of QED-augmented ZVP Absorption . . . 143
5.7.1 Target Parameters . . . 144
5.7.2 Laser Parameters . . . 145
5.7.3 Diagnostics . . . 145
5.7.4 Target Chamber & Campaign Design . . . 146

5.8 Summary . . . . . 147

**6 Conclusions** **148**

6.1 Summary of Results . . . . . 148

6.2 Future Work . . . . . 152

**A Derivations in Full** **155**

A.1 Equation 1.19: Velocity calculated for PIC codes via Leapfrogging . . 155

A.2 Resonant Absorption - Section 2.4 . . . . . 157

A.3 Vacuum Heating - Section 2.5 . . . . . 162

A.4 Integrating the Error Function - Section 3.2 . . . . . 163

A.5 Combination of Relativistic Velocities - Section 3.3.2 . . . . . 163

A.6 Equation 5.7 - The Headlight Effect . . . . . 164

A.7 Equation 5.15 - The Proper Time Interval . . . . . 165

**References** **167**

# List of Publications

1. M. W. Mayr, L. Ceurvorst, M. F. Kasim, J. D. Sadler, B. Spiers, K. Glize, **A. F. Savin**, N. Bourgeois, F. Keeble, A. J. Ross, D. R. Symes, R. Aboushelbaya, R. A. Fonseca, J. Holloway, N. Ratan, R. M. G. M. Trines, R. H. W. Wang, R. Bingham, L. O. Silva, P. N. Burrows, M. Wing, P. P. Rajeev, P. A. Norreys. Wakefields in a cluster plasma, *Phys. Rev. Accel. Beams*, accepted for publication.

2. R. Aboushelbaya, K. Glize, **A. F. Savin**, M. Mayr, B. Spiers, R. Wang, J. Collier, M. Markland, R. M. G. M. Trines, R. Bingham, P. A. Norreys. Orbital angular momentum coupling in elastic photon-photon scattering, *Phys. Rev. Lett.*, **123**, 113604 (2019).

3. J. D. Sadler, Y. Lu, B. Spiers, M. W. Mayr, **A. Savin**, R. H. W. Wang, R. Aboushelbaya, K. Glize, R. Bingham, H. Li, K. A. Flippo, P. A. Norreys. Kinetic simulations using fusion ignition with hot-spot ablator mix, *Phys. Rev. E*, **100**, 033206 (2019).

4. **A. F. Savin**, A. J. Ross, R. Aboushelbaya, M. W. Mayr, B. Spiers, R. H.-W. Wang, P. A. Norreys. Energy absorption in the laser-QED regime, *Sci. Rep.*, **9**, 8956 (2019).

5. R. Aboushelbaya, **A. F. Savin**, L. Ceurvorst, J. Sadler, P. A. Norreys, A. S. Davies, D. Froula, A. Boyle, M. Galimberti, P. Oliveira, B. Parry, Y. Katzir, K. Glize. Single-shot frequency-resolved optical gating for retrieving the pulse shape of high energy picosecond pulses, *Rev. Sci. Instrum.*, **89**, 103509 (2018).

6. C. McGuffey, M. Dozières, J. Kim, **A. Savin**, J. Park, J. Emig, C. Brabetz, L. Carlson, R. F. Heeter, H. S. McLean, J. Moody, M. B. Schneider, M. S. Wei, F. N. Beg. Soft

X-ray backlighter source driven by a short-pulse laser for pump-probe characterization of warm dense matter, *Rev. Sci. Instrum.*, **89**, 10F122 (2018).

7. L. Ceurvorst, **A. Savin**, N. Ratan, M. F. Kasim, J. Sadler, P. A. Norreys, H. Habara, K. A. Tanaka, S. Zhang, M. S. Wei, S. Ivancic, D. H. Froula, W. Theobald. Channel optimization of high-intensity laser beams in millimeter-scale plasma, *Phys. Rev. E.*, **97**, 043208 (2018).

8. J. D. Sadler, L. O. Silva, R. A. Fonseca, K. Glize, M. F. Kasim, **A. Savin**, R. Aboushelbaya, M. W. Mayr, B. Spiers, R. H. W. Wang, R. Bingham, R. M. G. M. Trines, P. A. Norreys. Advantages to a diverging Raman amplifier, *Communications Physics*, **1**, 19 (2018).

9. **A. F. Savin**, A. J. Ross, M. Serzans, R. M. G. M. Trines, L. Ceurvorst, N. Ratan, B. Spiers, R. Bingham, A. P. L. Robinson, P. A. Norreys. Attosecond-scale absorption at extreme intensities, *Phys. Plasmas*, **24**, 113103 (2017).

10. J. D. Sadler, M. Sliwa, T. Miller, M. F. Kasim, N. Ratan, L. Ceurvorst, **A. Savin**, R. Aboushelbaya, P. A. Norreys, D. Haberberger, A. S. Davies, S. Bucht, D. H. Froula, J. Vieira, R. A. Fonseca, L. O. Silva, R. Bingham, K. Glize, R. M. G. M. Trines. Robustness of raman plasma amplifiers and their potential for attosecond pulse generation, *HEDP*, **23**, 212, (2017).

# List of Figures


1.1 Scanning Electron Miscroscope image of a typical polyHIPE foam. Reprinted with permission from Steckle and Nobile, Fusion Sci. Technol., **43**, 301, (2003). Copyright 2007 American Nuclear Society. . . . 4
1.2 A schematic of the Einstein models of absorption, spontaneous emission, and stimulated emission . . . . . 5
1.3 The history of maximum achievable laser intensity. Reproduced with permission from G. A. Mourou *et al.* 2007 *Plasma Phys. Control. Fusion* **49** B667. Copyright IOP Publishing. All rights reserved . . . . . 7
1.4 A schematic of optical parametric chirped pulse amplification . . . . . 8
1.5 A schematic of the leap-frogging procedure used in particle-in-cell codes 13

2.1 A schematic of Rutherford scattering . . . . . 27
2.2 A pictorial representation of resonance absorption . . . . . 30
2.3 A plot of various electron trajectories associated with vacuum heating 37
2.4 A schematic of High-order Harmonic Generation in gases . . . . . 43
2.5 A schematic of Target Normal Sheath Acceleration . . . . . 47

3.1 Depiction of the three frames of interest when considering Shock Acceleration . . . . . 57
3.2 The surfaces used for integrating the ionic distribution function to find the Sagdeev potential . . . . . 63
3.3 Typical solutions of the distribution function approach for electrostatic shocks propagating through near-critical density plasma . . . . . 67
3.4 A solution to the distribution function model as applied to historical experimental results. . . . . 70
3.5 A plot of the viable parameter space for collisionless shock acceleration. 74
3.6 An extracted section of the parameter space portrayed in Figure 3.5 with areas attainable by various high-power laser systems highlighted. 77

3.7 Schematic of a proposed experiment to measure Collisionless Shock Acceleration using a high-intensity 1 $\mu$m laser system. . . . . 78

4.1 Pictorial representation of the competing effects setting up the potential well that is the centrepoint of Zero Vector Potential absorption . 88
4.2 Schematic indicating the coordinate system used to describe the Zero Vector Potential absorption mechanism . . . . . 90
4.3 Schematic indicating effect of a coordinate transform from the plasma rest frame to the laboratory frame - inducing oscillations beyond the critical density surface . . . . . 92
4.4 Typical initial target profile for 2D OSIRIS simulations investigating the ZVP mechanism . . . . . 100
4.5 Phase space diagram displaying the high-longitudinal-momentum electron peaks characteristic of the ZVP mechanism . . . . . 103
4.6 Momentum-position phase space plots investigating ZVP absorption of an obliquely incident pulse. . . . . 104
4.7 Momentum-position phase space plot investigating the ZVP mechanism under the influence of a circularly polarised laser pulse . . . . . 105
4.8 Intensity spectra of coherent x-rays reflected from a ZVP interaction indicating efficient high harmonic generation . . . . . 106
4.9 Graph of electron energy after absorbing via the ZVP mechanism against plasma electron density. . . . . 107
4.10 Graph of electron energy after absorbing via the ZVP mechanism against laser intensity. . . . . 108
4.11 A plot of ZVP absorption efficiency against laser intensity . . . . . 109
4.12 A plot of ZVP absorption efficiency against the relativistic similarity parameter . . . . . 111
4.13 Target profile for ZVP simulations after the target has begun to be subject to hole boring . . . . . 112
4.14 Plot of the partitioning of energy absorbed via the ZVP mechanism between the plasma electrons and ions . . . . . 113
4.15 Schematic of a proposed experiment to measure the existence of the ZVP mechanism . . . . . 114

5.1 A Feynman diagram of the Breit-Wheeler process. . . . . 124
5.2 A Feynman diagram of the multi-photon Breit-Wheeler process. . . . 125
5.3 Feynman diagrams of the Trident and Bethe-Heitler processes . . . . 126

5.4 Pictorial representation of the QED-modified ZVP mechanism . . . . 128
5.5 Schematic indicating the Gaussian surfaces relevant to the QED-modified ZVP theory. . . . . 130
5.6 Plot of extracted fast electron energy against incident laser $a_0$ for extremely high intensities ($a_0 > 100$). . . . . 136
5.7 Number density of positrons measured in the ZVP EPOCH simulations. 136
5.8 Plot of extracted fast electron energy against incident laser $a_0$ with scaling relations fitted for the QED and non-QED cases. . . . . 137
5.9 Comparison of EPOCH ZVP simulations when the QED Monte Carlo package is and is not artificially suppressed. . . . . 138
5.10 A schematic of the tamped target used in the hydrodynamic HELIOS simulations. . . . . 140
5.11 Plot of the temperature to which a tamped aluminium slab is heated by coherent XUV radiation. . . . . 142
5.12 Schematic of a proposed experiment to measure the existence of the QED modification to the ZVP mechanism, and the heating effect of coherently generated XUV radiation . . . . . 144

# List of Tables

3.1 A comparison of the parameters and results of two experiments: one investigating Radiation Pressure Acceleration, and the other measuring Collisionless Shock Acceleration. . . . . 56
3.2 A set of normalisation factors used to simplify calculations of Collisionless Shock Acceleration . . . . . 61
3.3 Laser Beam Parameters for an experiment investigating Collisionless Shock Acceleration . . . . . 80

4.1 Conversion factors between dimensionless OSIRIS variables and variables with S.I. units . . . . . 102

5.1 Conversion factors between dimensionless OSIRIS variables and variables with S.I. units, as used in EPOCH . . . . . 135

# List of Symbols and Abbreviations

**Vector Notation** Bold script is reserved exclusively for relativistic four-vectors. Classical, three-dimensional vectors are indicated with an arrow over the symbol, e.g. $\vec{A}$. The magnitude of vectors is indicated by moduli symbols, e.g. $|A|$. Tensors are indicated with a double-bar over the symbol.

**Subscripts** Roman subscripts indicate labels: L - laser, p - plasma, e - electron, i - ion. Italic subscripts indicate variables: $t$ - time, $x$, $y$, $z$ - axes. Any variable can, in principle, take any subscript but there are some subscripts reserved for particular cases that are indicated below.

**Tildes:** Tildes are used to indicate that a variable has been normalised into a dimensionless form. The normalisation factor is always given.

$\langle \ldots \rangle$. . . . . Angled brackets indicate that the quantity within the brackets has been time averaged.

$\vec{A}$. . . . . Vector potential of a laser pulse

$A_0$. . . . . Amplitude of said vector potential

$A_{21}$. . . . . Einstein A coefficient

$\mathrm{Ai}(x)$. . . . . First Airy function of $x$

$a$. . . . . Acceleration

$a_0$. . . . . Normalised vector potential

$\vec{B}$. . . . . Magnetic field vector

$B_{21/12}$. . . . . Einstein B coefficient

$b$. . . . . Impact parameter

$C$. . . . . Constant of integration

$\mathcal{C}$. . . . . Heat Capacity

$c$. . . . . Speed of light *in vacuo* $= 3 \times 10^8\,\mathrm{m\,s^{-1}}$

$c_s$. . . . . Speed of sound

$\vec{D}$. . . . . Electric displacement vector

$\vec{E}$. . . . . Electric field vector

$e$. . . . . electronic charge $= 1.6 \times 10^{19}\,\mathrm{C}$

$\vec{F}$. . . . . Force

$\mathcal{F}$. . . . . Fraction (of particles)

$f(\nu)$. . . . . Distribution function of property $\nu$

$f$. . . . . Fraction of incident radiation that is absorbed

$G$. . . . . Arbitrary constant

$\mathcal{G}$. . . . . Arbitrary function

$g$. . . . . Degeneracy of an atomic energy level

$g_{\mu\nu}$. . . . . Minkowski metric

$\vec{H}$. . . . . Magnetic field H-vector

$\mathcal{H}$. . . . . The Hamiltonian of a given system

$\hbar$. . . . . Reduced Planck's constant $= 1.055 \times 10^{-34}\,\mathrm{J\,s}$

$h_{\mathrm{ij}}$. . . . . Heat transfer co-efficient between species i & j

$I$. . . . . Intensity

$\mathcal{I}$. . . . . Integral

$\vec{J}$. . . . . Bulk current density

$\vec{j}$. . . . . Current density associated with a particle

$k$. . . . . Wavevector

$k_{\mathrm{B}}$. . . . . Boltzmann constant $= 1.38 \times 10^{-23}\,\mathrm{J\,K^{-1}}$

$L$. . . . . Typical length scale/size of plasma

$l$. . . . . Distance along axis of propagation

$M$. . . . . Mach number

$M_{\mathrm{ij}}$. . . . . General matrix

$m$. . . . . Mass

$N$. . . . . Population density of an atomic energy level

$N^{*}$. . . . . Population inversion density between a pair of atomic energy levels

$N_{\mathrm{D}}$. . . . . Plasma parameter

$n$. . . . . Number density

$n_{\mathrm{c}}$. . . . . Critical number density

$\mathbf{P}^{\mu}$. . . . . 4-Momentum

$\mathcal{P}$. . . . . Pressure

$\vec{P}$. . . . . Polarisation

$p$. . . . . 3-Momentum

$Q$. . . . . Charge

$q$. . . . . Harmonic order

$R$. . . . . Perpendicular distance from the laser axis of propagation

$\mathcal{R}$. . . . . Radius of curvature of a beam of radiation

$\vec{r}$. . . . . 3-Position vector

$\Delta\vec{r}$. . . . . Small displacement vector

$S$. . . . . Relativistic similarity parameter

$\mathcal{S}$. . . . . Rate (e.g. of reaction, absorption, emission, etc.)

$\hat{s}$. . . . . s-polarisation direction unit vector

$T$. . . . . Temperature. Equivalently, Kinetic Energy

$\mathcal{T}$. . . . . Retarded time

$t$. . . . . Time

$U$. . . . . Energy

$u$. . . . . Velocity of a body prior to interaction

$V$. . . . . Velocity of a frame of reference

$\mathcal{V}$. . . . . Volume

$v$. . . . . Velocity of a body after interaction

$W$. . . . . Work, the time integral of power

$w$. . . . . Radius of a beam of radiation

$w_0$. . . . . Beam waist of a beam of radiation

$Z$. . . . . Ionisation state/Atomic number

$z_\mathrm{R}$. . . . . Rayleigh range

$\alpha$. . . . . Exponential decay factor

$\beta$. . . . . Ratio of velocity to the speed of light, $c$

$\Gamma$. . . . . Adiabatic index

$\gamma$. . . . . Lorentz gamma-factor

$\Delta x$. . . . . Change in $x$

$\delta$. . . . . Skin depth/exponential decay scale-length

$\delta_{ij}$. . . . . Kronecker Delta

$\epsilon$. . . . . Dielectric permittivity

$\epsilon_0$. . . . . Permittivity of free space $= 8.85 \times 10^{-12}\,\mathrm{F\,m^{-1}}$

$\epsilon_{ijk}$. . . . . Levi-Civita symbol

$\varepsilon$. . . . . Ratio of energy to the average energy in a distribution

$\zeta(x)$. . . . . The Riemann-zeta function of $x$

$\eta$. . . . . Index of refraction

$\Theta(x)$. . . . . Heaviside step function of $x$

$\theta$. . . . . Angle of incidence

$\vartheta$. . . . . Temperature normalised to the rest mass energy

$\kappa$. . . . . Thermal Conductivity

$\mathbf{\Lambda}$. . . . . Lorentz Transformation matrix

$\lambda$. . . . . Wavelength

$\lambda_{\mathrm{D}}$. . . . . Debye length

$\lambda_{\mathrm{mfp}}$. . . . . Mean free path length

$\mu$. . . . . Magnetic permeability

$\mu_0$. . . . . Permeability of free space $= 4\pi \times 10^{-7}\,\mathrm{H\,m^{-1}}$

$\nu$. . . . . Damping Frequency

$\nu_{\mathrm{ij}}$. . . . . Collision frequency between species i and species j

$\xi$. . . . . Function solution of the Airy equation as relevant to resonant absorption

$\rho$. . . . . Mass density

$\varrho$. . . . . Radiation density

$\sigma$. . . . . Electrical conductivity

$\varsigma$. . . . . Cross-sectional area

$\tau$. . . . . Pulse duration

$\tau_{\mathrm{p}}$. . . . . Proper time

$\Phi$. . . . . Sagdeev potential

$\phi$. . . . . Spatial electrostatic potential energy

$\varphi$. . . . . Angle of polarisation

$\chi$. . . . . Scattering angle

$\psi$. . . . . Substitution Variable/Gouy phase

$\omega$. . . . . (Angular) frequency

1D. . . . . One-dimension(al)

2D. . . . . Two-dimension(al)

3D. . . . . Three-dimension(al)

BOA. . . . . Breakout Afterburner

CPA. . . . . Chirped Pulse Amplification

CSA. . . . . Collisionless Shock Acceleration

HHG. . . . . High Harmonic Generation

ICF. . . . . Inertial Confinement Fusion

IUPAC. . . . . International Union of Pure and Applied Chemistry

OPCPA. . . . . Optical Parametric Chirped Pulse Amplification

PIC. . . . . Particle-In-Cell

QED. . . . . Quantum Electrodynamic(s)

RPA. . . . . Radiation Pressure Acceleration

TNSA. . . . . Target Normal Sheath Acceleration

XUV. . . . . Extreme Ultraviolet radiation

ZVP. . . . . Zero Vector Potential

# Chapter 1

# Introduction

Since the invention of the laser in 1960 [1], the application of intense, coherent electromagnetic fields has motivated a broad range of research interests ranging from trapped-ion quantum computation [2] to inertial confinement fusion [3–5]. For high-intensity applications of laser systems (here, this is taken to mean systems whose intensities are in excess of $10^{14}\,\mathrm{W\,cm^{-2}}$) such as inertial fusion, the development of chirped pulse amplification [6] opened up the regime of relativistic laser-plasma interactions [7]. It is the future of experiments in this field, in particular, that forms the focus of this thesis.

The structure of this chapter is as follows: first, the basis for interest in the field of laser plasma interactions – with a focus on the processes related to laser-energy absorption – is briefly outlined. This is followed by a summary of the most recent developments in laser-plasma interactions at solid density (commonly referred to as laser-solid interactions), along with the impending commissioning of multi-petawatt laser systems. A concise description of the main simulation methods used in this thesis, namely particle-in-cell and radiative-hydrodynamics simulations is then presented. The chapter is concluded with a statement concerning the author's role in the production of this thesis and an outline of the thesis' structure.

## 1.1 Laser-Plasma Interactions

It is often famously stated that plasma comprises 99% or more of the visible universe [8]. From a purely academic standpoint, therefore, the field of plasma physics is of intrinsic interest to any researcher that wishes to grapple with the scientific questions about the structure and dynamics of the Universe. Unfortunately, technology has not yet advanced to the stage where researchers on Earth are able to conduct experiments remotely at locations such as stellar interiors or deep within the Interstellar Medium. Therefore, it is incumbent on the experimental scientist to create laboratory analogues of these astrophysical phenomena in order to definitively determine their properties [9]. To create a plasma from a material at room temperature requires an enormous amount of energy to be concentrated onto the material so that it can be ionised. There exist a number of methods for creating plasma in the laboratory: radio frequency discharges across two capacitor plates can create low density plasma [10] with temperatures at only a handful of electron-volts - comparable to interstellar clouds [11]. Creating higher energy-density plasma requires more powerful systems: tokamaks [12], Z-pinches [13], and high-power laser systems [14] being three of the most prevalent examples.

The interactions of laser light with plasma is of particular interest to the academic community due to the versatility of high-power laser systems and the wide range of physics that can be investigated in laser-plasma experiments. Understanding laser-plasma interactions is crucial to formulating a description of a wide range of phenomena, ranging from fundamental physical concepts such as parametric instabilities [15] to processes with potentially society-changing impacts such as the realisation of inertial fusion energy [3–5] and the development of compact particle accelerators [16, 17] for medical applications [18, 19]. In the context of both laser-driven particle acceleration, and in Inertial Confinement Fusion (ICF) experiments, the interaction of the laser electromagnetic fields with the plasma gives rise to a number of instabilities [20]

which complicate the analysis of any experimental results. The first step in understanding the seeding and growth of these instabilities is developing a description of how laser energy is transferred from its electromagnetic fields into the plasma, i.e. the processes dictating laser-energy absorption.

The mechanisms of laser-energy absorption and the accompanying laser-driven particle acceleration have been extensively studied and well documented [7, 21] since the invention of the laser [1]. The development of Chirped Pulse Amplification (CPA) [6] opened the field of laser-plasma interactions to a new regime that has been similarly well studied and documented. Experimental data has been published and explained for a large range of laser-plasma experiments from 10 $\mu$m $CO_2$ laser systems accelerating ions in gaseous targets [22, 23] to petawatt-class 1 $\mu$m Nd:glass laser-energy being absorbed in solid-density plasma [24, 25]. With developments in target fabrication being realised to produce high-quality low-density foams and new multi-petawatt class laser systems on the near horizon there is now an opportunity for laser-plasma experiments to both fill in the parameter-space for "mid-density" plasma *and* extend into the next intensity regime, both simultaneously and separately.

## 1.2 Low-Density Solid Laser Targets

Historically, the vast majority of laser-plasma experiments requiring uniform densities have involved firing a laser at either a gas jet launched from a nozzle [22], a solid foil mounted on a post [26], or – in the case of ICF experiments – a spherical fuel pellet [27]. This has restricted laser-plasma experiments with no spatial or temporal density gradients to investigations of plasma with densities on the order of either $\leq 1\,\mathrm{mg\,cm^{-3}}$ (in the case of gaseous targets) or $\geq 1\,\mathrm{g\,cm^{-3}}$ (for solid targets). In recent years, the development of high-quality foam targets [28–31] has opened the experimental parameter space to plasma densities between 1 and $250\,\mathrm{mg\,cm^{-3}}$, effectively closing

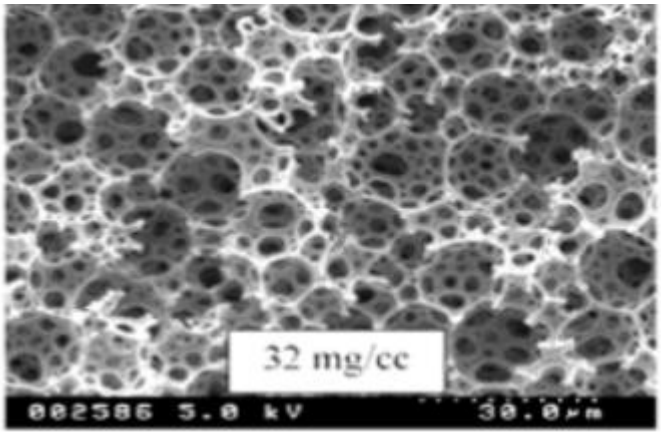



Figure 1.1: Scanning Electron Microscope image of a $32\,\mathrm{mg\,cm^{-3}}$ polyHIPE foam. Reprinted with permission from Steckle and Nobile, Fusion Sci. Technol., **43**, 301, (2003). Copyright 2007 American Nuclear Society. [32]

the gap in explored densities.

"Foams", in this thesis, is used to refer to a porous solid with air bubbles dispersed throughout the material - as is conventional in the field of high-power laser experiments, an example of which, from the work of Steckle Jr. *et al.* [32], can be seen in Figure 1.1. Strictly speaking, the materials referred to within this thesis are generally considered to be macro-porous solids by the International Union of Pure and Applied Chemistry (IUPAC) as they are porous solids with pore sizes greater than 50 nm [33]. One of the most common means of manufacturing these targets is to chemically synthesise the material in a gel[1], and subsequently extract the suspended liquid via freeze-drying [35, 36] or super-critical liquid $CO_2$ extraction [37]. The foams that can be produced via such processes range from inorganic aerogels with high atomic numbers, pore sizes on the order nanometres and an overall density of $1\,\mathrm{mg\,cm^{-3}}$ to acrylate foams (carbon-hydrogen-oxygen molecules - $Z \leq 8$) with pore sizes on the order of microns and densities up to $250\,\mathrm{mg\,cm^{-3}}$ offering high-power laser experiments a diverse range of low-density solids to utilise in investigations of laser-plasma interactions.

[1] A gel is defined by the IUPAC as a network of colloids or polymers that has been expanded by a fluid, i.e. a liquid is dispersed through a network of interconnected molecules in a solid [34].

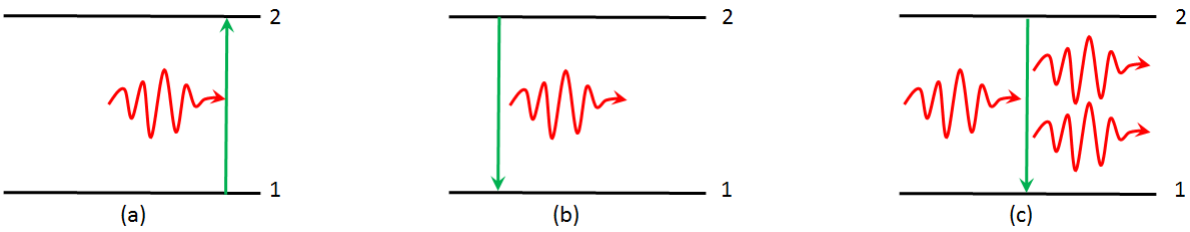



Figure 1.2: A schematic of the three processes involved in atomic energy level transitions in which a photon, or photons (red) of frequency $\omega$ mediate the transition of an electron (green) between two energy levels separated by an energy gap, $U = \hbar\omega$: (a) absorption of a photon, (b) spontaneous emission of a photon, (c) stimulated emission of a second photon.

## 1.3 Multi-Petawatt Laser Systems

Within the context of laser-plasma interactions, the most obvious technological advancements that can be made in the field revolve around increasing laser energies, powers, and intensities. The fundamentals of laser science originate in 1917 with Einstein's description of the three processes governing atomic energy level transitions: absorption, spontaneous emission, and stimulated emission [38]. The rates of these three processes, shown in Figure 1.2, depend on the population densities, $N_i$, the radiation density, $\varrho(\omega)$, and the Einstein A & B coefficients that quantify the atomic processes contributing to the absorption and emission rates. The rate per unit volume of absorption, $\mathcal{S}_\mathrm{a}$, can be expressed as:

$$\mathcal{S}_\mathrm{a} = N_1 B_{12} \varrho(\omega_{21}) \tag{1.1}$$

the rate per unit volume of spontaneous emission, $\mathcal{S}_\mathrm{sp}$, as:

$$\mathcal{S}_\mathrm{sp} = N_2 A_{21} \tag{1.2}$$

and the rate per unit volume of stimulated emission, $\mathcal{S}_{\mathrm{st}}$, as:

$$\mathcal{S}_{\mathrm{st}} = N_2 B_{21} \varrho(\omega_{21}) \tag{1.3}$$

By assuming the energy levels are in thermodynamic equilibrium and that the incident radiation has a Planckian distribution, it is then possible to relate the Einstein A & B coefficients:

$$A_{21} = \frac{\hbar\omega^3}{\pi^2 c^3} B_{21} \tag{1.4}$$

$$g_1 B_{12} = g_2 B_{21} \tag{1.5}$$

where $g_{\mathrm{i}}$ is the degeneracy of the $\mathrm{i}^{\mathrm{th}}$ energy level. These relations are true even when the assumptions of Planckian radiation and thermodynamic equilibrium do not hold as the Einstein coefficients are descriptors of the contribution of atomic processes to the transition rates, not external conditions.

It should be clear from Figure 1.2 and Equations 1.1-1.5 that if the rate of spontaneous emission can be raised above the rate of absorption, it is possible to amplify incident laser light within a so-called gain medium[2]. This has been widely defined as creating a "population inversion" such that $N_2/g_2 > N_1/g_1$. This is typically defined by considering the gain criterion for population inversion density, $N^*$:

$$N^* = N_2 - \frac{g_2}{g_1} N_1 > 0 \tag{1.6}$$

While there are a number of additional criteria for maintaining steady state population inversions [39], the fundamental principle of creating a population inversion is the foundation of laser technology. Increasing the energy, power, and intensity of these pulses is then a matter of building up the population inversion as high as possible before burning it down in as short a time frame as achievable. The first methods

[2]For the purposes of completeness, the reader is reminded here that this is the source of the word "laser": **L**ight **A**mplification by the **S**timulated **E**mission of **R**adiation

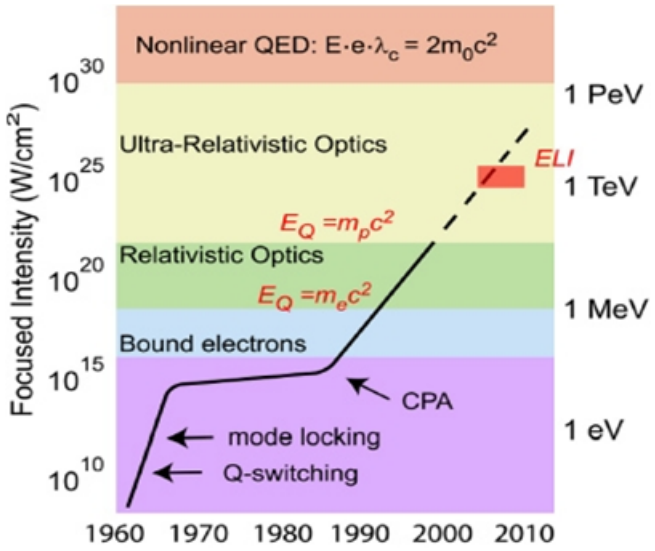



Figure 1.3: The history of maximum achievable laser intensity. Reproduced with permission from G. A. Mourou *et al.* 2007 *Plasma Phys. Control. Fusion* **49** B667. Copyright IOP Publishing. All rights reserved. [40]

for achieving temporary large population inversions, Q-switching and mode-locking, led to laser intensities on the order of $10^{15}\,\mathrm{W\,cm^{-2}}$ by the early 1970s (*cf.* Figure 1.3 [40]). The maximum achievable laser intensity then stagnated until the development of CPA by Strickland and Mourou in 1985 [6]. CPA was a groundbreaking development because it circumnavigated the issue of the time: laser intensities were so high that it was not possible to amplify the pulses any further without breaching the burn thresholds of the gain media of the day. The approach of CPA is to stretch the laser pulse in time (usually using diffraction gratings) before passing the radiation through a gain medium. Due to the extended temporal duration of the pulse, the photon flux is kept below the burn threshold of the gain medium and the laser pulse can be amplified safely. The amplified pulse is then compressed in time (again, usually using a diffraction grating) to increase the power, and thus focused intensity of the laser pulse. CPA rebooted the development of laser technology, and the maximum achievable focused intensity has been increasing at a rate of approximately one order of magnitude each five years ever since.

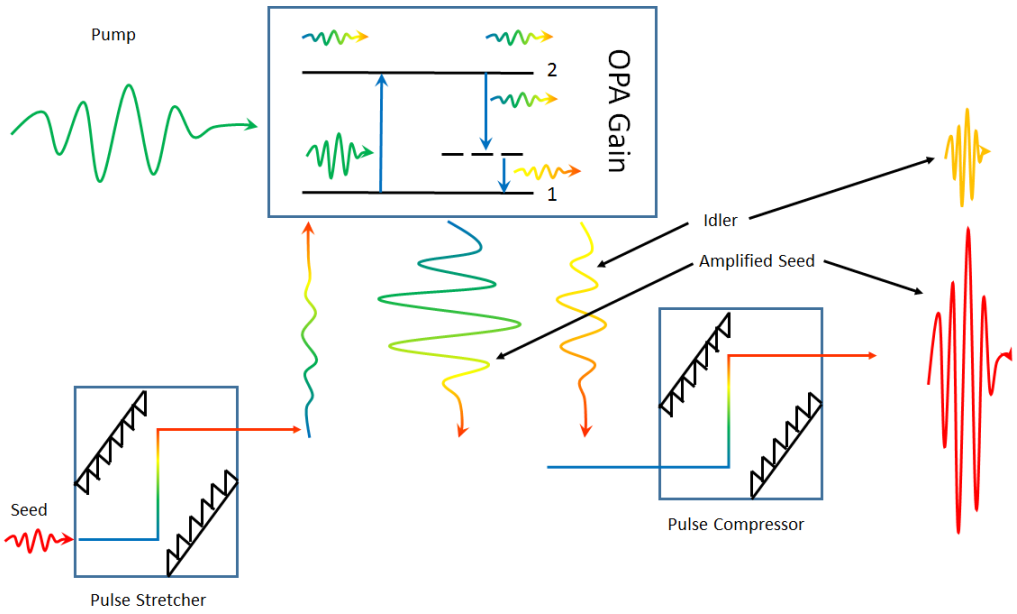



Figure 1.4: A schematic of OPCPA. A seed pulse is stretched to make it a candidate for amplification. The energy of a pump pulse is then transferred to the seed via an intermediate energy level and a newly generated "idler" pulse. The amplified seed and idler are then compressed to yield very high intensity laser pulses.

The next step forward in laser technology - Optical Parametric Chirped Pulse Amplification (OPCPA) - was devised by Dubietis *et al.* [41] and subsequently developed at the Central Laser Facility in the early 2000's [42], and demonstrated on the Vulcan Petawatt facility in 2006 [43]. OPCPA combines the principles of optical parametric amplification with CPA to potentially unlock the multi-petawatt regime for the impending generation of laser facilities, as shown in Figure 1.4. To reach higher intensities with the current standard of optics necessitates compressing the laser pulses to extremely short (on the order of femtosecond) durations, as current optics cannot easily withstand high energy pulses propagating through them. A consequence of this is that large bandwidth pulses are required[3]. Such pulses naturally lend themselves to optical parametric amplification. In the OPCPA scheme, a seed pulse is stretched (identical to the first step of CPA). This stretched seed is then passed through a

[3]The inverse proportionality between bandwidth and pulse duration, $\tau \sim 1/\Delta\omega$, is a direct consequence of the uncertainty principle.

parametric amplification system in the presence of a pump pulse which is absorbed between two levels of the gain medium, the seed stimulates emission to an intermediary level. This intermediary state subsequently decays back to the first level of the gain medium, emitting an "idler" photon in the process to conserve energy and momentum. Both the amplified seed, and the idler pulse are then passed through a compressor, generating very short-duration, high-power laser pulses. OPCPA has been successfully demonstrated on pre-existing laser systems such as Vulcan at the Central Laser Facility in the UK [44] and the ELFIE laser system at Laboratoire pour l'Utilisation des Lasers Intenses in France [45]. It is expected that as facilities with purpose-built OPCPA front ends such as Apollon [46] and ELI [40] come online in the near future, the multi-petawatt regime, and therefore the next intensity regime of laser-plasma interactions, is soon to be reached.

## 1.4 Modelling Laser-Plasma Interactions

Mathematical problems in plasma physics are notoriously difficult, oftentimes impossible, to solve analytically due to the stochastic nature of the motion of the particles in a plasma, which – even as a bulk – is a complex many-bodied system. For this reason, researchers regularly resort to large-scale simulations[4] to numerically solve the governing equations of plasma physics. The results of these simulations are then used to help explain the results of previous experiments; they are also regularly used to justify to funding agencies, or facility access panels that a proposed experiment is likely to be successful. Two of the principal types of code used to model plasma physics, and therefore laser-plasma interactions, are hydrodynamics codes such as the HELIOS code (part of the PRISM suite of software) [47] and the FLASH code developed at the University of Chicago [48], and particle-in-cell (PIC) codes such

[4]These simulations can be truly enormous, running for several days on thousands of computer cores.

as OSIRIS developed at IST Lisbon and UCLA [49] and EPOCH (developed and maintained by the University of Warwick, UK) [50].

### 1.4.1 Hydrodynamics Codes

The principle of all hydrodynamics codes is to neglect the individual particle motion of the constituents of a plasma, and instead consider the collective motion of fluid elements. Conventionally, each species is considered to be a single, distinct fluid and all hydrodynamics codes numerically solve the fluid equations conserving mass, momentum, and energy[5]:

$$\frac{\partial n_\mathrm{j}}{\partial t} + \nabla \cdot (n_\mathrm{j} \vec{u_\mathrm{j}}) = 0 \tag{1.7}$$

$$\rho_\mathrm{j} \left[ \frac{\partial \vec{u_\mathrm{j}}}{\partial t} + (\vec{u_\mathrm{j}} \cdot \nabla)\vec{u_\mathrm{j}} \right] = Q_\mathrm{j} n_\mathrm{j} (\vec{E} + \vec{u_\mathrm{j}} \times \vec{B}) - \nabla \cdot \overline{\overline{\mathcal{P}}}_\mathrm{j} - \rho_\mathrm{j} \sum_k \nu_\mathrm{jk} (\vec{u_\mathrm{j}} - \vec{u_\mathrm{k}}) \tag{1.8}$$

$$\mathcal{C}_\mathrm{V,e} \frac{\partial T_\mathrm{e}}{\partial t} = \kappa_\mathrm{e} \nabla^2 T_\mathrm{e} - \sum_j h_\mathrm{ej} (T_\mathrm{e} - T_\mathrm{j}) - \left( \frac{\partial U_\mathrm{e}}{\partial \mathcal{V}} + \mathcal{P}_\mathrm{e} \right) \frac{\partial \mathcal{V}}{\partial t} + \mathcal{S}_\mathrm{a} - \mathcal{S}_\mathrm{e} + \mathcal{S}_\mathrm{L} \tag{1.9}$$

$$\mathcal{C}_\mathrm{V,j} \frac{\partial T_\mathrm{j}}{\partial t} = \kappa_\mathrm{j} \nabla^2 T_\mathrm{j} - h_\mathrm{ej} (T_\mathrm{j} - T_\mathrm{e}) - \sum_k h_\mathrm{jk} (T_\mathrm{j} - T_\mathrm{k}) - \left( \frac{\partial U_\mathrm{j}}{\partial \mathcal{V}} + \mathcal{P}_\mathrm{j} \right) \frac{\partial \mathcal{V}}{\partial t} \tag{1.10}$$

$$\mathcal{P}_\mathrm{j} = C_\mathrm{j} n_\mathrm{j}^{\mathcal{C}_\mathrm{P,j}/\mathcal{C}_\mathrm{V,j}} \tag{1.11}$$

where $n_\mathrm{j}$ is the number density of species j, $\vec{u}_\mathrm{j}$ its fluid velocity, $\rho_\mathrm{j}$ its mass density, $Q_\mathrm{j}$ its charge, $\mathcal{P}_\mathrm{j}$ its pressure[6], $T_\mathrm{j}$ its temperature, $\mathcal{C}_\mathrm{V,j}$ and $\mathcal{C}_\mathrm{P,j}$ its heat capacities at constant volume and pressure respectively, $\kappa_\mathrm{j}$ its conductivity, $U_\mathrm{j}$ its internal energy, and $C_\mathrm{j}$ is a species-specific constant of integration that fully defines species j's equation of state. $\vec{E}$ and $\vec{B}$ are the electric and magnetic fields in the system, $\nu_\mathrm{jk}$ and $h_\mathrm{jk}$ are

[5]It should be noted here for completeness that all of these equations, with the exception of the equation-of-state are found by taking successive moments of the Boltzmann equation (or Vlasov equation if the system is collisionless) [8].

[6]In Equation 1.8 the pressure term has been included within a pressure-tensor. The off-diagonal terms of this tensor describe the viscosity of the fluid and allow for the effects of shear stresses, amongst other effects, to be considered.

the collision frequency and heat exchange co-efficent between species j and k, $\mathcal{V}$ is the volume of the system, $\mathcal{S}_\mathrm{a}$ and $\mathcal{S}_\mathrm{e}$ are the rates of electron energy absorption and emission, $\mathcal{S}_\mathrm{L}$ is the energy source term for applied external fields such as a laser pulse. Equation 1.7 describes the usual continuity, or conservation of mass, equation; Equation 1.8 is a casting of the Navier-Stokes equation in a form that explicitly includes the effects of electromagnetic fields and collisions; Equations 1.9 and 1.10 describe the energy continuity equations in terms of temperature for the electrons and ions specifically; and Equation 1.11 is the equation of state for species j.

In order to close these equations and make the system solvable, it is common practice - and, in fact, necessary - to input the equations-of-state for all of the species in the plasma into the hydrodynamics code, using published equation-of-state tables such as the SESAME [51] or PROPACEOS [47] databases. There are then two different approaches to numerically solve the fluid equations: the Lagrangian method and the Eulerian. The Eulerian approach to fluid mechanics defines an artificial mesh through which the fluids flow, and measures the fluid's evolution at each point in the mesh over time. In contrast, the Lagrangian framework tracks distinguished fluid parcels and measures the evolution of separate fluid elements as they flow through time and space. Both approaches are used by professional standard codes: the HELIOS code is explicitly Lagrangian, while the FLASH code is Eulerian - albeit with a Lagrangian framework superimposed to allow tracking Lagrangian quantities such as the path of tracer particles [52]. Both approaches require the simulations to be carefully constructed: insufficient spatial or temporal resolution in regions of interest can lead to unphysical results such as artificial heating or the production of fictitious shock waves. Further, while they are useful tools, hydrodynamic codes cannot capture plasma behaviour that is due to the interaction of fields with individual particles, thus prompting the need for other methods of numerically predicting plasma behaviour: one such example is the broad set of particle-in-cell codes.

### 1.4.2 Particle-in-Cell Codes

Particle-in-cell (PIC) codes, as alluded to above, calculate the behaviour of a many-bodied system under the influence of electromagnetic fields. The only equations solved by PIC codes are the Lorentz force law, and Maxwell's equations[7]:

$$m_{\mathrm{j}}\dot{\vec{v}}_{\mathrm{j}} = Q_{\mathrm{j}}(\vec{E} + \vec{v}_{\mathrm{j}} \times \vec{B}) \tag{1.12}$$

$$\nabla \cdot \vec{E} = \frac{1}{\epsilon_0}\sum_{\mathrm{j}} Q_{\mathrm{j}} n_{\mathrm{j}} \tag{1.13}$$

$$\nabla \cdot \vec{B} = 0 \tag{1.14}$$

$$\nabla \times \vec{E} = -\frac{\partial \vec{B}}{\partial t} \tag{1.15}$$

$$\nabla \times \vec{B} = \mu_0 \sum_{\mathrm{j}} Q_{\mathrm{j}} n_{\mathrm{j}} \vec{v}_{\mathrm{j}} + \mu_0 \epsilon_0 \frac{\partial \vec{E}}{\partial t} \tag{1.16}$$

Unfortunately, the number of particles within a typical laser-produced plasma is vastly in excess of $10^{23}$, and solving all five of Equations 1.12-1.16 would be catastrophically expensive and time consuming. Therefore, PIC codes make a number of simplifying assumptions.

Firstly, the simulation space is divided into a series of cells, and each cell is filled with a number of "macro-particles". These macro-particles are initiated with the same charge:mass ratios as the species under investigation but are collated so that several "real" particles are clustered together and represented by a single macro-particle. With the macro-particle density described in both position and velocity space, and the electromagnetic fields initialised it is then possible to numerically solve the system. This can be done via one of two approaches: implicit or explicit [53]. The implicit approach is to update to new values for the electric and magnetic fields before

[7]It is possible, in most PIC codes, to model the effect of collisions by including parameters such as the Coulomb logarithm [8] but this is a second order correction to the workings of PIC codes and so isn't vital to the basic outline presented here.

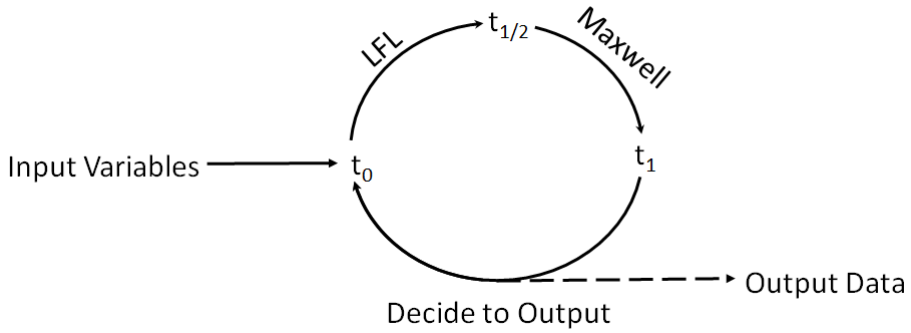



Figure 1.5: Schematic of the leap-frogging procedure used in PIC codes. The Lorentz Force law is used to update the velocities of the particles which are pushed to new positions. Maxwell's equations then use these velocities and positions to re-evaluate the fields at the next half-time step. The cycle repeats with output data produced at the end of each time step for which a request has been made.

calculating the velocity and pushing the particles. In contrast, an explicit solver takes the old, already-stored values for the electric and magnetic fields and uses these to calculate new velocities. The most commonly applied approach in the most widely used PIC codes is the "leapfrog method" depicted in Figure 1.5 which is an explicit solver. In the leapfrog method, time steps are divided into halves with velocities calculated on half-steps and fields and positions on whole steps. If one considers the time step $t$ with a step size of $\Delta t$, the leapfrog method can be written as:

$$\vec{r}_{t+1} = \vec{r}_t + \vec{v}_{t+1/2}\Delta t \tag{1.17}$$

$$\vec{v}_{t+1/2} = \vec{v}_{t-1/2} + \frac{Q}{m}\left(\vec{E}_t + \frac{\vec{v}_{t+1/2} + \vec{v}_{t-1/2}}{2} \times \vec{B}_t\right)\Delta t \tag{1.18}$$

Although Equation 1.18 looks intractable, through matrix algebra it can be solved exactly (see Appendix 1):

$$\vec{v}_{t+1/2} = \frac{1}{1 + (Q\Delta t|B_t|/2m)^2} \times \left\{ \left[1 - \left(\frac{Q\Delta t}{2m}\right)^2\right]\vec{v}_{t-1/2} + \frac{Q\Delta t}{m}(\vec{E}_t + \vec{v}_{t-1/2} \times \vec{B}_t) + \left(\frac{Q\Delta t}{2m}\right)^2 \left[2\left(\vec{v}_{t-1/2} + \frac{Q\Delta t}{2m}\vec{E}_t\right) \cdot \vec{B}_t\right]\vec{B}_t + \frac{1}{2}\left(\frac{Q\Delta t}{m}\right)^2 \vec{E}_t \times \vec{B}_t \right\} \tag{1.19}$$

Thus, provided the temporal resolution (and spatial resolution of the cell grid) is sufficiently high, PIC simulations are able to compute the trajectories of plasma particles and their interactions with incident laser pulses relatively quickly, given the scale of the problem.

In general, the two resolution criteria are expressed as the Courant condition (for time):

$$\Delta t \leq \frac{\Delta x}{c} \tag{1.20}$$

and the Debye condition (for space):

$$\Delta x \ll \lambda_{\mathrm{D}} \tag{1.21}$$

where $\Delta t$ is the time step of the simulation, $\Delta x$ is the simulation's cell size, $c$ is the speed of light in vacuum, and $\lambda_{\mathrm{D}}$ is the Debye length: the length scale over which the collective behaviour of plasma smothers local perturbations[8]. Provided these criteria are met, PIC simulations have the capability (albeit in a potentially costly manner) to simulate and accurately predict a wide range of effects from plasma instabilities such as hosing [54] to laser-driven particle acceleration [23].

## 1.5 Role of the Author & Collaborators

One of the greatest features of scientific research is its collaborative nature, and the research presented in this thesis is no exception. Several individuals and research groups have contributed meaningfully to the work and naming everyone involved would result in an unfortunately long and tedious list for the reader to digest. Therefore, only a small minority of those who made the most significant direct contributions can be named here.

[8]The Debye length, along with other plasma parameters, will be discussed further in Chapter 2.

Firstly, Professor Peter Norreys directed the research and so very little, if any, of the work contained within this thesis can be honestly claimed not to be the result of his insight and input. Other members of the research group, both past and present, have also contributed to the research presented here; specific examples include Dr. Luke Ceurvorst who provided many astute suggestions and improvements to the experiment design that is presented in Chapter 3; Mr. Ben Spiers who has continued much of the work involving said experiment now that its proposal has been accepted for a six-week run on the Vulcan laser at the Central Laser Facility; and Mr. Ramy Aboushelbaya who greatly assisted the author in his understanding of quantum electrodynamics (QED) making the work presented in Chapter 5 possible. The author has also had the great fortune to work with several MPhys students over the course of his DPhil. While attempting (and hopefully succeeding) in providing practical advice and direction to their projects, they have provided invaluable insight into the scientific dilemmas we encountered together.

Outside of the research group in Oxford there have been a number of other individuals who have contributed to the work in this thesis. Dr. Kevin Glize at the Central Laser Facility and Drs. Chris McGuffey, Maylis Dozières, Pierre Forrestier-Colleoni, and Joowhan Kim at the University of San Diego provided an enormous amount of input into developing the author's ability to design high power-laser experiments. Professor Alan Cairns of the University of St. Andrews originally proposed the theoretical model employed in Chapter 3, and stimulating discussions with him provided the direction for the research described therein. To all others who have contributed to the work presented in this thesis, whether through co-authoring papers or five-minute coffee break discussions at conferences, the author can only say thank you and hope that no offence is given by omitting their names here.

Having established the collaborative nature of the work the author has conducted over the course of his DPhil, it is now prudent to attempt to extricate the particu-

lar works that can be attributed to him. Chapters 1 & 2 are almost exclusively the reproduction of historic research, laying the groundwork that motivates and informs the work of the later chapters. In Chapter 3, the extension and application of Cairns' theory [55, 56] to high-power laser experiments for collisionless shock acceleration was the work of the author, as was the design for the proposed (and now accepted) experiment on the Vulcan laser system. The Zero Vector Potential absorption mechanism, originally proposed and described in 1D by Baeva *et al.* [57] is the core of Chapters 4 & 5, significant portions of which have been published by the author [58, 59]. The work extending the mechanism's description beyond one-dimension and theory of how entering the QED regime changes the absorption is the work of the author. The simulation data for the absorption efficiency is from simulations run by the author and informed by the MPhys project of Mr. Thomas Gawne. Similarly, simulation data for the QED-relevant absorption in Chapter 5 is from simulations conducted by the author following the success of Miss Aimee Ross' MPhys project. The hydrodynamics simulations presented at the end of Chapter 5 were the work of the author. The direction of investigation for these simulations was informed by Mr. Thomas Campbell's MPhys project.

## 1.6 Structure of the Thesis

The thesis is structured as follows: Chapter 1 introduces the subject of laser-plasma interactions, and briefly describes some of the recent and impending technological advances that make the content of this thesis relevant to the field of laser-plasma science. The chapter also briefly describes the workings of hydrodynamic and particle-in-cell simulations: two of the most common ways to numerically model laser-plasma interactions. Chapter 1 concludes with a summary of the author's contribution to the research presented in this thesis and an outline of said thesis' structure.

Chapter 2 outlines the theory of laser-plasma interactions, beginning with detailing the most important parameters and properties of both lasers and plasma. It then moves on to outline the most prevalent laser-energy absorption mechanisms understood to date, and some of the methods by which laser systems have been exploited to drive particle acceleration.

Chapter 3 examines the potential progress that could be made in laser-driven particle acceleration. In particular, the high energy density physics community's need for monoenergetic, or quasi-monoenergetic, particle beams is addressed. A simple model, originally proposed by Cairns *et al.* [55,56] is given a more complete exposition than currently exists in the literature and the parameter space for the theory is fully mapped. It is shown that the recent development of low-density solid targets gives a large number of petawatt-class laser systems access to this parameter space, and the potential energies achievable with collisionless shock acceleration using these laser systems is discussed. This chapter concludes with the details of a proposed experiment to measure the quasi-monoenergetic spectrum from collisionless shock acceleration, which is due to be conducted in November 2019.

Chapter 4 moves on to discuss laser-energy absorption beyond the ponderomotive regime: a regime that is predicted to be accessible to impending multi-petawatt laser systems, such as ELI [40] and Apollon [46]. A key focus is put on the "Zero Vector Potential" (ZVP) mechanism originally proposed by Baeva *et al.* [57] and, recently, further developed by Savin *et al.* [58]. Chapter 4 is concluded with unpublished material concerning the efficiencies of the ZVP process and an experiment design that is posited to be suitable for the HERCULES laser facility at the University of Michigan [60].

Chapter 5 extends the ZVP mechanism further, to the limits of the expected capabilities of the next generation of laser systems, and investigates how laser-energy absorption could be expected to change as the laser intensities break into a regime

relevant to quantum electrodynamics processes. A clear and dramatic shift in the power-law scaling of electron energy with laser intensity offers the prospect of a clear experimental signature that investigations into laser-plasma interactions have entered the QED regime (this work has recently been published by Savin *et al.* [59]). The chapter also briefly highlights some of the potential ways in which coherent XUV radiation generated by the fast electrons could be exploited for future investigations. As with previous chapters, Chapter 5 is concluded with a proposed experiment design that may prove suitable for the Extreme Light Infrastructure beamlines system [40] to investigate the applicability of this high-intensity coherent XUV radiation.

Finally, Chapter 6 concludes the thesis and briefly summarises the main results contained therein. It offers some suggestions for the direction that future research into this topic might take as technological capabilities continue to improve.

## 1.7 Summary

In this chapter, the field of laser-plasma interactions was introduced and the future direction of experimental laser-plasma physics was discussed. Particular consideration was given to the development of low-density solid targets made from foams and the impending commissioning of multi-petawatt laser systems. Two of the most prevalent approaches to numerical investigations into laser-plasma interactions - hydrodynamics codes and particle-in-cell codes - were then presented. An explanation of each code type's calculation process and some of the strengths and weaknesses of each approach was given. Finally, the chapter concluded with a discussion of the role of the author in completing the work contained within this thesis, and the structure of said thesis.

# Chapter 2

# Laser Energy Absorption & Laser-Driven Particle Acceleration

At its most fundamental level, laser-plasma interactions can be considered as the various mechanisms by which laser pulses and plasma exchange energy. Broadly speaking, therefore, the most basic of these interactions can be split into laser-energy absorption mechanisms, and laser-driven particle acceleration mechanisms. Each of these mechanisms has its own particular regime of applicability in terms of both the intensity and wavelength of the laser, and the density and ionisation state of the target. To provide as complete and relevant a background to the work presented later in the thesis as is possible, it is important to outline the most prevalent of these mechanisms, and the regimes in which they are applicable. The structure of this chapter, therefore, is as follows: first, various laser-energy absorption mechanisms are described, including a brief exposition for the definition of precisely what constitutes plasma, and concluding with a number of the most prevalent laser-driven ion acceleration schemes[1].

[1]Much of the material covered in this chapter can be found scattered throughout the most important textbooks for postgraduate students studying and researching High Energy Density Physics. They are cited here for the sake of brevity [7, 8, 21, 39]. A small selection of peer-reviewed articles relevant to the specific absorption and acceleration mechanisms are cited in-line in the usual way.

## 2.1 Laser Energy Absorption in Non-Ionised Material

For laser intensities below approximately $10^8\,\mathrm{W\,cm^{-2}}$, the laser energy is insufficient to cause significant ionisation of the target and therefore, most of the laser energy interacts with bound electrons in the target's material. If we consider the case of a general material with electrical conductivity, $\sigma$, dielectric permittivity, $\epsilon$, and magnetic permeability, $\mu$, that is subject to Ohm's law:

$$\vec{J} = \overline{\overline{\sigma}} \cdot \vec{E} \tag{2.1}$$

then Maxwell's equations (Equations 1.13-1.16) - in the case of an electromagnetic wave propagating through the material - can be re-cast as:

$$\nabla \cdot \epsilon\vec{E} = 0 \tag{2.2}$$

$$\nabla \cdot \mu\vec{H} = 0 \tag{2.3}$$

$$\nabla \times \vec{E} = -\mu\frac{\partial\vec{H}}{\partial t} \tag{2.4}$$

$$\nabla \times \vec{H} = \epsilon\frac{\partial\vec{E}}{\partial t} + \overline{\overline{\sigma}} \cdot \vec{E} \tag{2.5}$$

where Equation 2.2 follows from the definition of the electric displacement vector: $\vec{D} = \epsilon\vec{E} \equiv \epsilon_0\vec{E} + \vec{P}$ (where $\vec{P}$ is the polarisation of the material), and $\vec{H} = \vec{B}/\mu$ is the magnetic field H-vector.

By taking the Fourier transform of Equations 2.4 and 2.5, it is possible to obtain a pair of simultaneous equations:

$$\vec{k} \times \vec{E} = -\mu\omega\vec{H} \tag{2.6}$$

$$\vec{k} \times \vec{H} = (\epsilon\omega - i\sigma)\,\vec{E} \tag{2.7}$$

where $\vec{k}$ and $\omega$ are the wavevector and angular frequency respectively of an electromagnetic wave propagating through the material. These equations can be solved to yield a dispersion relation:

$$k^2 = \mu\epsilon\omega^2 - i\mu\sigma\omega \tag{2.8}$$

$$k = \omega\sqrt{\mu\epsilon}\left\{\left[\frac{\sqrt{1+(\sigma/\epsilon\omega)^2}+1}{2}\right]^{1/2} + i\left[\frac{\sqrt{1+(\sigma/\epsilon\omega)^2}-1}{2}\right]^{1/2}\right\} \tag{2.9}$$

The imaginary component of $k$ indicates the absorption of the electromagnetic wave, and assuming that the material is a good conductor (i.e. $\sigma \gg \epsilon\omega$), then the characteristic skin depth, $\delta$, over which the wave's amplitude is attenuated by a factor of $1/e$ is:

$$\delta = [\Im(k)]^{-1} = \sqrt{\frac{2}{\sigma\mu\omega}} \tag{2.10}$$

where $\Im$ indicates taking the imaginary part.

If one takes the conductivity to be that found in the Drude model, $\sigma = n_\mathrm{e}e^2/m_\mathrm{e}\omega$, and uses the definition of electromagnetic wave-speed:

$$\sqrt{\frac{1}{\mu\epsilon}} = \frac{c}{\eta} \tag{2.11}$$

where $\eta$ is the index of refraction of the material and the wave speed is $c/\eta$, then the skin depth can be expressed as:

$$\delta = \sqrt{2}\frac{\omega_\mathrm{p}c}{\eta} \tag{2.12}$$

where $\omega_p^2 = n_\mathrm{e}e^2/m_\mathrm{e}\epsilon$ is the plasma frequency[2].

It can be seen from Equation 2.12, that the attenuation of laser light, even in non-ionised material, depends strongly on the plasma frequency: the natural frequency of

[2]It is noted that it is slightly presumptive to introduce the plasma frequency before defining a plasma, but the nomenclature is so widely used in electromagnetism and condensed matter physics that it would be remiss to not use it here.

electron oscillations in a cold[3] plasma.

## 2.2 Defining a Plasma

Conventionally, three criteria are used to define a plasma:

1. Ionised: a plasma comprises free-moving electrons and ions from which the electrons have been freed.

2. Quasi-neutrality: while there are local variations due to the motion of free charges, over large length scales plasma is a net-neutral composite body.

3. Collective motion: in plasma, long-range electrostatic forces dominate over the collisions that typically dictate the kinetics of gases - this allows the collisionless fluid approximation to be made for plasma and results in plasma dynamics being governed by electromagnetism.

Each of these criteria manifest as a particular property of plasma: the plasma parameter, $N_{\mathrm{D}}$; the Debye length, $\lambda_{\mathrm{D}}$; and the plasma frequency, $\omega_p$.

### 2.2.1 The Plasma Frequency

The collective motion of plasma particles manifests itself as a plasma frequency, briefly alluded to when discussing the absorption of laser energy in non-ionised material. If one considers an ionised system comprising an ion fluid of number density, $n_{\mathrm{i}}$, and charge state, $Z$; and an electron fluid of number density $n_{\mathrm{e}} = Zn_{\mathrm{i}}$; the plasma frequency is determined by displacing the electron fluid by a small distance $\Delta r$. By constructing a Gaussian surface, it can be seen that the electron fluid will be influenced by a restoring electric field, and that the equation of motion for each

[3] "cold", here means that thermal fluctuations have been neglected; no plasma can truly be considered cold in the conventional sense.

electron is:

$$m\frac{\mathrm{d}^2\Delta r}{\mathrm{d}t^2} = -eE = -\frac{n_\mathrm{e}e^2}{m_\mathrm{e}\epsilon_0}\Delta r \tag{2.13}$$

It is clear that Equation 2.13 is the equation of motion for a simple harmonic oscillator with a characteristic frequency given by the plasma frequency:

$$\omega_\mathrm{p}^2 = \frac{n_\mathrm{e}e^2}{m_\mathrm{e}\epsilon_0} \tag{2.14}$$

Thus the mathematical expression for criterion 3 of the plasma criteria is that:

$$\omega_\mathrm{p} \gg 2\pi\nu_\mathrm{en} \tag{2.15}$$

(where $\nu_\mathrm{en}$ is the electron-neutrals collision frequency) as this expresses that electrostatic forces dominate over the kinetic effects that are typical of gases.

### 2.2.2 The Debye Length

The extent to which a plasma is quasi-neutral is quantified by the Debye length, $\lambda_\mathrm{D}$. If one considers a test charge embedded within a plasma then its electrostatic potential, $\phi$, can be expressed in Poisson's equation as:

$$\epsilon_0\nabla^2\phi = -e(Zn_\mathrm{i} - n_\mathrm{e}) \tag{2.16}$$

Assuming that the ionic and electronic number densities can be described by a Boltzmann distribution ($n_\mathrm{j} = n_\mathrm{j}^0 \exp\left(-Q_j\phi/k_\mathrm{B}T_\mathrm{j}\right)$), and that the plasma is weakly coupled (i.e. $e\phi \ll k_\mathrm{B}T_\mathrm{j}$ where $T_\mathrm{j}$ is the temperature of species, j), then the number density of electrons and ions can be described as:

$$n_e(\vec{r}) = n_e^0\left(1 + \frac{e\phi(\vec{r})}{k_\mathrm{B}T_\mathrm{e}}\right) \tag{2.17}$$

$$n_i(\vec{r}) = \frac{n_e^0}{Z}\left(1 - \frac{Ze\phi(\vec{r})}{k_{\mathrm{B}}T_{\mathrm{i}}}\right) \tag{2.18}$$

By substituting Equations 2.17 and 2.18 into Equation 2.16, an expression for the Debye length can be deduced:

$$\nabla^2\phi = \frac{\phi}{\lambda_{\mathrm{D}}^2} \tag{2.19}$$

where the Debye length is given by:

$$\frac{1}{\lambda_{\mathrm{D}}^2} = \frac{1}{\epsilon_0}\left[\frac{n_{\mathrm{e}}e^2}{k_{\mathrm{B}}T_{\mathrm{e}}} + \frac{Zn_{\mathrm{i}}e^2}{k_{\mathrm{B}}T_{\mathrm{i}}}\right] \tag{2.20}$$

which, in the limit of the electrons being much more energetic than the ions[4] can be simplified to:

$$\lambda_{\mathrm{D}} = \sqrt{\frac{\epsilon_0 k_{\mathrm{B}}T_{\mathrm{e}}}{n_{\mathrm{e}}e^2}} \tag{2.21}$$

To satisfy the second of the plasma criteria, it is simply required that the Debye length is much shorter than the size of the bulk plasma so that quasineutrality can hold over the course of several Debye lengths.

### 2.2.3 The Plasma Parameter

The plasma parameter, $N_{\mathrm{D}}$, is by far the simplest of the properties that can be attributed to a plasma: it is simply the number of free charged particles contained within a sphere whose radius is equal to the Debye length:

$$N_{\mathrm{D}} = \frac{4}{3}\pi n_{\mathrm{e}}\lambda_{\mathrm{D}}^3 = \frac{4}{3}\pi\left(\frac{\epsilon_0 k_{\mathrm{B}}T_{\mathrm{e}}}{e^2}\right)^{3/2} n_{\mathrm{e}}^{-1/2} \tag{2.22}$$

Provided the plasma parameter is much larger than one, then the first plasma criterion is satisfied.

[4]This approximation holds in most laser-plasma interactions as the electrons are heated directly by the laser and the electron-ion collision frequency is typically much lower than the electron plasma frequency.

Thus the three plasma criteria can be expressed mathematically as:

1. $N_{\mathrm{D}} \gg 1$

2. $\lambda_{\mathrm{D}} \ll L$

3. $\omega_{\mathrm{p}} \gg \nu_{\mathrm{en}}$

Provided these three criteria are satisfied, one can be confident that a system's dynamics are in the plasma regime, and can therefore consider the processes by which plasma absorbs laser energy.

## 2.3 Inverse Bremsstrahlung

In a collisionless plasma, and for laser intensities in excess of $10^{13}\,\mathrm{W\,cm^{-2}}$, with wavelengths sufficiently long that the photon energies are much less than the ionisation potentials of the plasma, the dominant absorption process is inverse bremsstrahlung [61,62]. In this process, photons accelerate electrons in the vicinity of ions - the exact opposite of bremsstrahlung radiation where electrons radiate photons due to being decelerated by the electric field of nearby ions. The rate of energy absorption through inverse bremsstrahlung, $\mathcal{S}_{\mathrm{IB}}$ can be expressed as:

$$\mathcal{S}_{\mathrm{IB}} = U_{\mathrm{P}} \nu_{ei} \tag{2.23}$$

where $U_{\mathrm{p}}$ is the energy imparted to an electron by a laser[5] and $\nu_{\mathrm{ei}}$ is the electron-ion collision frequency. To proceed further with an understanding of inverse bremsstrahlung requires a functional form for both $U_{\mathrm{p}}$ and $\nu_{\mathrm{ei}}$.

[5]This energy has presumptively been given the index "P" in anticipation of the derivation of the ponderomotive energy.

### 2.3.1 The Ponderomotive Energy

If one considers initialising an electron at rest at time $t = 0$ in a background oscillating electric field of frequency $\omega_{\mathrm{L}}$ oriented in the $\hat{x}$-direction, described by $\vec{E} = E_0\hat{x}\cos\omega_{\mathrm{L}}t$ then its equation of motion is given by:

$$\frac{\mathrm{d}\vec{v}}{\mathrm{d}t} = \frac{-e}{m_{\mathrm{e}}}E_0\hat{x}\cos\omega_{\mathrm{L}}t \tag{2.24}$$

which can be integrated to give the electron's velocity vector:

$$\vec{v} = \frac{-eE_0}{m_{\mathrm{e}}\omega_{\mathrm{L}}}\hat{x}\sin\omega_{\mathrm{L}}t \tag{2.25}$$

The so-called ponderomotive energy is then the energy attributed to the root-mean-square average of this velocity:

$$U_{\mathrm{P}} = \frac{1}{2}m_{\mathrm{e}}\langle v^2\rangle = \frac{1}{4}a_0^2 m_{\mathrm{e}}c^2 \tag{2.26}$$

where $a_0$ is the normalised vector potential:

$$a_0 = \frac{eE_0}{me\omega_{\mathrm{L}}c} \equiv \sqrt{\frac{I_{\mathrm{W\,cm^{-2}}}\lambda^2_{\mu\mathrm{m}}}{1.37\times10^{18}}} \tag{2.27}$$

### 2.3.2 Electron-Ion Collision Frequency

To evaluate the electron-ion collision frequency, it is normal to consider the Rutherford model of scattering as depicted in Figure 2.1. If an electron approaches an ion in charge state $Z$, then it will be subject to the Coulomb force. To first order, the main contribution to the Coulomb force will be as the electron is deflected around the ion, at a constant distance roughly equal to the impact parameter, $b$. Under these

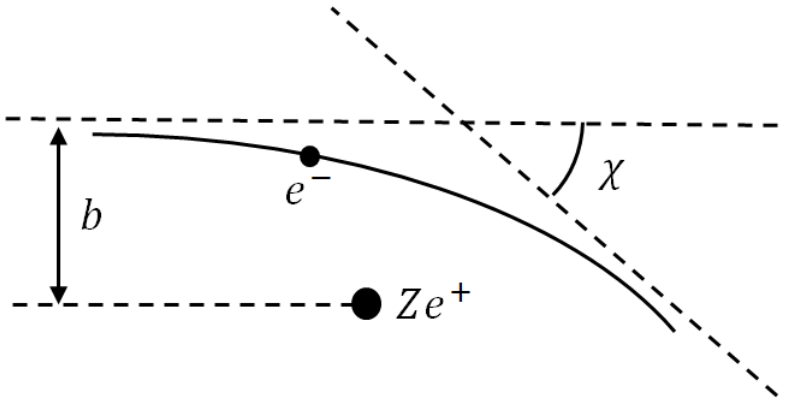



Figure 2.1: A schematic of Rutherford scattering of an electron with an impact parameter, $b$, relative to a stationary ion through a scattering angle, $\chi$.

conditions the equation of motion is given by:

$$\frac{\Delta p}{\Delta t} = \frac{-Ze^2}{4\pi\epsilon_0 b^2} \tag{2.28}$$

Given that the interaction between the ion and the electron will last for a time $\Delta t \approx b/v$, it is possible to write the change in velocity due to Rutherford scattering as:

$$|\Delta v| = \frac{Ze^2}{4\pi\epsilon_0 m_e v b} \tag{2.29}$$

The collision time can be considered as the average time it takes for a typical electron within the plasma to be deflected through a scattering angle of $\chi = 90°$. More formally, one can view this as the time it takes for the root-mean-square of $\Delta v$ to vary from 0 to $v$[6]. This requires integrating across all possible cross section elements, $\pi b^2 \to 2\pi b\,\mathrm{d}b$, such that:

$$\nu_{\mathrm{ei}} v^2 = \frac{\mathrm{d}\langle \Delta v^2 \rangle}{\mathrm{d}t} = \int_{b_{\min}}^{b_{\max}} n_{\mathrm{i}} v (\Delta v)^2 2\pi b\,\mathrm{d}b \tag{2.30}$$

[6]One can assume that after being scattered the final speed is approximately $v$ as the ion is so massive relative to the electron that it remains stationary throughout the interaction.

By considering that the maximum viable impact parameter is the Debye length, $\lambda_D$, on account of the shielding effect of plasma quasi-neutrality, and that the minimum plausible impact parameter will be one for which the magnitude of the velocity change, $\Delta v$, is approximately equal to the original speed, $v$, such that:

$$b_{\min} = \frac{Ze^2}{4\pi\epsilon_0 m_e v^2} \tag{2.31}$$

then by inputting these integral limits and substituting Equation 2.29 into the integrand of Equation 2.30, then the electron-ion collision frequency can be easily retrieved:

$$\nu_{\mathrm{ei}} = \frac{Z^2 n_i e^4}{8\pi\epsilon_0^3 v^3 m_{\mathrm{e}}^2} \ln\left(\frac{\lambda_D}{b_{\min}}\right) \tag{2.32}$$

which can be simplified greatly by using Equations 2.14, 2.21, and 2.22, and by taking $v$ to be the thermal velocity of the plasma, $v = \sqrt{k_{\mathrm{B}} T_{\mathrm{e}}/m_{\mathrm{e}}}$:

$$\nu_{\mathrm{ei}} = \frac{1}{6}\frac{\omega_{\mathrm{p}}}{N_{\mathrm{D}}} \ln\left(\frac{\lambda_{\mathrm{D}}}{b_{\min}}\right) \tag{2.33}$$

When Equation (2.32) is combined with Equation (2.26), Equation 2.23 becomes:

$$\mathcal{S}_{\mathrm{IB}} = \frac{1}{24}\frac{a_0^2 m_{\mathrm{e}} c^2 \omega_{\mathrm{p}}}{N_{\mathrm{D}}} \ln\left(\frac{\lambda_{\mathrm{D}}}{b_{\min}}\right) = \frac{I_{\mathrm{W\,cm^{-2}}} \lambda_{\mu\mathrm{m}}^2 n_{\mathrm{cm^{-3}}} T_{\mathrm{eV}}^{-3/2}}{7.85 \times 10^{20}} \ln\left(\frac{\lambda_{\mathrm{D}}}{b_{\min}}\right) \tag{2.34}$$

It can be seen from Equation 2.34, that inverse bremsstrahlung is strongest in high intensity, low-frequency laser interactions with cold, dense plasma. Typically inverse bremsstrahlung is a dominant absorption process for laser intensities in the range $10^{-3} < a_0 < 0.3$, although it can play an important role in absorption processes in higher intensity laser-plasma interactions; particularly in the lower-density ablation front of a laser-produced plasma, provided that the mean free path of the electrons, $\lambda_{\mathrm{mfp}} = v\nu_{\mathrm{ei}}$, is significantly shorter than the skin depth of the ablating plasma [25].

## 2.4 Resonance Absorption

Another absorption mechanism that is dominant in the intensity range $10^{-3} < a_0 < 0.3$ is resonant absorption [63]. In this process, an obliquely incident p-polarised laser pulse propagates through a plasma to the critical density surface[7] and drives a plasma wave, thus transferring energy from the laser into the plasma. There are two key effects to model when considering resonance absorption: the movement of the reflection surface away from the critical density surface when using an obliquely incident pulse, and the transfer of energy from the electromagnetic wave into the plasma wave.

### 2.4.1 The Critical Density Surface

It is well known that the greater the density of a medium, the higher frequency the radiation must possess in order to be able to transmit through the medium[8]. Thus, it is to be expected that for a given frequency of wave, there is a "critical density" beyond which materials are opaque to that particular frequency. If one considers the dispersion relation given in Equation 2.8, and again takes the conductivity to be that found in the Drude model, then it can be seen that:

$$c^2k^2 = \omega^2\left(1 - \frac{n_\mathrm{e}e^2}{m_\mathrm{e}\epsilon_0}\frac{1}{\omega^2}\right) \tag{2.35}$$

At this stage, it is common to identify the plasma frequency and state that electromagnetic waves cannot propagate unless their frequency exceeds the plasma frequency. It is also possible, however, to frame this more explicitly in terms of the density by

[7]The critical density surface will be described shortly.

[8]Indeed, the use of medical X-ray scans is dependent upon this.

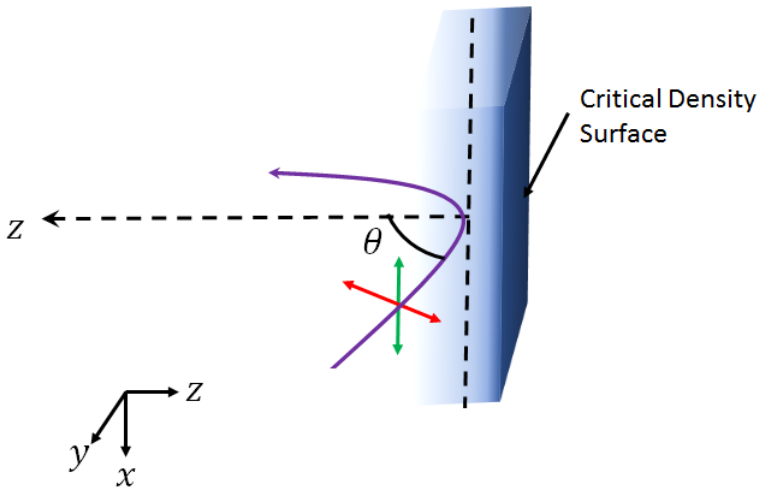



Figure 2.2: Reflection of an obliquely incident pulse (purple), with angle of incidence $\theta$ from a plasma (fading blue). The critical density surface is the rightmost surface of the plasma, the red arrow indicates the direction of p-polarisation in the $\hat{y}-\hat{z}$ plane, and the green arrow indicates s-polarisation in the direction of the $\hat{x}-$axis.

defining a frequency's critical density, $n_{\mathrm{c}}$ as:

$$n_{\mathrm{c}}(\omega) = \frac{\omega^2 m_{\mathrm{e}} \epsilon_0}{e^2} = \frac{1.11 \times 10^{21}}{\lambda_{\mu\mathrm{m}}^2} \, [\mathrm{cm}^{-3}] \tag{2.36}$$

Thus, the index of refraction, $\eta$, of a plasma can be expressed as:

$$\eta^2(\vec{r}, t) = \left(1 - \frac{n_{\mathrm{e}}(\vec{r}, t)}{n_{\mathrm{c}}}\right) \tag{2.37}$$

For a normally incident laser pulse, the critical density surface is the surface from which the pulse reflects when propagating through plasma with a density gradient. The reflection surface for an obliquely incident pulse, however, is not positioned at the same point in the plasma.

### 2.4.2 Reflection of an Obliquely Incident Pulse

As alluded to above, the first effect to consider when modelling resonant absorption is the displacement of the reflection surface from the critical density surface, as seen

in Figure 2.2[9]. If one considers first the reflection of an s-polarised[10] laser pulse from a plasma with a density gradient then it is necessary to consider the wave equation for an oscillating electric field:

$$\nabla^2 \vec{E} - \frac{\eta^2}{c^2} \frac{\partial^2 \vec{E}}{\partial t^2} = 0 \tag{2.38}$$

For s-polarisation, only the $\hat{x}-$component of the electric field is of interest and by taking the temporal Fourier transform of Equation 2.38, a separable partial differential equation is recovered[11]:

$$-\frac{\partial^2 E_x}{\partial y^2} = \frac{\partial^2 E_x}{\partial z^2} + \frac{\omega^2}{c^2}\eta^2(z)E_x = k_y^2 E_x \tag{2.39}$$

where the separation constant has been preemptively identified as the $\hat{y}$-component of the wavevector, $k_y$.

In order to conserve momentum, $k_y$ must be constant, and it is a trivial solution that far from the critical density surface of the plasma:

$$k_y = \frac{\omega}{c} \sin\theta \tag{2.40}$$

where $\theta$ is the angle of incidence of the laser, as defined in Figure 2.2. The electric field can now be expressed as:

$$E_x = E(z) \exp\left[-i\omega(t - \frac{y}{c}\sin\theta)\right] \tag{2.41}$$

[9]The axis directions specified in Figure 2.2 are the same as will be used throughout the rest of this section.

[10]s-polarisation is polarisation in the direction perpendicular to the plane of propagation, originating from the German word for "perpendicular": *senkrecht*. The German word for "parallel" is *parallel*, and so p-polarisation indicates polarisation in the plane of propagation but still perpendicular to the axis of propagation.

[11]The full derivation of resonant absorption can be found in Appendix A.

which subsequently yields the dispersion relation:

$$c^2 k_z^2(z) = \omega^2(\eta^2(z) - \sin^2\theta) \tag{2.42}$$

and so, the reflection surface is at the position where $\eta^2(z) = \sin^2\theta$ or at the reflection density surface, with density $n_{\text{refl}}$:

$$n_{\text{refl}} = n_{\text{c}} \cos^2\theta \tag{2.43}$$

### 2.4.3 Transferring Energy from Laser to Plasma

It should be clear from Figure 2.2 that s-polarised light cannot be resonantly absorbed by a plasma, as the s-polarisation unit vector, $\hat{s}$, is orthogonal to the wavevector of any induced longitudinal plasma waves. In contrast, p-polarised light will have some component of its electric field in the same direction as the plasma wavevector, and so resonance absorption is possible for this polarisation. For the purposes of this discussion, we will assume that there is a linear density ramp with a characteristic skin depth, $\delta$:

$$n_{\text{e}}(z) = \frac{z}{\delta} n_{\text{c}} \tag{2.44}$$

which is a generally valid approximation provided $z \ll \delta$.

Consideration of Equation 2.2, under the assumption that the plasma is unmagnetised (i.e. $\mu = \mu_0$, $\epsilon/\epsilon_0 = 1 - n_{\text{e}}(z)/n_{\text{c}}$) yields:

$$\nabla \cdot \vec{E} = -\frac{1}{\epsilon}\frac{\partial \epsilon}{\partial z} E_z \tag{2.45}$$

which clearly has a resonance for $\epsilon = 0$: at the critical density surface. In order for there to be electromagnetic fields that can be resonantly absorbed, it is necessary that while the laser pulse is reflected at the reflection surface given in Equation 2.43,

some portion of the fields must penetrate to the critical density surface. The easiest method to proceed is to consider the s-polarised $\vec{B}-$field which will have the form given in Equation 2.41. By considering Equations 2.1, 2.5, and 2.44, a functional form for the $\hat{z}-$component of the electric field can be deduced:

$$E_z = \frac{cB(z)\sin\theta}{1 - z/\delta} \tag{2.46}$$

It then becomes a matter of solving for $B(\delta)$, which is assumed to be an exponentially decayed form of the B-field at the reflection surface:

$$B(\delta) = B(\delta\cos^2\theta)e^{-\alpha} \tag{2.47}$$

where $\alpha$ is the exponential decay factor that is yet to be calculated. If Equations 2.40, 2.41, and 2.44 are substituted into Equation 2.38, this results in:

$$\frac{\mathrm{d}^2B}{\mathrm{d}z^2} - \left(\frac{z - \delta\cos^2\theta}{\delta}\right)\frac{\omega^2}{c^2}B = 0 \tag{2.48}$$

which is a form of the Airy equation, and thus has known solutions:

$$B(z) = G \times \mathrm{Ai}\left[(z - \delta\cos^2\theta)\left(\frac{\omega^2}{\delta c^2}\right)^{1/3}\right] \tag{2.49}$$

where $\mathrm{Ai}(x)$ is the first Airy function [64] and $G$ is a constant of integration. By assuming that the magnetic field has sinusoidal solutions in the region $z < 0$, it is possible to evaluate $G$ and subsequently determine that the magnetic field at the reflection surface is given by:

$$B(\delta\cos^2\theta) \approx 0.9\frac{E_0}{c}\left(\frac{c}{\omega\delta}\right)^{1/6} \tag{2.50}$$

where $E_0$ is the amplitude of the electric field of the laser as it propagates through

free space.

It now remains to calculate the exponential decay factor, $\alpha$:

$$\alpha = \int_{\delta\cos^2\theta}^{\delta} \frac{\mathrm{d}z}{c}\sqrt{\omega_\mathrm{p}^2(z) - \omega^2\cos^2\theta} = \frac{2}{3}\frac{\omega\delta}{c}\sin^3\theta \tag{2.51}$$

Therefore, by combining Equations 2.46, 2.47, 2.50, and 2.51, it is possible to determine the electric field at the critical density surface:

$$E_z = \frac{E_0}{1 - z/\delta}\sqrt{\frac{c}{2\pi\omega\delta}} \times \xi\left[\left(\frac{\omega\delta}{c}\right)^{1/3}\sin\theta\right] \tag{2.52}$$

where $\xi(x) = 2.3x \times \exp(\frac{2}{3}x^3)$.

From this stage, it is possible to calculate the fraction, $f_\mathrm{res}$, of incident radiation that is absorbed. In order to do this, a damping frequency term, $\nu$, is introduced to account for any interactions (such as collisions) that introduce heating. To accomplish this the index of refraction must be modified:

$$\eta^2(z) = 1 - \frac{\omega_\mathrm{p}^2(z)}{\omega^2} \longrightarrow 1 - \frac{\omega_\mathrm{p}^2(z)}{\omega(\omega + i\nu)} \tag{2.53}$$

This modifies the expression for the electric field in Equation 2.52 and so the fraction of absorbed radiation can be written as:

$$f_\mathrm{res} = \frac{1}{E_0^2}\int_0^\infty \frac{\nu E_z^2}{c}\mathrm{d}z = \frac{\nu\xi^2}{2\pi\omega\delta}\int_0^\infty \frac{\mathrm{d}z}{(1 - z/\delta)^2 + (\nu/\omega)^2} \tag{2.54}$$

It transpires that not only can the integral in Equation 2.54 be solved, the solution is fully independent of $\nu$, meaning that the precise nature of the collisions or other damping effects are not critical to any consideration of resonant absorption:

$$f_\mathrm{res} = \frac{1}{2}\xi^2\left[\left(\frac{\omega\delta}{c}\right)^{1/3}\sin\theta\right] \tag{2.55}$$

Analysis of the resonant absorption problem has yielded the result that for p-polarised light at an oblique incidence, the absorption is most efficient when the incident laser pulse is able to drive resonance in the plasma wave most successfully. This occurs at the maximum of the function $\xi$ and has been found to be at the angle [7, 25]:

$$\theta \approx \arcsin\left[0.8\left(\frac{c}{\omega\delta}\right)^{1/3}\right] \tag{2.56}$$

### 2.4.4 Anharmonic Resonant Absorption of Femtosecond-Class Pulses

While the model for resonant absorption described above is perfectly adequate for the interaction of picosecond and nanosecond-class lasers with plasma, it does not describe the resonant absorption of femtosecond-class pulses - primarily because there is not enough time to set up a smooth density ramp. It was this problem that prompted the study of anharmonic resonance [65]. Mulser *et al.* identified that a number of criteria needed to be satisfied in order to explain the results of simulations and experiments investigating the absorption of femtosecond-class pulses [24, 66–68]. They identified that as fast electrons are generated within just a few laser cycles, resonance with the plasma frequency (Equation 2.14) must be the physical mechanism driving absorption; but, given that the absorption is observed in simulation to occur before any density modulation takes place, the resonance must be anharmonic - with any anharmonicity arising from the difference between the laser frequency, $\omega$, and the plasma frequency, $\omega_{\mathrm{p}}$.

Although the governing equations, in particular the Hamiltonian, for anharmonic resonance is somewhat different to the "standard" case described above, many of the qualitative results are retained: no heating is observed for circularly polarised light at normal incidence, absorption is strongest for p-polarised light incident at an oblique angle and absorption efficiencies are typically on the order of tens of

percent. As such the details of the governing mathematics are not provided here, but the existence of anhamornic resonance absorption is noted as it is a prevalent and important absorption mechanism for obliquely incident p-polarised femtosecond pulses incident on overcritical plasma.

## 2.5 Brunel Heating (a.k.a. Vacuum Heating)

In the derivation given above for resonant absorption, a gentle density gradient from the critical density surface to vacuum was assumed. In general, for the interaction of short-pulse lasers with intensities exceeding $10^{15}\,\mathrm{W\,cm^{-2}}$ with solid targets, such an assumption is invalid. Instead, Brunel suggested that if the scale length of the density gradient is less than $a_0\lambda/2\pi$ then a different process ought to dominate the absorption of the laser energy [69]. This "Brunel heating", or vacuum heating as it is often known, has been further explored since Brunel's original proposition [66, 70, 71] and is recognised as one of the dominant absorption mechanisms in high-power laser-plasma experiments [25].

Brunel heating can be considered by simply considering the motion of an electron under the influence of the electric fields arising from the laser field and from the displacement of the electron fluid from its ion background[12]. If one considers the situation of a semi-infinite plasma, with plasma of electron number density $n_\mathrm{e}$ for $x > 0$, and vacuum for $x < 0$, then an electron that starts initially at rest at a position $x_0 > 0$ will be subject to the electric fields of both the laser, $E_\mathrm{L}\sin\omega t$, and that arising from the displacement of electrons from the ion background[13]:

$$E_\mathrm{p} = \frac{n_e e}{\epsilon_0}[x\Theta(x) - x_0] \tag{2.57}$$

[12]For all of the following, the ion background is assumed to be static. Given the orders of magnitude difference between the electronic and ionic acoustic speeds, this assumption holds over the time frames considered here.

[13]A more complete derivation of Brunel Heating can be found in Appendix A

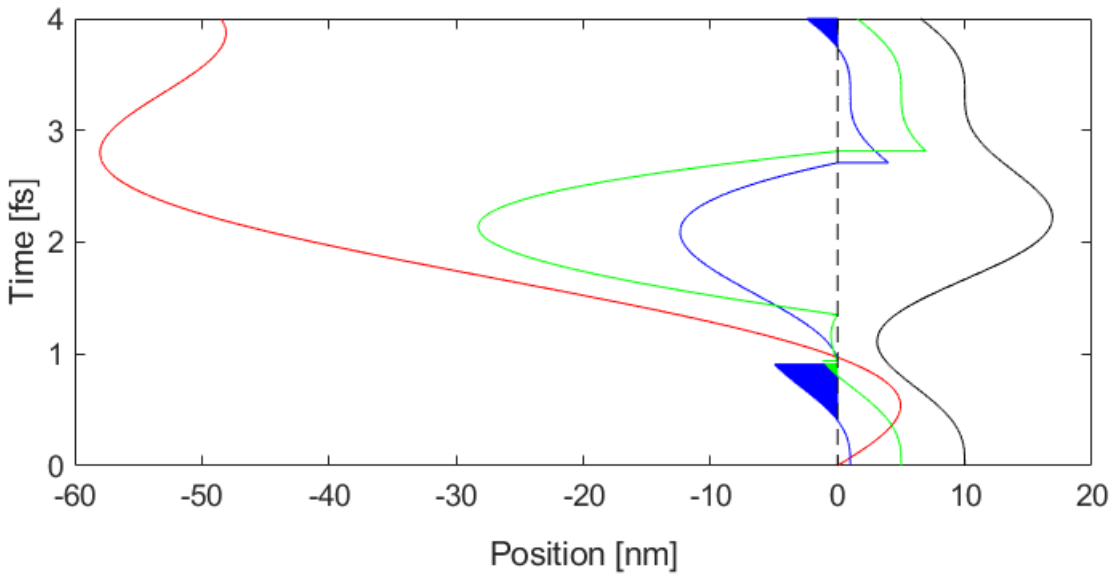



Figure 2.3: Plot of the trajectories for electrons in the 1D vacuum heating model for starting positions of 0 nm (red), 1 nm (blue), 5 nm (green), and 10 nm (black) from the critical density surface. The critical density surface is indicated by the vertical dashed black line. The laser is modelled as a 1 $\mu$m-wavelength pulse with an intensity of $1.37 \times 10^{16}\,\mathrm{W\,cm^{-2}}$ incident on a plasma with an electron density $4.5 \times 10^{21}\,\mathrm{cm^{-3}}$.

where $\Theta(x)$ is the Heaviside step function. It follows that the equation of motion of an electron is then:

$$\ddot{x} = -\omega_\mathrm{p}^2[x\Theta(x) - x] - a_0\omega c \sin\omega t \tag{2.58}$$

Under the initial conditions of $x(0) = x_0$, $\dot{x}(0) = 0$, Equation 2.58 yields the solution (example trajectories of which are plotted in Figure 2.3):

$$x = \begin{cases} \dfrac{\lambda a_0}{2\pi}\left[(\sin\omega t - \sin\omega t_\mathrm{c} + \dfrac{\omega(t_\mathrm{c}-t)}{1-(\omega_\mathrm{p}/\omega)^2}\left(\cos\omega_\mathrm{p}t_\mathrm{c} - \dfrac{\omega_\mathrm{p}^2}{\omega^2}\cos\omega t_\mathrm{c}\right)\right] + \\ \qquad\qquad \dfrac{\omega_\mathrm{p}^2(t-t_\mathrm{c})^2}{2}x_0, & x < 0 \\ x_0 + \dfrac{\lambda a_0}{2\pi}\dfrac{(\omega/\omega_\mathrm{p})\sin\omega_\mathrm{p}t - \sin\omega t}{(\omega_\mathrm{p}/\omega)^2 - 1}, & x > 0 \end{cases} \tag{2.59}$$

where $t_\mathrm{c}$ is a "crossing time" when the electron crosses the plasma-vacuum interface

at $x = 0$ and is given by the equation:

$$\frac{\omega}{\omega_{\mathrm{p}}} \sin \omega_{\mathrm{p}} t_{\mathrm{c}} - \sin \omega t_{\mathrm{c}} = -\frac{2\pi x_0}{a_0 \lambda} \left( \frac{\omega_{\mathrm{p}}^2}{\omega^2} - 1 \right) \tag{2.60}$$

The physical picture of vacuum heating is that in lieu of being able to drive a resonant absorption process, the laser field pulls electrons from close to the surface of the plasma out into the vacuum. These electrons are then launched back into the plasma where they deposit their energy. It can be determined that Equation 2.60 only has solutions of $t_c$ if $x_0 < \delta$, where $\delta$ is the skin depth of the plasma, meaning that beyond the skin depth, no electrons can be pulled into the vacuum:

$$\delta = \frac{\lambda a_0}{2\pi} \frac{\omega/\omega_{\mathrm{p}}}{(\omega_{\mathrm{p}}/\omega) - 1} \tag{2.61}$$

The absorption efficiency of this process can be calculated by considering the kinetic energy flux of the electrons involved in vacuum heating during one laser cycle and equating this to some fraction, $f_{\mathrm{vh}}$ of the incident intensity:

$$\frac{1}{2} m_{\mathrm{e}} v_{\mathrm{osc}}^2 \times n_{\mathrm{e}} \delta \times \frac{\omega}{2\pi} = f_{\mathrm{vh}} \times \frac{1}{2} \epsilon_0 c E_L^2 \cos\theta \tag{2.62}$$

where $m_{\mathrm{e}} v_{\mathrm{osc}}^2/2$ is the kinetic energy associated with the oscillations out of the plasma, into the vacuum, and back again; $n_{\mathrm{e}} \delta \omega / 2\pi$ is the particle flux; and the $\cos\theta$ term accounts for the mitigation of the intensity due to an oblique incidence angle.

It is possible, from here, to show that the absorption efficiency is given by:

$$f_{\mathrm{vh}} = \frac{1}{1 - (\omega/\omega_{\mathrm{p}})^2} \frac{1}{2\pi} \frac{v_{\mathrm{osc}}^3}{v_{\mathrm{L}}^2 c \cos\theta} \tag{2.63}$$

where $v_{\mathrm{L}} = eE_{\mathrm{L}}/m_{\mathrm{e}}\omega$ is the quiver velocity associated with a response to the laser's electric field. It is more interesting, and illustrative, to express the absorption effi-

ciency explicitly as:

$$f_{\mathrm{vh}} = \left[\frac{2}{\pi}\frac{1}{(\omega_{\mathrm{p}}^2/\omega^2 - 1)^2(1 - \omega/\omega_{\mathrm{p}})}\frac{1}{\cos\theta}\right] a_0 \tag{2.64}$$

Here, it is clear that the absorption efficiency of vacuum heating scales linearly with $a_0$. It is less obvious, but also demonstrated from Equation 2.64 that the absorption efficiency is inversely proportional to the electron number density of the plasma. These scaling relations are common to the predominant absorption mechanisms within the ponderomotive regime[14].

## 2.6 Relativistic $\vec{j} \times \vec{B}$ Heating

The final laser-energy absorption mechanism to be considered in this chapter is the $\vec{j} \times \vec{B}$ heating mechanism proposed by Kruer and Estabrook in 1985 [72]. This absorption mechanism arises from the $\vec{j} \times \vec{B}$ term in the Lorentz force law, when considering non-linear, or ponderomotive, effects.

### 2.6.1 Classical Ponderomotive Force

Suppose there is an electromagnetic field with some slowly varying spatial dependence incident on a plasma:

$$\vec{E} = E_{\mathrm{S}}(x)\sin\omega t\ \hat{y} \tag{2.65}$$

[14]The ponderomotive regime here, and throughout this thesis, means the laser and plasma conditions for which absorption is dominated by resonant absorption, vacuum heating, and the soon to be presented $\vec{j} \times \vec{B}$ absorption process.

It is possible to determine the effect of this variation by splitting the Lorentz force law for an electron into equilibrium, linear, and non-linear parts:

$$\begin{cases} \dot{\vec{v}}_{\mathrm{eq}} = 0 \\ \dot{\vec{v}}_{\mathrm{l}} = -\dfrac{e\vec{E}_{\mathrm{eq}}}{m_{\mathrm{e}}} \\ \dot{\vec{v}}_{\mathrm{nl}} = -\dfrac{e}{m_{\mathrm{e}}}\left[\vec{E}_{\mathrm{l}} + \vec{v}_{\mathrm{l}} \times \vec{B}_{\mathrm{l}}\right] \end{cases} \tag{2.66}$$

Given the form of the electric field in Equation 2.65, it is relatively simple to extract the linear perturbation to the velocity and position of an electron:

$$\vec{v}_{\mathrm{l}} = \frac{eE_{\mathrm{S}}(x)}{m_{\mathrm{e}}} \cos\omega t \; \hat{y} \tag{2.67}$$

$$\vec{r}_{\mathrm{l}} = \frac{eE_{\mathrm{S}}(x)}{m_{\mathrm{e}}\omega^2} \sin\omega t \; \hat{y} \tag{2.68}$$

It is then feasible to deduce the linear perturbations on the electric and magnetic fields (finding the latter by using Equation 1.15):

$$E_{\mathrm{l}} = (\vec{r}_{\mathrm{l}} \cdot \nabla)(E_{\mathrm{S}}\hat{y})|_{\vec{r}=\vec{r}_{\mathrm{eq}}} \sin\omega t \tag{2.69}$$

$$\vec{B}_{\mathrm{l}} = \frac{1}{\omega}\nabla \times (E_{\mathrm{S}}\hat{y})|_{\vec{r}=\vec{r}_{\mathrm{eq}}} \cos\omega t \tag{2.70}$$

By substituting Equations 2.67, 2.69, and 2.70, into the non-linear part of Equation 2.66, the classical equation for the ponderomotive force can be found:

$$\vec{F}_{\mathrm{P}} = -\frac{e^2}{m_{\mathrm{e}}\omega^2}\left[(\vec{E}_{\mathrm{S}} \cdot \nabla)\vec{E}_{\mathrm{S}} \sin^2\omega t + \vec{E}_{\mathrm{S}} \times (\nabla \times \vec{E}_{\mathrm{S}}) \cos^2\omega t\right] \tag{2.71}$$

Using the vector identity $\vec{A} \times (\nabla \times \vec{A}) = (\nabla \cdot \vec{A})\vec{A} - (\vec{A} \cdot \nabla)\vec{A}$, recognising that the $(\vec{E}_{\mathrm{S}} \cdot \nabla)\vec{E}_{\mathrm{S}} = 0$, and that $(\nabla \cdot \vec{E}_{\mathrm{S}})\vec{E}_{\mathrm{S}} = \nabla \cdot \vec{E}_{\mathrm{S}}^2/2$ gives the final result:

$$\vec{F}_{\mathrm{P}} = -\frac{e^2}{m_{\mathrm{e}}\omega^2}(1 + \cos 2\omega t)\nabla E_{\mathrm{S}}^2(x) \tag{2.72}$$

### 2.6.2 Relativistic Ponderomotive Force

To properly consider what happens during a relativistic $\vec{j} \times \vec{B}$ heating process, consider the fluid form of the Lorentz force law:

$$\frac{\partial \vec{p}}{\partial t} + (\vec{v} \cdot \nabla)\vec{p} = -e(\vec{E} + \vec{v} \times \vec{B}) = e\nabla\phi + e\frac{\partial A}{\partial t} - e\vec{v} \times \nabla \times \vec{A} \tag{2.73}$$

where $\phi$ and $\vec{A}$ are the scalar and vector electromagnetic potentials respectively.

By again separating the momentum into slowly varying, $p_0 = \gamma m_{\mathrm{e}} v$, and quickly varying, $p_{\mathrm{f}} = eA$, and using the same vector identity for the triple vector product as above a simplified form can be deduced:

$$\frac{\partial \vec{p}_0}{\partial t} + (\vec{v} \cdot \nabla)\vec{p}_0 = \frac{d\vec{p}_0}{dt} = e\nabla\phi - \frac{1}{2m_{\mathrm{e}}\gamma}\nabla|p_{\mathrm{f}}|^2 \tag{2.74}$$

where the first term on the right-hand side is an electrostatic force and the second term is the ponderomotive force, which - by considering $\gamma = \sqrt{1 + \langle p \rangle^2/m_e^2 c^2}$ - can be expressed as:

$$\vec{F}_{\mathrm{P}} = -m_{\mathrm{e}}c^2\nabla(\gamma - 1) \tag{2.75}$$

From Equation 2.75, it is easy to extract the so-called ponderomotive energy [24]:

$$U_{\mathrm{P}} = (\gamma - 1)m_{\mathrm{e}}c^2 \tag{2.76}$$

By considering that $\gamma^2 = 1 + (\langle p \rangle/m_e c)^2$, and that the time-averaged value of the

momentum will depend on the polarisation and amplitude of the incident laser pulse, it is then possible to retrieve Wilks' ponderomotive scaling relation for the "hot electron temperature" [25]:

$$T_{\mathrm{h}} = \begin{cases} (\sqrt{1+a_0^2}-1)m_e c^2, & \text{Circular Polarisation} \\ (\sqrt{1+a_0^2/2}-1)m_e c^2, & \text{Linear Polarisation} \end{cases} \tag{2.77}$$

Again, as for vacuum heating, the energy of the electrons that absorb via this mechanism scales approximately linearly with $a_0$, this has been verified both in simulations [24] and experiment [73], and the electron energy has been seen there to scale inversely with electron density.

It is worth noting, in the concluding part of this section, that it is the angle of incidence that is the most crucial factor in determining whether it is vacuum heating or $\vec{j}\times\vec{B}$ heating that dominates. If $\sin\theta > a_0\omega/\omega_{\mathrm{p}}$ then vacuum heating is expected to dominate while if the converse is true then $\vec{j}\times\vec{B}$ heating is the prevalent effect [25].

## 2.7 High Harmonic Generation

It is well known that accelerating charged particles radiate with the power, $\mathrm{d}W/\mathrm{d}t$, of the emitted radiation proportional to the square of the particle's acceleration, explicitly written as Larmor's formula [74]:

$$\frac{\mathrm{d}W}{\mathrm{d}t} = \frac{Q^2 \dot{v}^2}{6\pi\epsilon_0 c^3} \tag{2.78}$$

Thus it should be no surprise that for the electrons that absorb energy from a high-power, short-pulse laser, a significant fraction of the absorbed energy is re-emitted. One process by which this occurs is High Harmonic Generation (HHG), which has been studied extensively: in theory, simulation, and experiment [75–82].

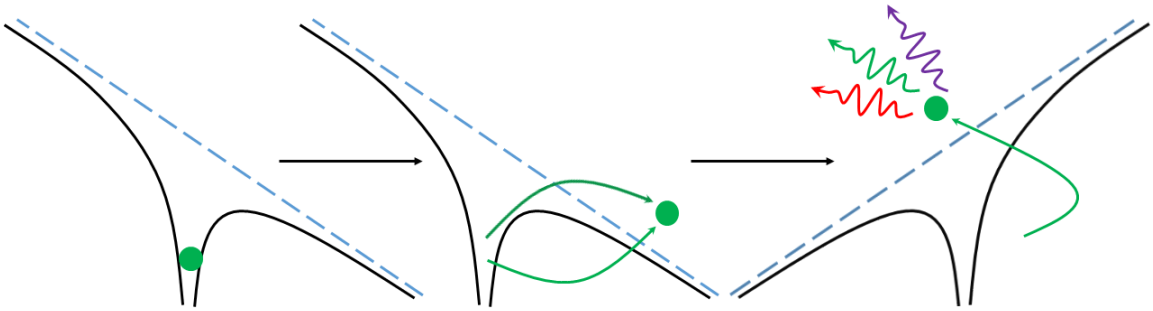


Figure 2.4: A schematic of high-order harmonic generation depicting the three-step process of potential superposition, electron escape, and recombination. This leads to the emission of coherent x-ray radiation.

The generation of high-order harmonics was first observed in laser-interactions with gases in the late 1980s [83, 84] and a model for such generation shortly followed [85, 86]. This model, as portrayed in Figure 2.4, describes a three step process. In the first step, the electric field of a linearly polarised incident laser superposes with the atomic potential binding a valence electron to its atom. This acts to suppress one side of the ionisation potential while augmenting the other. In the next step, depending on how suppressed the ionisation potential is by the laser field, the electron either tunnels through the potential barrier, or simply escapes over the top of the barrier to become a free particle. The final step concerns the interaction of the now free electron with the linearly polarised laser field: first the electron is accelerated away from the atom, before being returned to the atomic core, albeit at higher energy. When the re-captured electron interacts with its parent ion, a number of processes can occur (e.g. emission of a second valence electron or the excitation of a bound electron),- one of which is the emission of a high-order harmonic photon.

The process in a plasma, however, is somewhat different. It is also, notably, very easy to distinguish between harmonic generation from gases and from plasma. Due to the inversion symmetry of noble gas atoms[15], even-order harmonic generation is suppressed and so only odd-order harmonics can be observed; this is not the case for

[15]Most HHG experiments in gases have been conducted using noble gases [75].

HHG in plasma where all orders can be generated up to a certain cut-off frequency [75]. The generation of high-order harmonics from the interaction of high-energy nanosecond laser pulses with plasma has been studied via non-linear electromagnetic fluid dynamics [75]. However, when considering higher intensities - such as those seen in femtosecond and picosecond class laser systems - the nature of the plasma is radically different. Over such a short timescale, the plasma is not able to set up a smooth-gradient ablation front, and the plasma can be modelled with a Heaviside function (as in Equation 2.58). Unfortunately, due to the sharp density gradient, the waves described in the standard fluid approach are vulnerable to breaking and the model fails [70, 87, 88]. A new model - the oscillating mirror model - was proposed and developed to circumvent this issue [80,89–91]. In this model, the electron density $n_{\mathrm{e}}$, is assumed to have both a spatial and temporal dependence:

$$n_{\mathrm{e}}(x,t) = Zn_{\mathrm{i}}\Theta\left[x - x_{\mathrm{m}}(t)\right] \tag{2.79}$$

were $x_m(t)$ is the position of the mirror surface at a time, $t$. Given that the incident laser light will now be reflecting from a moving surface, it is necessary to introduce the retarded time, $\mathcal{T}$:

$$\mathcal{T} = t - \frac{x_{\mathrm{m}}(t)}{c} \tag{2.80}$$

The field reflected from the surface will be sinusoidal and of the form $E = E_0 \sin\omega\mathcal{T}$, and so if the mirror surface is oscillating sinusoidally (e.g. $x_{\mathrm{m}} = x_0 \sin\omega_{\mathrm{m}}t$), then the reflected electric field will have an explicitly anharmonic spectrum:

$$E = E_0 \sin\left[\omega\left(t - \frac{x_0}{c}\sin\omega_{\mathrm{m}}t\right)\right] \tag{2.81}$$

This model was later modified to a "spiky" mirror model [80] which predicted a

characteristic spectrum for radiation originating from HHG:

$$I_q = I_1 q^{-8/3} \tag{2.82}$$

Where $q$ is the harmonic order, and $I_q$ is the intensity of the $q^{\text{th}}$ harmonic. This spectrum was subsequently experimentally validated [78, 79].

Recent years have seen a number of theoretical and experimental results that optimise HHG ranging from measurements of extremely high-orders ($q \geq 3000$) [79], to optimisation of the ablation front scale-length ($\delta_{\text{opt}} \approx 0.2\lambda$, where $\lambda$ is the wavelength of the incident laser) [82]. Further, while early milestone experiments investigating HHG found the emission to be isotropic [77], the development of plasma mirrors as high-intensity optics has made it possible to focus HHG radiation into areas smaller than the original focal spot size of the incident laser [92, 93].

## 2.8 Laser-Driven Ion Acceleration

The discussion to this point has almost exclusively concerned how laser-plasma interactions mediate the exchange of energy between a laser field and the electrons. Indeed, even the case of High Harmonic Generation is simply a consequence of an incident laser field's interactions with electrons. The reason that this can be done is that the ions typically respond on the order of two-thousand times slower to the effects of a laser field than the electrons[16]. Therefore, assuming that the ion fluid is a static background is often valid for the case of femtosecond-class lasers interacting with plasma. However, in the high-energy pico- and nano-second regime of laser-plasma interactions, there is sufficient time for the ions to absorb a significant fraction of the incident laser energy, albeit often through the electrons as a mediator.

[16]This should not be surprising given that even a single proton is 1836 times more massive and therefore 1836 times more inertial than an electron.

These high energy ions can be exploited for a variety of purposes, they can be a source of isochoric heating in warm dense matter experiments [94], a diagnostic in the form of proton radiography [95], and have been posited as a plausible candidate for proton- or ion-based fast ignition in ICF experiments [96, 97] and in hadron therapy [18, 19]. In this section, a very brief description of some prevalent ion acceleration mechanisms will be presented: Target Normal Sheath Acceleration, Radiation Pressure Acceleration, and Breakout Afterburner. The case of Collisionless Shock Acceleration (CSA) will be discussed separately in the next chapter as CSA is the main topic of Chapter 3.

### 2.8.1 Target Normal Sheath Acceleration

Possibly the most prevalent, and widely studied, ion acceleration scheme is Target Normal Sheath Acceleration (TNSA) [26, 98, 99]. In this mechanism, an intense laser pulse interacts with a solid target with a preformed ablating plasma on the front surface. The laser pulse accelerates electrons in the preformed plasma to high energy and launches these electrons into the bulk target, as shown in Figure 2.5. These hot electrons propagate through the bulk of the target, with the divergence of the electron beam increasing due to collisions with ions in the target (*cf.* Section 2.3.2). The hot electrons eventually breakout and form a dense negatively charged sheath on the rear side of the target. This sheath field ionises atoms close to the rear edge of the target and pulls them out into vacuum, accelerating them to form a high energy divergent broadband ion beam.

The maximum energy achievable through TNSA is known to be [100]:

$$U_{\max} = 2k_{\mathrm{B}}T_{\mathrm{h}}\left[\ln\left(\tilde{t} + \sqrt{\tilde{t}^2+1}\right)\right]^2 \tag{2.83}$$

where $\tilde{t} = t_{\mathrm{acc}} \times Z(m_{\mathrm{e}}/m_{\mathrm{i}})\omega_{\mathrm{p}}/\sqrt{2\exp(1)}$ is a normalised expression for the length of

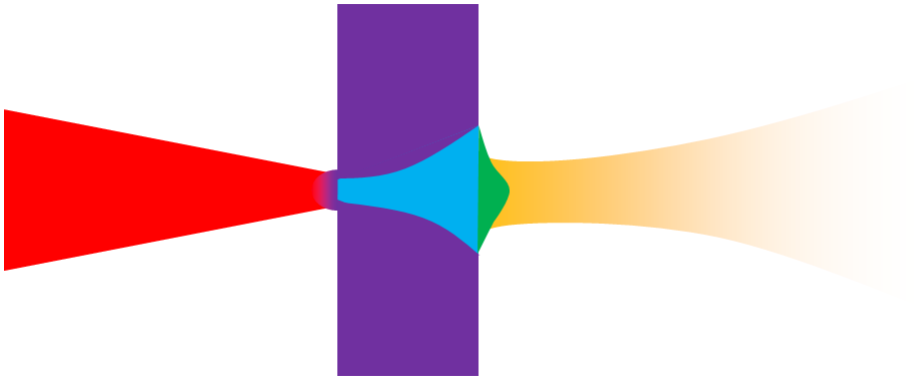


Figure 2.5: A schematic of Target Normal Sheath Acceleration. A high intensity laser pulse (red) incident on a solid target (purple): the laser's pre-pulse creates an ablation front of pre-plasma. The main part of the laser pulse accelerates the electrons in the pre-plasma launching them into the main target. These hot electrons (blue) diverge in the target and emerge on the rear side of the target creating a dense, hot sheath (green). The electric field of this sheath ionises atoms on the rear surface of the target and accelerates them, normal to the surface of the target creating a high energy expanding ion beam (yellow).

time over which the ions are accelerated, and $T_{\mathrm{h}}$ is the hot electron temperature. For sub-picosecond lasers, $T_{\mathrm{h}}$ is modelled well by Equation 2.77. However, recent results have indicated that TNSA can be augmented by using multi-picosecond pulses to generate the hot electrons; the hot electron temperature in this case can exceed the ponderomotive scaling by 30% or more and yield significantly more energetic cut-offs in the ion energy spectrum [101]. TNSA is now used regularly to provide high-energy protons with spectral cut-offs on the order of tens of MeV with $>10^{13}$ protons possessing energies above 4 MeV. The one notable limit to TNSA is that the ion spectrum is very broad[17], making it very difficult to extract meaningful quantitative information from diagnostics such as proton radiography [102].

[17]This is, in part, due to the fact that TNSA is dependent on electron temperature which is an intrinsically statistical quantity. More critically, however, is the fact that ions closer to the rear surface of the target shield ions deeper in the bulk from the sheath field and so the accelerating electric field that the ion feels is strongly dependent on its initial position.

### 2.8.2 Radiation Pressure Acceleration

An alternative approach to producing ion beams, and one that produces very narrow-band ion spectra, is Radiation Pressure Acceleration (RPA) [103]. In this scheme, the radiation pressure of an intense laser pulse incident on a critically over-dense plasma ($n_e > n_c$) forces electrons into the target via the $\vec{j} \times \vec{B}$ force. The sudden introduction of electrons in the bulk of the target sets up an electrostatic shock which propagates through the target at a speed equal to the hole boring velocity, $v_{hb}$. Given that the radiation pressure of a laser pulse reflected from a target can be expressed as: $\mathcal{P} = 2I/c$, it is a simple matter of equating the radiation pressure to a momentum flux - $n_e v_{hb} \times m_e v_{hb}$ - to obtain a form for the hole boring velocity:

$$v_{hb} = \sqrt{\frac{2I}{n_e m_e c}} \tag{2.84}$$

The electrostatic field of the shock pulls along ions downstream of the shock at the hole boring velocity, while those ions that are upstream of the shock are specularly reflected from the shock front, acquiring a speed of twice the hole boring velocity and attaining energies of:

$$U = \frac{1}{2} m_i (2v_{hb})^2 = \frac{m_i}{m_e} \frac{4I}{n_e c} \tag{2.85}$$

If the target is so thin that all of the electrons can be ejected from the rear edge of the target (i.e. the target thickness is less than $c/\omega_p$), then all of the ions will be downstream of the "shock" and will be dragged in unison by the electrons. This is known as the "light-sail" regime of RPA, and has been theorised to be applicable not just to ion acceleration but also to interstellar travel [104][18]. The nature of reflection of ions from a well-defined shock front leads one to predict that ions accelerated via RPA will be mono-energetic. Unfortunately, it has been established that

[18]The author admits that this is possibly the most bizarre and fanciful reference in the thesis, but must also admit that the prospect of citing this particular paper was an opportunity that was simply too good to pass up.

in order for RPA to dominate over TNSA on a linearly-polarised laser system with wavelengths of approximately 1 $\mu$m, it is necessary for the intensities to be on the order of $10^{22}\,\mathrm{W\,cm^{-2}}$ or greater [103]. It has been theorised that circularly polarising the laser light will allow RPA to dominate at lower intensities [105]; principally this is due to the fact that the laser pulse's instantaneous amplitude never passes through zero, and so the electrons are continuously expelled through the target. This prevents a sheath field from forming, and thus inhibits TNSA. This prediction was validated experimentally [106], but the high intensities required to achieve RPA in solid-density targets led to a relatively broadband spectrum.

A pioneering experiment conducted by Palmer *et al.* circumvented this issue by firing a 10 $\mu$m $CO_2$ laser at a gas target [22]. Not only did this reduce the intensity required to enter the RPA regime, but the use of hydrogen gas also meant that the produced proton beam was notably free from impurities. The measured proton beams were notable for their high-brightness (exceeding $10^{12}\,\mathrm{MeV^{-1}\,sr^{-1}}$), with peak energies on the order of 1 MeV with just a 4% energy spread, and a signal-to-noise ratio over 100. However, while these results are promising, a significant contributor to the result is the use of a 10 $\mu$m laser and a gas target. Most notably, when trying to scale this to higher intensity 1 $\mu$m systems with thin foils, the use of high-Z elements has been seen to introduce a large number of impurities into the proton beam [107]. It should be noted that it is possible to accelerate heavier ions, such as $C^{5+}$ [108], but the spectrum here is still impure in the sense that while one component may be quasi-monoenergetic, other species are also present with significantly broader spectra.

Nonetheless, the monoenergeticity of ions accelerated via reflection from a shock front has prompted research into the possibility of using collisionless electrostatic shocks to achieve what it appears RPA cannot: an impurity-free, quasi-monoenergetic, high peak-energy proton beam on current high-intensity, high-energy 1 $\mu$m laser systems [23, 55, 56, 109, 110]. CSA is an active field of research, the discussion of which

will be intertwined with the results presented in Chapter 3.

### 2.8.3 Breakout Afterburner

As mentioned above, RPA has been successfully seen when using circularly polarised light. When using linearly polarised light in the same regime, a different phenomenon - laser breakout afterburner (BOA) - is seen [111–113]. The process for BOA is broken into stages: firstly direct TNSA occurs in a thin foil[19]. However, because the foil is thin, a large fraction of the initially cold electrons are expelled into the sheath. This lowers the plasma frequency of the foil and moves the reflection surface of the laser pulse deeper into the target. A consequence of the propagation of the reflection surface is that the laser pulse is able to directly heat a larger number of electrons, eventually heating all of the electrons within the foil and creating a very large sheath field. In this sense, the second stage of BOA is very similar to RPA, in that the ions are being accelerated by a large longitudinal electric field set up by the forward-propagation of hot electrons. The third, and final stage, of BOA occurs when the entire plasma is transparent to the laser due to sufficient heating of the electrons. The laser fully penetrates the plasma through to the rear surface, thus heating the sheath electrons to form a relativistically high-temperature electron beam. The large difference between the electron beam and ion beam velocities seeds an instability somewhat similar to the Farley-Buneman instability[20] [114, 115] which acts to accelerate and heat the ions while simultaneously decelerating the hot electrons. However, the energy of the laser (which is co-propagating with the fast electron beam) is absorbed by the electrons, thus maintaining their high energy and forcing the accelerating longitudinal electric fields set up by the Farley-Buneman-like instability to persist. This results in very high-energies for heavy ion spectra.

[19] Thin, here, means that the thickness of the target is on the order of the laser wavelength

[20] The Farley-Buneman instability is a form of two-stream instability which acts to reduce the difference in the drift velocities of electrons and ions in a plasma.

In general, it is expected that hybrid mechanisms, such as BOA, which combine facets of TNSA and RPA will yield the highest energy protons, indeed such a hybrid mechanism is believed to have resulted in proton energies of almost 100 MeV [116]. Nonetheless, the measured spectra are still broad and so despite the impressiveness of the energy cut-offs in the spectra obtained to date, the goal of a narrowband high-energy proton beam from interactions of a 1 $\mu$m laser with a plasma is yet to be achieved.

## 2.9 Summary

In this chapter, the background physical theory underpinning and motivating the work presented in the rest of this thesis was presented. The chapter began with a brief description of the process by which laser light can be absorbed in dielectric non-ionised materials. It was noted that as laser intensities extend beyond $10^{13}\,\mathrm{W\,cm^{-2}}$, there is sufficient energy associated with the electric field to ionise the atoms and cause the target material to transition from the solid or gaseous phase into plasma. The three parameters most commonly used to define and characterise a plasma (plasma frequency, Debye length, and plasma parameter) were defined, as was the plasma state itself. This was followed by a description of the most common and dominant absorption mechanisms in both the classical regime ($10^{13}\,\mathrm{W\,cm^{-2}} < I < 10^{15}\,\mathrm{W\,cm^{-2}}$) and the ponderomotive regime ($I > 10^{15}\,\mathrm{W\,cm^{-2}}$). Particular attention was given to inverse bremsstrahlung, resonance absorption, vacuum (or Brunel) heating, and relativistic $\vec{j} \times \vec{B}$ heating. It was noted that as the electrons absorb the overwhelming majority of energy over short timescales, they can be accelerated and so the electrons themselves emit radiation. This was briefly explored in the context of high harmonic generation. It is currently left as an open problem that the ponderomotive regime may have an upper limit in terms of intensity, a problem that will be discussed in

detail in Chapters 4 and 5.

Chapter 2 was concluded with a brief exposition of some laser-driven ion acceleration schemes. It was discussed how with pico- and nano-second laser pulses, the timescale of the dynamics is sufficiently long to accelerate ions via a variety of mechanisms. Prevalent mechanisms such as target normal sheath acceleration, radiation pressure acceleration, and breakout afterburner were described. It was noted, however, that these mechanisms either yield broadband ion spectra or require currently unattainable intensities to produce monoenergetic ion spectra. In contrast, it is the desire of the scientific community to be able to produce narrowband high-energy proton/ion beams from the interactions of a $1\,\mu$m laser with plasma. It is this question that is the subject of Chapter 3.

# Chapter 3

# Particle Acceleration in "Mid-Density" Plasma

As has been alluded to in the previous chapter, the main bulk of currently understood ion acceleration mechanisms yield broadband energy spectra [117]. This makes extracting meaningful quantitative information from diagnostics such as proton radiographs difficult [102]. To simplify the analysis, and allow experiments to obtain more quantitative data via proton radiography, it is desirable to produce monoenergetic ion spectra. While Radiation Pressure Acceleration has been shown to achieve this using $10\,\mu$m $CO_2$ lasers [22], it is incredibly difficult to achieve the same results on the higher-intensity $1\,\mu$m systems that dominate experimental high energy density physics research. One potential candidate to deliver a solution, or a part of a solution, to this problem is Collisionless Shock Acceleration (CSA) [109, 118]: a mechanism that can only be investigated experimentally on $1\,\mu$m laser systems using low-density solid targets, i.e. foams.

The structure of this chapter is as follows: firstly, the mechanism of CSA is described in physical and mathematical terms. A simpler mathematical model that captures the results of the CSA model (originally devised by Cairns *et al.* [55, 56]) is

discussed and given a more complete description and solution than is currently available in the literature. The results of this model, when applied to ion acceleration are presented, and the parameter space over which the model predicts CSA to be viable is plotted and discussed with reference to the performance capabilities of various high-power laser systems available worldwide [119]. The chapter is then concluded with the outline of an experiment design proposal, that is due to be conducted in November 2019 on the Vulcan Target Area West system at the Central Laser Facility [44].

## 3.1 Collisionless Shock Acceleration

Collisionless Shock Acceleration (CSA), as has been mentioned above and in the previous chapter is a potential acceleration mechanism that could yield high energy, narrowband proton sources that could be used for a wide variety of applications. In the context of this discussion, and indeed the wider field, CSA describes the acceleration of ions by a collisionless electrostatic shock. Here, "collisionless" is taken to mean that the longitudinal width of the shock (i.e. the width of the shock front) is narrow, on the order of five Debye lengths or less. In this case, a particle within the plasma can cross the shock front without colliding with another particle. Shocks of this type are often referred to as being "laminar" [55, 120], in that turbulent effects are either absent or weak relative to the long-range collective effects of the electrostatic fields associated with the shock.

### 3.1.1 Comparing Experimental Data of Radiation Pressure Acceleration to Collisionless Shock Acceleration

One experiment that successfully measured CSA was conducted and reported by Haberberger *et al.* at the University of California - Los Angeles [23]. To better understand the importance of these results, and the radical improvement from RPA-

produced spectra, it is instructive to compare Haberberger *et al.*'s results to those obtained in Palmer *et al.*'s groundbreaking RPA experiment at the Brookhaven National Laboratory that was the first to produce a background-free ion beam from RPA (contrast $> 100\times$) [22]. For the benefit of the reader, this discussion is also summarised in Table 3.1.

The two core differences between the RPA and CSA experiments were the laser intensity and the target density. In the RPA experiment, a broad range of target densities were investigated, with positive results reported for densities from four-to-eight times the critical density; with a laser intensity on the order of $6 \times 10^{15}\,\mathrm{W\,cm^{-2}}$, it should be noted here that it was only possible to drive RPA at such low intensities because the wavelength was $10\,\mu$m, and so the value of $a_0$ as given in Equation 2.27 was still sufficient to drive radiation pressure acceleration. Radiation Pressure Acceleration then produced quasi-monoenergetic ion spectra with approximately symmetric peaks centred on 0.4-1.2 MeV and a spread of approximately 4%. These results matched well with the prediction that the energy should scale like the kinetic energy of a particle whose velocity is twice the hole boring velocity of the laser pulse through the plasma (*cf.* Equations 2.84 & 2.85). Most notably, the prediction that the energy should scale linearly with $I/n_\mathrm{e}$ matched well with Palmer *et al.*'s data regardless of which parameter – laser intensity or target density – was varied.

In contrast, the CSA experiment at UCLA used a more intense laser ($I \approx 6.5 \times 10^{16}\,\mathrm{W\,cm^{-2}}$), and reported results over a narrower range of target densities: only ranging from $3n_\mathrm{c}$ to $5n_\mathrm{c}$. Not only did Haberberger *et al.* record ion energy spectra with significantly higher energies (ranging from 14 MeV up to 22 MeV), they also measured spectra that had narrower and, sometimes, distinctly anti-symmetric peaks. The width of the peaks was only 1% of the peak energy, and some of the peaks appear to be truncated so that there is a sharp cut-off in energy on the high-energy side of the peak in the distribution. This led Haberberger *et al.* to postulate that the protons

| Parameter/Result | RPA @ Brookhaven | CSA @ UCLA |
|---|---|---|
| Laser Wavelength | $10\,\mu$m | $10\ \mu$m |
| Laser Intensity | $6 \times 10^{15}\,\mathrm{W\,cm^{-2}}$ | $6.5 \times 10^{16}\,\mathrm{W\,cm^{-2}}$ |
| Pulse Train Timings | 6 ps pulses<br>25 ps separation | 3 ps pulses<br>18 ps separation |
| Target Species | $H_2$ | $H_2$ |
| Target Density | up to $10^{20}\,\mathrm{cm^{-3}}$<br>$(4n_c < n_e < 8n_c)$ | up to $6 \times 10^{19}\,\mathrm{cm^{-3}}$<br>$(3n_c < n_e < 5n_c)$ |
| Peak Ion Energy | 0.4-1.2 MeV | 14-22 MeV |
| Spectral Spread | $\sim$4% | $\sim$1% |
| Spectral Shape | Roughly symmetric peak | Sometimes truncated on the high-energy side of the peak |

Table 3.1: A comparison of the parameters and results of the RPA experiment conducted by Palmer *et al.* [22] and the CSA experiment conducted by Haberberger *et al.* [23]

were accelerated by reflecting from a narrow electrostatic shock[1], i.e. Acceleration due to a Collisionless Shock.

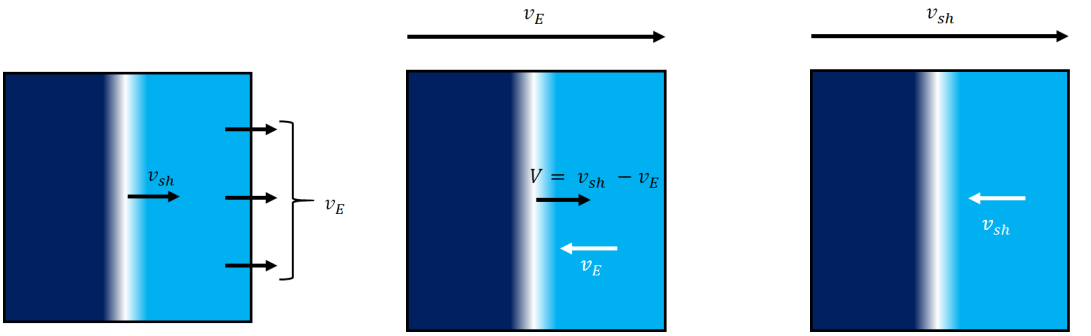
### 3.1.2 A Model for Collisionless Shock Acceleration

One of the most prevalent theoretical models for CSA is that of Fiuza *et al.* [109]. This section draws largely on their model, but uses a non-relativistic version for simplicity and illustrative purposes.

When considering the acceleration of ions by shock waves, there are three principle reference frames of interest: the laboratory frame in which any experimental measurements will be made; the rest frame of the expanding plasma; and the shock frame - the rest frame of the propagating shock front (as depicted in Figure 3.1).

When considering the shock frame, similarly to the hole-boring model discussed for RPA, the ions are expected to be reflected specularly at a speed of $v_{\mathrm{sh}}$, where $v_{\mathrm{sh}}$

[1]Narrow, here, meaning that the width of the shock front was less than five Debye lengths.




(a) Lab Frame (b) Rest Frame (c) Shock Frame

Figure 3.1: A depiction of the three frames of interest when considering shock acceleration of ions. The shock wave (white) is propagating to the right from a region of high density (dark blue) to a region of lower density (light blue). Black labels indicate the speed of the shock wave in the given frame, white labels indicate the speed of ions ahead of the shock in the given frame. The laboratory (or lab) frame is the frame in which an experimental measurement would take place. The rest frame is the rest frame of the expanding plasma. The shock frame is the rest frame of the shock front.

is the speed of the shock wave in the laboratory frame. This translates to a speed of:

$$v = 2v_{\mathrm{sh}} + v_{\mathrm{E}} \tag{3.1}$$

where $v_{\mathrm{E}}$ is the expansion speed of the plasma in the laboratory frame. Therefore, the energy of the ions $U = \frac{1}{2}m_{\mathrm{i}}v^2$ can be expressed as:

$$U = 2m_{\mathrm{i}}v_{\mathrm{sh}}^2 + 2mv_{\mathrm{sh}}v_{\mathrm{E}} + \tfrac{1}{2}m_{\mathrm{i}}v_{\mathrm{E}}^2 \tag{3.2}$$

To proceed further with this discussion requires determining the constraints on the system that limit the parameter space within which CSA is viable. Firstly, the electrostatic potential across the shock front provides the electric field that reflects the ions incident in the shock frame. In order for this to be possible, the shock speed must be sufficiently slow that the kinetic energy associated with incident ions is less than the potential energy across the shock front. This places an upper limit on the speed of the shock front which manifests as a "critical" Mach number $M_{\mathrm{c}}$. Therefore,

the shock speed at it's fastest could be expressed as:

$$v_{\mathrm{sh}} = M_{\mathrm{c}} c_{\mathrm{s}} \tag{3.3}$$

where $c_{\mathrm{s}} = \sqrt{\Gamma Z k_B t_{\mathrm{e}} / m_{\mathrm{i}}}$ is the speed of sound in the plasma and $\Gamma$ is the adiabatic index of the ion species of the plasma.

There are also constraints on the density profile of the plasma. In order for CSA to be efficient, the density trailing the shock front must significantly exceed the density ahead of the shock front, this ensures that the electrostatic profile across the shock front is sufficient to reflect the ions. Achieving this in practical terms requires targeting plasma that is initially near-critical or very slightly over-critical ($n_{\mathrm{e}} < 5 n_{\mathrm{c}}$). This constrains the un-shocked, expanding plasma to be at a low density, while an incident laser is able to steepen the density profile at its point of incidence sufficiently to create a large density ratio between between the downstream and upstream plasma[2].

To consider the expansion speed of the plasma it is plausible to assume that, to first order, the plasma expands at approximately the sound speed of the plasma with some small perturbation:

$$v_{\mathrm{E}} = c_{\mathrm{s}} + \Delta v \tag{3.4}$$

By then exploiting the kinematic equations (or *suvat* equations: $v = u + at$ and $v^2 = u^2 + 2as$) for linear acceleration from rest:

$$v_{\mathrm{E}} = at \tag{3.5}$$

$$v_{\mathrm{E}}^2 = 2a\delta \tag{3.6}$$

and making the approximation that given a sufficiently small $\Delta v$, $v_{\mathrm{E}}^2 \approx c_{\mathrm{s}}^2$, the linear

[2] "Downstream" and "upstream" are here defined in relation to the shock front.

acceleration of the expanding plasma can be expressed as:

$$a = \frac{c_s^2}{\delta} \tag{3.7}$$

and so the expansion velocity is:

$$v_E = \frac{t}{\delta} c_s^2 \tag{3.8}$$

where, in the above, $a$ is the linear acceleration, $t$ is the time over which the acceleration occurs, and $\delta$ is a skin depth of the density discontinuity and is of the same order as the width of the shock front.

By combining Equations 3.3 and 3.8, and by using the explicit form for the sound speed (assuming $Z = 1$ and $\Gamma = 5/3$)[3], the maximum energy of the ion distribution can be deduced:

$$U = \frac{10}{3} M_c^2 k_B T_e + \frac{20}{3}\sqrt{\frac{5}{3}} M_c \left(\frac{k_B T e}{m_i}\right)^{3/2} \frac{t}{\delta} + \frac{25}{9}\left(\frac{k_B T_e}{m_i}\right)^2 \left(\frac{t}{\delta}\right)^2 \tag{3.9}$$

This agrees, in broad terms, with the result derived by Fiuza *et al.* in that while the numerical pre-factors in front of each term are different, the power-law dependence on $M_c$ and $T_e$ are the same [109][4].

## 3.2 Modelling Electrostatic Shocks with a Sagdeev Potential

While Fiuza *et al.* demonstrated a theoretical model that identified the maximum energy of the ion spectrum, their published work did not provide a theoretical de-

[3]This is equivalent to assuming a Hydrogen plasma where the molecules have dissociated into individual atoms.

[4]It is worth noting that the time, $t$, in Equations 3.5, 3.8 and 3.9 is the time after expansion has started at which the shock instantaneously accelerates the ions in the plasma. In this sense, time is a parameter of the system and not a variable.

scription of the shape of the ion energy distribution. To do this, the work of Cairns *et al.* is considered and developed in a somewhat more complete manner [55, 56][5].

First, the distribution function for an ion population is considered. An upper bound is placed on the reflected ions' energies as if the incident ions are too energetic then they will not be reflected by the shock. This concept can be expressed mathematically by writing an equation that explicitly forces energy to be conserved:

$$\frac{1}{2}m_{\mathrm{i}}v_{\mathrm{refl}}^2 = \frac{1}{2}m_{\mathrm{i}}v^2 + Ze\phi \tag{3.10}$$

Assuming a one-dimensional problem, which is permissible in the limit that the transverse extent of the shock front greatly exceeds its width, and that the electrostatic potential associated with the shock rises monotonically from zero at a point far ahead of the shock to some maximum value, $\phi_{\mathrm{max}}$ at the shock front, the distribution function for the ion population – in the rest frame of the expanding plasma – can be expressed as:

$$\begin{aligned} n_{\mathrm{i}}(\phi,\phi_{\mathrm{max}}) = \frac{n_0}{\sqrt{2\pi}}\int_0^{\infty} \exp\left\{-\frac{m_{\mathrm{i}}}{2k_{\mathrm{B}}T_{\mathrm{i}}}\left(\sqrt{v^2+\frac{2Ze\phi}{m_{\mathrm{i}}}}-V\right)^2\right\}\mathrm{d}v + \\ \frac{n_0}{\sqrt{2\pi}}\int_0^{\sqrt{\frac{2Ze(\phi_{\mathrm{max}}-\phi)}{m_{\mathrm{i}}}}} \exp\left\{-\frac{m_{\mathrm{i}}}{2k_{\mathrm{B}}T_{\mathrm{i}}}\left(\sqrt{v^2+\frac{2Ze\phi}{m_{\mathrm{i}}}}-V\right)^2\right\}\mathrm{d}v \end{aligned} \tag{3.11}$$

where $n_0$ is the bulk density of the plasma. The first integral in this distribution function relates to all of the ions incident on the shock front, including those that

[5]While the structure of this section closely follows the work published by Cairns *et al.*, the mathematics presented here has been worked through independently by the author, and in several places expanded (particularly the sections where analytic solutions are provided for some of the integrals - Cairns *et al.* left the distribution functions to be solved numerically and did not find a fractional form for the ions' distribution function in terms of energy).

| Original label | Normalisation Factor | New label |
|---|---|---|
| $n$ | $1/n_0$ | $\tilde{n}$ |
| $v$ | $\sqrt{k_\mathrm{B}T_\mathrm{i}/m_\mathrm{i}}$ | $\tilde{v}$ |
| $V$ | $\sqrt{k_\mathrm{B}T_\mathrm{i}/m_\mathrm{i}}$ | $\tilde{V}$ |
| $\phi$ | $k_\mathrm{B}T_\mathrm{i}/Ze$ | $\tilde{\phi}$ |
| $T_\mathrm{e}$ | $Z/T_\mathrm{i}$ | $\tilde{T}$ |
| $x$ | $\sqrt{Zn_\mathrm{i}e^2/\epsilon_0 k_\mathrm{B}T_\mathrm{i}}$ | $\tilde{x}$ |

Table 3.2: The set of normalisation factors used to simplify the calculations in this chapter.

pass through the shock and are not accelerated (all viewed in the expanding plasma's rest frame). The second integral describes the reflected part of the energy spectrum, capturing the concept that these ions must have an incident kinetic energy that is low enough to allow the electrostatic potential, $\phi_\mathrm{max}$ to reflect them and accelerate them to form a quasimonoenergetic beam. To make this equation easier to read and manage, a series of normalisations are necessary, as summarised in Table 3.2. Applying these normalisation drastically simplifies Equation 3.11:

$$\begin{aligned}\tilde{n}_\mathrm{i}(\tilde{\phi},\tilde{\phi}_\mathrm{max}) = \frac{1}{\sqrt{2\pi}}\int_0^\infty \exp\left\{-\frac{1}{2}\left(\sqrt{\tilde{v}^2+2\tilde{\phi}}-\tilde{V}\right)^2\right\}\mathrm{d}\tilde{v}+ \\ \frac{1}{\sqrt{2\pi}}\int_0^{\sqrt{2(\tilde{\phi}_\mathrm{max}-\tilde{\phi})}} \exp\left\{-\frac{1}{2}\left(\sqrt{\tilde{v}^2+2\tilde{\phi}}-\tilde{V}\right)^2\right\}\mathrm{d}\tilde{v}\end{aligned} \tag{3.12}$$

To determine the electronic distribution function, it is simplest to recognise that electrons thermalise on much shorter timescales than ions, and so the electrons can be considered to be in a Boltzmann distribution with the limiting condition of quasineutrality:

$$\tilde{n}_{\mathrm{e}}(\tilde{\phi}, \tilde{\phi}_{\mathrm{max}}) = Z\tilde{n}_{\mathrm{i}}(0, \tilde{\phi}_{\mathrm{max}}) \exp(\tilde{\phi}/\tilde{T}) \tag{3.13}$$

The difficulty in solving Equations 3.12 and 3.13 arises from the fact that $\tilde{\phi}_{\mathrm{max}}$ is a non-trivial function of the expansion velocity, shock velocity, and ion and electron temperatures. A common approach to solving equations of this form [55, 56, 109] is to construct a pseudo-potential, eponymously named the Sagdeev potential, $\Phi$ [120]. The Sagdeev potential is defined via the Poisson equation to be:

$$\frac{\mathrm{d}^2\tilde{\phi}}{\mathrm{d}\tilde{x}^2} = -\frac{\partial\Phi}{\partial\tilde{\phi}} \tag{3.14}$$

alternatively in integral form:

$$\Phi(\tilde{\phi}, \tilde{\phi}_{\mathrm{max}}) = \int_0^{\tilde{\phi}} Z\tilde{n}_{\mathrm{i}}(\tilde{\phi}', \tilde{\phi}_{\mathrm{max}}) - \tilde{n}_{\mathrm{e}}(\tilde{\phi}', \tilde{\phi}_{\mathrm{max}})\mathrm{d}\tilde{\phi}' \tag{3.15}$$

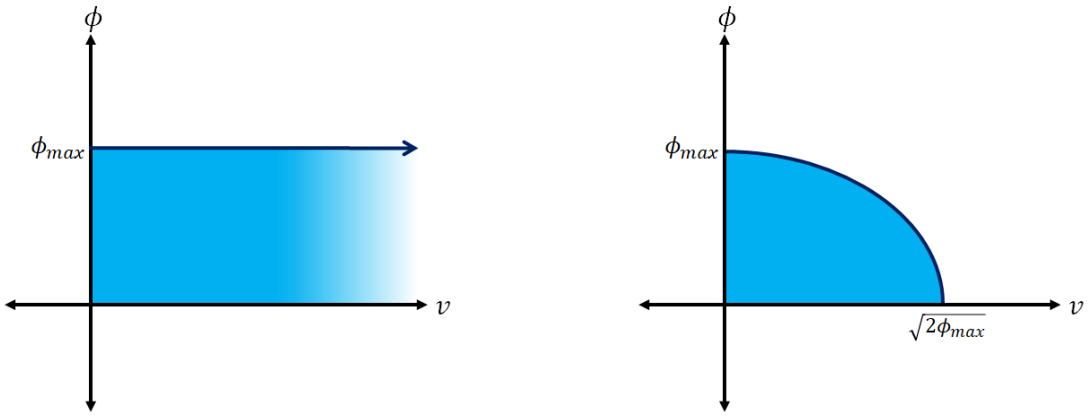
This definition for the Sagdeev potential effectively closes the system of equations as the system is constrained such that $\Phi(0, \tilde{\phi}_{\mathrm{max}}) = \Phi(\tilde{\phi}_{\mathrm{max}}, \tilde{\phi}_{\mathrm{max}}) = 0$. Consequently, this means that the sum and difference of four double integrals is zero:

$$\mathcal{I}_1 + \mathcal{I}_2 - \mathcal{I}_3 - \mathcal{I}_4 = 0 \tag{3.16}$$

where:

$$\mathcal{I}_1 = \frac{Z}{\sqrt{2\pi}} \int_0^{\tilde{\phi}_{\mathrm{max}}} \int_0^{\infty} \exp\left[-\frac{1}{2}\left(\sqrt{\tilde{v}^2 + 2\tilde{\phi}} - \tilde{V}\right)^2\right] \mathrm{d}\tilde{v}\mathrm{d}\tilde{\phi} \tag{3.17}$$

$$\mathcal{I}_2 = \frac{Z}{\sqrt{2\pi}} \int_0^{\tilde{\phi}_{\mathrm{max}}} \int_0^{\sqrt{2(\tilde{\phi}_{\mathrm{max}} - \tilde{\phi})}} \exp\left[-\frac{1}{2}\left(\sqrt{\tilde{v}^2 + 2\tilde{\phi}} - \tilde{V}\right)^2\right] \mathrm{d}\tilde{v}\mathrm{d}\tilde{\phi} \tag{3.18}$$




(a) Surface for $\mathcal{I}_1$ (b) Surface for $\mathcal{I}_2$

Figure 3.2: The surfaces used in the integrals for Equations 3.17 and 3.18. While the integral for $\mathcal{I}_2$ is over a closed surface, the surface for $\mathcal{I}_1$ extends to infinity along one axis.

$$\mathcal{I}_3 = \frac{Z}{\sqrt{2\pi}} \int_0^{\tilde{\phi}_{\max}} \exp\left(\frac{\tilde{\phi}}{\tilde{T}}\right) \mathrm{d}\tilde{\phi} \int_0^{\infty} \exp\left[-\frac{1}{2}\left(\tilde{v}-\tilde{V}\right)^2\right] \mathrm{d}\tilde{v} \tag{3.19}$$

$$\mathcal{I}_4 = \frac{Z}{\sqrt{2\pi}} \int_0^{\tilde{\phi}_{\max}} \exp\left(\frac{\tilde{\phi}}{\tilde{T}}\right) \mathrm{d}\tilde{\phi} \int_0^{\sqrt{2\tilde{\phi}_{\max}}} \exp\left[-\frac{1}{2}\left(\tilde{v}-\tilde{V}\right)^2\right] \mathrm{d}\tilde{v} \tag{3.20}$$

Due to the obvious separated nature of Equations 3.19 and 3.20, it is possible to analytically integrate both $\mathcal{I}_3$ and $\mathcal{I}_4$ to yield:

$$\mathcal{I}_3 = \frac{Z\tilde{T}}{2}\left[1+\mathrm{erf}\left(\frac{\tilde{V}}{\sqrt{2}}\right)\right]\left\{\exp\left(\frac{\tilde{\phi}_{\max}}{\tilde{T}}\right)-1\right\} \tag{3.21}$$

$$\mathcal{I}_4 = \frac{Z\tilde{T}}{2}\left[\mathrm{erf}\left(\sqrt{\tilde{\phi}_{\max}}-\frac{\tilde{V}}{\sqrt{2}}\right)+\mathrm{erf}\left(\frac{\tilde{V}}{\sqrt{2}}\right)\right]\left\{\exp\left(\frac{\tilde{\phi}_{\max}}{\tilde{T}}\right)-1\right\} \tag{3.22}$$

In contrast, the ionic distribution integrals, $\mathcal{I}_1$ and $\mathcal{I}_2$ are clearly not separable into the product of two independent integrals, and so the surface of integration must be more carefully considered. These surfaces are depicted in Figure 3.2. While it transpires that the semi-infinite limit in one of the integrals of $\mathcal{I}_1$ makes finding an

analytic solution an unviable option, the surface for $\mathcal{I}_2$ is perfectly bound and can be solved with relative ease if the order of integration is reversed. This is achieved by modifying the limits such that:

$$\int_0^{\tilde{\phi}_{\max}} \mathrm{d}\tilde{\phi} \int_0^{\sqrt{2(\tilde{\phi}_{\max}-\tilde{\phi})}} \mathrm{d}\tilde{v} \Longrightarrow \int_0^{\sqrt{2\tilde{\phi}_{\max}}} \mathrm{d}\tilde{v} \int_0^{\tilde{\phi}_{\max}-\frac{1}{2}\tilde{v}^2} \mathrm{d}\tilde{\phi} \tag{3.23}$$

By then making the substitution $\psi = \sqrt{2\tilde{\phi} + \tilde{v}^2} - \tilde{V}$, Equation 3.18 can be simplified to:

$$\mathcal{I}_2 = \frac{Z}{\sqrt{2\pi}} \int_0^{\sqrt{2\tilde{\phi}_{\max}}} \int_{\tilde{v}-\tilde{V}}^{\sqrt{2\tilde{\phi}_{\max}}-\tilde{V}} (\psi + \tilde{V}) \exp\left(\frac{\psi^2}{2}\right) \mathrm{d}\tilde{v}\mathrm{d}\psi \tag{3.24}$$

Equation 3.24 can be integrated analytically with respect to $\psi$, leaving just an integral needing to be performed with respect to $\tilde{v}$:

$$\begin{aligned}\mathcal{I}_2 = \frac{Z}{\sqrt{2\pi}} \int_0^{\sqrt{2\tilde{\phi}_{\max}}} & \exp\left[-\frac{(\tilde{v}-\tilde{V})^2}{2}\right] + \exp\left[-\frac{(\sqrt{2\tilde{\phi}_{\max}}-\tilde{V})^2}{2}\right] + \\ & \tilde{V}\sqrt{\frac{\pi}{2}}\mathrm{erf}\left[\sqrt{\tilde{\phi}_{\max}} - \frac{\tilde{V}}{\sqrt{2}}\right] - V\sqrt{\frac{\pi}{2}}\mathrm{erf}\left[\frac{\tilde{v}-\tilde{V}}{2}\right] \mathrm{d}\tilde{v}\end{aligned} \tag{3.25}$$

Despite being somewhat lengthy and containing an error function in the integrand, Equation 3.25 can be integrated to yield[6]:

[6]The integral of the error function is relatively standard, it is done by parts. The exceptionally brief derivation is given in the Appendix.

$$\mathcal{I}_2 = \frac{Z(1+\tilde{V}^2)}{2}\left[\mathrm{erf}\left(\sqrt{\tilde{\phi}_{\max}} - \frac{\tilde{V}}{\sqrt{2}}\right) + \mathrm{erf}\left(\frac{\tilde{V}}{\sqrt{2}}\right)\right] + \frac{Z\tilde{V}}{\sqrt{2\pi}}\exp\left(-\frac{\tilde{V}^2}{2}\right) - \frac{Z\left(\sqrt{2\tilde{\phi}_{\max}} + \tilde{V}\right)}{\sqrt{2\pi}}\exp\left[-\frac{\left(\sqrt{\tilde{\phi}_{\max}} - \tilde{V}\right)^2}{2}\right] \quad (3.26)$$

This leaves just the first integral, $\mathcal{I}_1$ to compute numerically, drastically reducing the potential for introducing numerical errors into the calculation.

Solving Equation 3.16 yields a value for $\tilde{\phi}_{\max}$. Once the maximum of the potential has been determined, the Sagdeev potential, $\Phi$, can be deduced from Equation 3.15 and subsequently the functions $\tilde{n}_{\mathrm{i}}(\tilde{\phi}, \tilde{\phi}_{\max})$ and $\tilde{n}_{\mathrm{e}}(\tilde{\phi}, \tilde{\phi}_{\max})$ can be calculated. To frame this problem into more physically intuitive terms, it is desirable to take the newly determined functions for the electron and ion number densities and substitute them into Poisson's equation (Equation 3.14). This gives the electrostatic potential, and subsequently the number densities as functions of position, $\tilde{x}$.

It is important to note that the nature and indeed the existence of solutions to this set of equations is strongly dependent on the initial parameters of the system. Strong limits are placed on the shock velocity: firstly, and possibly most obviously, the density perturbation that sets up that electrostatic shock must be propagating fast enough to genuinely constitute a shock, i.e. the Mach number of the shock, $M$, must exceed unity. However, the there is also an upper limit placed on the Mach number of the shock. Shock-like solutions for the set of equations presented in this section only exist if the Sagdeev potential satisfies the condition:

$$\Phi \leq 0 \quad (3.27)$$

for all values of the electrostatic potential, $\tilde{\phi} \leq \tilde{\phi}_{\max}$. Cairns *et al.* determined,

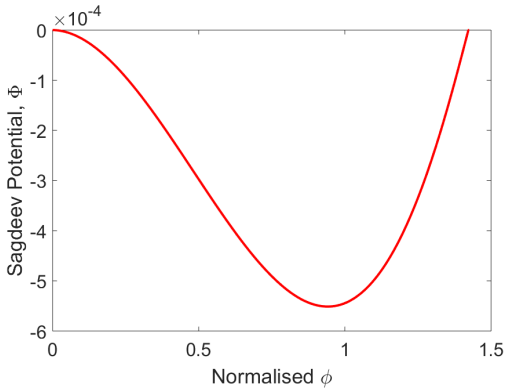
via numerical trial and error that this constrained the Mach number of the shock to $M < 2$ but that as the ratio between electron and ion temperatures tends to unity (i.e. $\tilde{T} \to 1$) the so-called critical Mach number $M_c$ tends to 1.2 [56].

The restriction on the Mach number in this model arises quite naturally from considerations of the physics at play. As the Cairns/Sagdeev approach. The lower limit of the Mach number is reasonably intuitive, as a shock-like scenario cannot occur if the Mach number of the disturbance is too low. The upper limit placed on the Mach number, however, requires more discussion. Given that the model discussed in Equations 3.17 to 3.20 above do not account for collisions, the model quite naturally fails at high Mach numbers, where the disturbance propagates fast enough that turbulence effects are induced. Once inertial forces, such as turbulent collisions, become important the model discussed above becomes insufficient to describe the dynamics of the system. However, if collisions are dynamically significant, the reflected ion spectra will be broadened as the accelerated ions will collide with background plasma and attempt to thermalise with the colder background. and so the acceleration mechanism could no longer be considered to be **collisionless** shock acceleration.

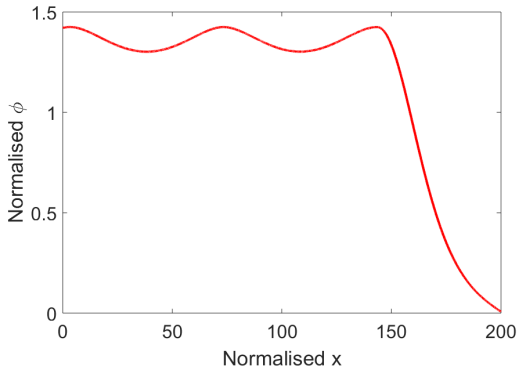
Nonetheless, provided that the the shock's Mach number remains within the required limits, the prescription described above can be used to yield solutions for the Sagdeev potential, electrostatic potential, and electric field, as can be seen in Figure 3.3.

## 3.3 Obtaining the Energy Distribution from Collisionless Shock Acceleration

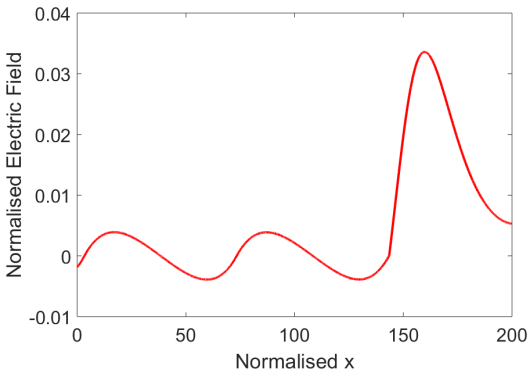
As hinted at above, one of the benefits of using the distribution function approach described above is that the distribution function can be recast as an energy distribution function that matches the expected signal one would measure when using a




(a) Sagdeev potential




(b) Electrostatic Potential




(c) Electric Field

Figure 3.3: Typical solutions to the model described in this chapter, using initial conditions of $\tilde{V} = 5$ and $\tilde{T} = 16$.

particle spectrometer.

### 3.3.1 Non-Relativistic Distribution

Despite the reality that most shocks propagating through plasma do so at relativistically relevant speeds, the energies of ions reflected from these shocks is still an order of magnitude or more below that of their rest mass energy. Thus, it is still both useful and instructive to consider the non-relativistic scenarios; especially as the results yielded by the two approaches do not radically differ when taking currently achievable parameters as initial conditions.

It is clear from Equation 3.12 that the distribution function for ion number density in terms of the dimensionless variable $\tilde{v}$ is:

$$f(\tilde{v}) = \exp\left[-\frac{\left(\sqrt{\tilde{v}^2 + 2\tilde{\phi}} - \tilde{V}\right)^2}{2}\right] \tag{3.28}$$

Reversing the normalisation applied above, and considering the speed of the reflected ions in the laboratory frame (*cf.* Figure 3.1) yields the "real" speed of the ions:

$$v_{\mathrm{R}} = \sqrt{v^2 + \frac{2Ze\phi}{m_{\mathrm{i}}}} + v_{\mathrm{sh}} + v_E \tag{3.29}$$

which allows for the energy of the ions to be calculated as $U = \frac{1}{2}m_{\mathrm{i}}v_{\mathrm{R}}^2$. To convert from a distribution function in terms of $v$ to one in terms of $U$ requires employing a change of variables:

$$f(U) = \sqrt{\frac{m_{\mathrm{i}}}{2\pi k_{\mathrm{B}} T_{\mathrm{i}}}}\frac{\mathrm{d}v}{\mathrm{d}U}\exp\left[-\frac{m_{\mathrm{i}}}{2k_{\mathrm{b}}T_{\mathrm{i}}}\left(\sqrt{v^2 + \frac{2Ze\phi}{m_{\mathrm{i}}}} - v_{\mathrm{sh}} + v_{\mathrm{E}}\right)^2\right] \tag{3.30}$$

By using the definition of U above, and its derivative:

$$\frac{\mathrm{d}U}{\mathrm{d}v} = \sqrt{2m_{\mathrm{i}}U}\sqrt{1 - \frac{2Ze\phi/m_{\mathrm{i}}}{\left(\sqrt{\frac{2U}{m_{\mathrm{i}}}} - v_{\mathrm{sh}} - v_{\mathrm{E}}\right)^2}} \tag{3.31}$$

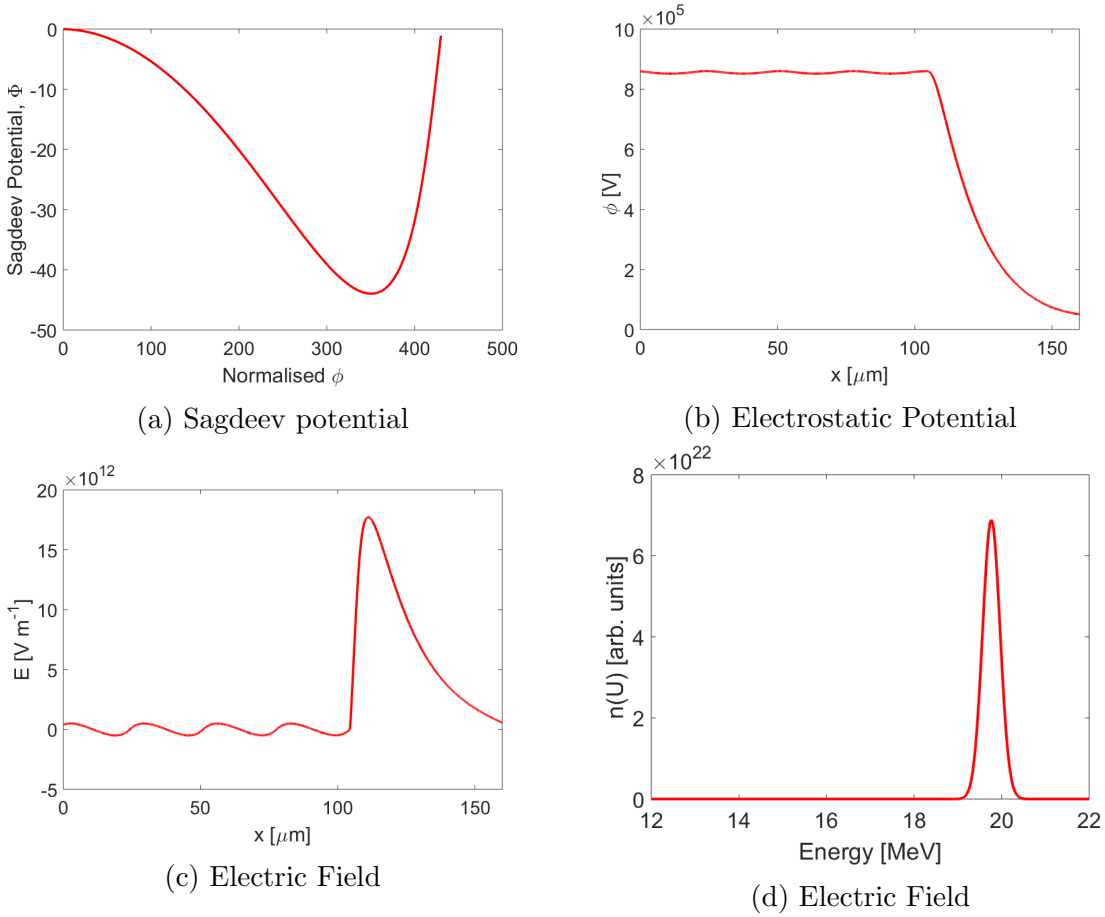
and so the energy distribution function can be expressed as:

$$f(U) = \frac{\exp\left[-\frac{m_{\mathrm{i}}}{2k_{\mathrm{B}}T_{\mathrm{i}}}\left(\sqrt{\frac{2U}{m_{\mathrm{i}}}} - 2v_{\mathrm{sh}}\right)^2\right]}{\sqrt{4\pi k_{\mathrm{B}}T_{\mathrm{i}}U}\sqrt{1 - \frac{2Ze\phi/m_{\mathrm{i}}}{\left(\sqrt{2U/m_{\mathrm{i}}} - v_{\mathrm{sh}} - v_{\mathrm{E}}\right)^2}}} \tag{3.32}$$

By inputting shock and expansion speeds, and ion temperatures into Equation 3.32, an energy distribution can be extracted, an example of which – matching the conditions determined by Haberberger *et al.* [23] – can be seen in Figure 3.4. To model this, an electron temperature of 1 MeV was used, and a corresponding ion temperature of 2 keV with a shock propagating through the plasma with a Mach number of 1.4, and an expansion velocity of $0.1c$. In Haberberger *et al.*'s results, the electron and ion temperatures were determined from particle-in-cell simulations which were designed to match the density measurements and shock velocity measurements that had been made via interferometry during their experimental campaign [23].

### 3.3.2 Relativistic Distribution

While the expansion velocities seen in laser-plasma experiments can be several percent of the speed of light [121, 122], and that even at modest Mach numbers (around unity) shock velocities can tend towards several hundreds of kilometres per second [22, 110, 123, 124]; and it would, therefore, seem prudent to consider a relativistic formulation of the distribution function approach described above; the energy of the reflected ion beam even at potential energies of 50 MeV is orders of magnitude lower than the rest mass energy of a proton. For this reason, the classical approach taken




(a) Sagdeev potential

(b) Electrostatic Potential

(c) Electric Field

(d) Electric Field

Figure 3.4: A solution for the distribution function model presented in this chapter, as applied to the results of Haberberger *et al.* [23]. Most notably, the position of the peak in the energy distribution matches well with Haberberger *et al.*'s measurements.

above is entirely legitimate. However, if one were to consider the prospect of creating energetic ions with a view to applying them to a medical treatment scenario [18], then the energies required exceed 200 MeV. In this setting, the relativsitic dynamics of the system could be critically important and so for the sake of completeness, a relativistic modification to the model described above is briefly outlined here.

Firstly, in a similar vein to the construction of Equation 3.10, the principle of conservation of energy is applied to relativistic particles being reflected from the shock front:

$$\gamma_{\mathrm{refl}} m_{\mathrm{i}} c^2 = Ze\phi_{\mathrm{max}} = \gamma m_{\mathrm{i}} c^2 + Ze\phi \tag{3.33}$$

The limits of integration (for the integral corresponding to the reflected part of the spectrum) can be obtained by considering the kinetic energy, $T = (\gamma - 1)m_{\mathrm{i}}c^2$ of the particles:

$$0 < T < Ze(\phi_{\mathrm{max}} - \phi) \tag{3.34}$$

$$\therefore 1 < \gamma < \frac{Ze}{m_{\mathrm{i}}c^2}(\phi_{\mathrm{max}} - \phi) + 1 \tag{3.35}$$

Thus, Equations 3.11 and 3.13 can be re-cast as:

$$\begin{aligned} n_{\mathrm{i}}(\phi, \phi_{\mathrm{max}}) = n_0 \Bigg\{ & \int_1^{\infty} \exp\left(-\frac{\gamma'(\phi, \gamma, \gamma_{\mathrm{E}})}{\vartheta_{\mathrm{i}}}\right) \mathrm{d}\gamma + \\ & \int_1^{1 + \frac{Ze}{m_{\mathrm{i}}c^2}(\phi_{\mathrm{max}} - \phi)} \exp\left(-\frac{\gamma'(\phi, \gamma, \gamma_{\mathrm{E}})}{\vartheta_{\mathrm{i}}}\right) \mathrm{d}\gamma \Bigg\} \end{aligned} \tag{3.36}$$

$$n_{\mathrm{e}}(\phi, \phi_{\max}) = n_{\mathrm{i}}(0, \phi_{\max}) \exp\left(\frac{Ze\phi}{m_{\mathrm{i}}c^2\vartheta_{\mathrm{e}}}\right) \tag{3.37}$$

where $\gamma'$ is an effective Lorentz factor accounting for the velocity addition seen in Equation 3.11, $\gamma_{\mathrm{E}}$ is the Lorentz factor associated with the speed of expansion, $v_{\mathrm{E}}$, and $\vartheta_{\mathrm{j}} = k_{\mathrm{B}}T_{\mathrm{j}}/m_{\mathrm{i}}c^2$ is a normalised form of the temperature of species j.

By exploiting the equations that combine relativistically relevant velocities (*cf.* the appendix), most critically the Lorentz $\gamma$ factor for a speed $w$ that combines two speeds, $u$ and $v$ [125]:

$$\gamma_w = \gamma_u\gamma_v\left(1 + \frac{uv}{c^2}\right) \tag{3.38}$$

the modifications to the standard distribution function in Equation 3.11 can be easily converted to a relativistic formulation:

$$\sqrt{v^2 + \frac{2Ze\phi}{m_{\mathrm{i}}}} \longrightarrow \gamma + \frac{Ze\phi}{m_{\mathrm{i}}c^2} \tag{3.39}$$

$$\sqrt{v^2 + \frac{2Ze\phi}{m_{\mathrm{i}}}} - v_{\mathrm{e}} \longrightarrow \left(\gamma + \frac{Ze\phi}{m_{\mathrm{i}}c^2}\right)\gamma_{\mathrm{E}}\left(1 + \frac{v_{\mathrm{sh}}v_{\mathrm{E}}}{c^2}\right) \tag{3.40}$$

which results in the final relativistically accurate formulation for the equations describing the ion and electron density distributions:

$$\begin{aligned} n_{\mathrm{i}}(\phi, \phi_{\max}) = n_0 \Bigg\{ &\int_1^{\infty} \exp\left[-\frac{\gamma_{\mathrm{E}}}{\vartheta_{\mathrm{i}}}\left(\gamma + \frac{Ze\phi}{m_{\mathrm{i}}c^2}\right)\left(1 + \frac{v_{\mathrm{sh}}v_{\mathrm{E}}}{c^2}\right)\right] \mathrm{d}\gamma + \\ &\int_1^{1 + \frac{Ze}{m_{\mathrm{i}}c^2}(\phi_{\max} - \phi)} \exp\left[-\frac{\gamma_{\mathrm{E}}}{\vartheta_{\mathrm{i}}}\left(\gamma + \frac{Ze\phi}{m_{\mathrm{i}}c^2}\right)\left(1 + \frac{v_{\mathrm{sh}}v_{\mathrm{E}}}{c^2}\right)\right] \mathrm{d}\gamma \Bigg\} \end{aligned} \tag{3.41}$$

$$n_{\mathrm{e}}(\phi,\phi_{\max}) = n_0 \exp\left(\frac{Ze\phi}{m_{\mathrm{e}}c^2\vartheta_{\mathrm{e}}}\right)\left\{\int_1^{\infty} \exp\left[-\frac{\gamma_{\mathrm{E}}\gamma}{\vartheta_{\mathrm{i}}}\left(1+\frac{v_{\mathrm{sh}}v_{\mathrm{E}}}{c^2}\right)\right]\mathrm{d}\gamma + \int_1^{1+\frac{Ze\phi_{\max}}{m_{\mathrm{i}}c^2}} \exp\left[-\frac{\gamma_{\mathrm{E}}\gamma}{\vartheta_{\mathrm{i}}}\left(1+\frac{v_{\mathrm{sh}}v_{\mathrm{E}}}{c^2}\right)\right]\mathrm{d}\gamma\right\} \tag{3.42}$$

In the relativistic regime, $U = \gamma m_{\mathrm{i}}c^2$ and so the substitution that must be made to obtain the relativistic distribution is remarkably simpler than in the non-relativistic case:

$$f(U) = \frac{1}{m_{\mathrm{i}}c^2}\exp\left[\frac{\gamma_{\mathrm{E}}}{k_{\mathrm{B}}T_{\mathrm{i}}}\left(U+Ze\phi\right)\left(1+\frac{v_{\mathrm{sh}}v_{\mathrm{E}}}{c^2}\right)\right] \tag{3.43}$$

Although it is not transparently obvious from Equation 3.43, in the limit of $v \ll c$, the relations described in Equations 3.39 and 3.40 can be recovered, and so as $\gamma$ tends towards unity, the non-relativistic distribution function as described in Equation 3.32 is recovered.

## 3.4 Mapping the Parameter Space of Collisionless Shock Acceleration

It is clear from the model presented in Section 3.2 that there is a narrow parameter space within which the model predicts CSA to be viable. This is determined by whether or not it is possible to find a solution for $\tilde{\phi}_{\max}$ where Equation 3.16 is satisfied. The parameters that could affect the possibility of retrieving a valid solution for $\tilde{\phi}_{\max}$ are, plausibly, the electron and ion temperatures and the speed of the shock. These are most easily combined into two variables: the normalised temperature $\tilde{T} = ZT_{\mathrm{e}}/T_{\mathrm{i}}$,

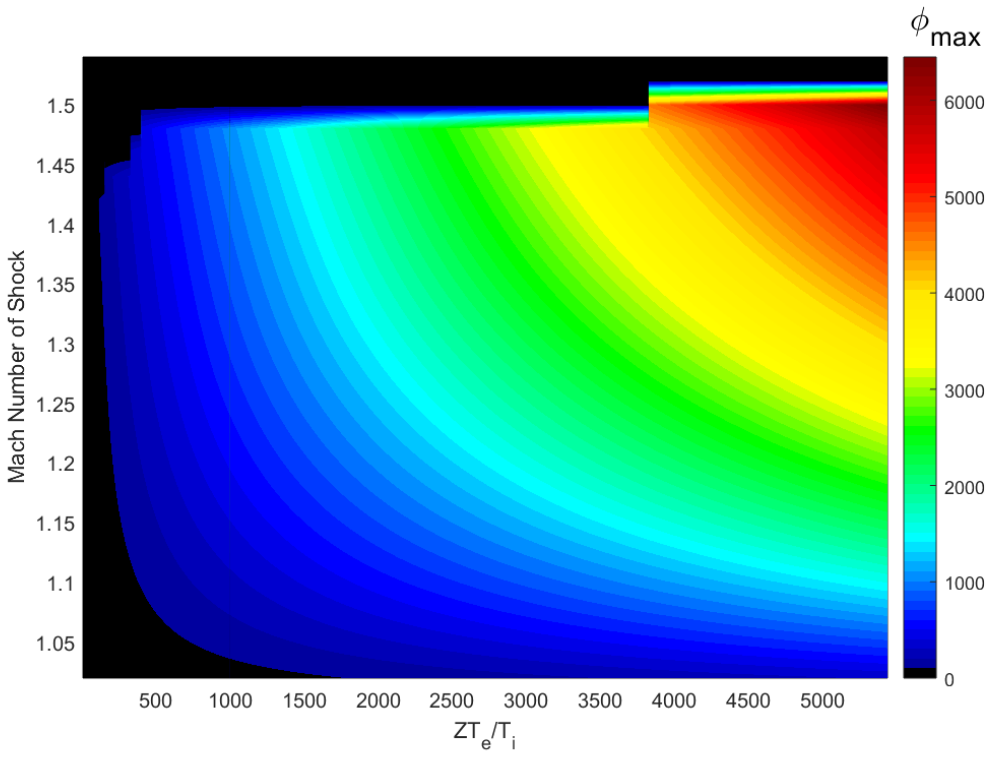



Figure 3.5: The viable parameter space for Collisionless Shock Acceleration, bounded in terms of the electron:ion temperature ratio, $\tilde{T}$, and the Mach number of the shock, $M$. CSA is not viable for $\tilde{T} < 6$, and it can be seen that as the temperature ratio is increased, the range of acceptable Mach numbers increases from solely $M = 1.26$ to $1 < M < 1.56$. For each viable point in the parameter space, the value of the peak of the normalised electrostatic potential , $\tilde{\phi}_{\max}$, is also given. This indicates, as expected, that higher energies are attainable with CSA by driving higher Mach number shocks. The sharp discontinuities that resemble steps on the upper limit of the surface of the parameter space arise from computational difficulties mapping the space. The presence or absence of a solution is so sensitive on the parameters $M$ and $\tilde{T}$ that small changes in either direction can result in dramatic shifts in the qualitative nature of the results. Probing this upper limit more carefully and at even higher resolution is a promising avenue for future work.

and the Mach number of the shock, $M = \tilde{V}/\sqrt{\tilde{T}}$. The existence of a solution can be determined by considering a series of properties concerning the Sagdeev potential:

1. $\Phi < 0$ for $\tilde{\phi} < \tilde{\phi}_{\max}$
2. $\partial\Phi/\partial\tilde{\phi} = 0$ for some value of $\tilde{\phi} < \tilde{\phi}_{\max}$
3. One would expect, from energy conservation, that the search for a value of $\tilde{\phi}_{\max}$ can be terminated once the search has strayed into territories where the energy associated with the electrostatic potential greatly exceeds the energy associated with the propagation of the shock: i.e. $\tilde{\phi}_{\max} \not\gg M^2\tilde{T}$

By probing the system of integrals in Equations 3.17-3.20 while remaining within the constraints of points 1-3 enumerated above, it is possible to definitively determine the parameter space within which CSA is plausible. This parameter space is plotted in Figure 3.5. It is clear that by increasing the ratio of the electron temperature to the ion temperature, the permissible range of shock Mach numbers increases from an incredibly narrow range centred on $M = 1.26$ to a slightly broader (but still narrow) range of $1 < M < 1.56$. Further, it is unsurprising to note that the maximum value of the potential, $\tilde{\phi}_{\max}$, increases as the Mach number of the driving shock increases, suggesting that CSA will be able to attain higher energies when using more energetic shocks, providing the shock is not so energetic that it induces turbulent dynamics in the system.

Arguably, the most interesting information that can be gleaned from Figure 3.5 is the extent to which current high-power laser systems [119] are capable of probing this parameter space. To investigate these systems, a series of hydrodynamic simulations using the HELIOS code [47] to model the expected plasma temperatures that could be obtained with various long pulse laser systems was conducted[7]. The systems

[7]Long pulse laser systems, in this context, are lasers whose pulse durations are on the order of 1 ns.

considered here are the UCLA system (matching the experiment by Haberberger *et al.* [23]), the Vulcan laser at the Central Laser Facility [44], the Orion laser at the Atomic Weapons Establishment UK [126], the Titan laser at Lawrence Livermore National Laboratory [127], and the Laser MegaJoule-PETawatt Aquitaine Laser at the Commissariat à l'énergie atomique et aux énergies alternatives [128]. The ion and electron temperatures, and sound speeds were extracted from the results of the HELIOS simulations to place the laser systems' capabilities on the parameter space map, by considering typical shock speeds produced with petawatt-class laser systems [22, 23, 55, 56, 109, 118, 124, 129–132], as is depicted in Figure 3.6. From Figure 3.6, it is quite clear that provided a target can be made that will form a plasma at close to the critical density for a 1 $\mu$m laser system (corresponding to approximately $10^{20}\,\mathrm{cm}^{-3}$), there are a number of pre-existing laser systems with which CSA can be experimentally investigated.

## 3.5 Proposed Measurement of Collisionless Shock Acceleration

Having reached the stage of producing Figure 3.6, it is a natural continuation to discuss the workings of a potential experiment to measure CSA-produced ions using a high-power laser system, in this case the Vulcan laser at the Central Laser Facility [44]. This experiment is due to be carried out on the Vulcan laser system at the end of 2019, following a successful application for access to the facility.

### 3.5.1 Target Parameters

As CSA is expected to occur exclusively in near-critical density targets, foams are the ideal candidate for targets for this experiment. Further as protons are the lightest ion available, they are the easiest to accelerate to the highest energies. For these reasons,

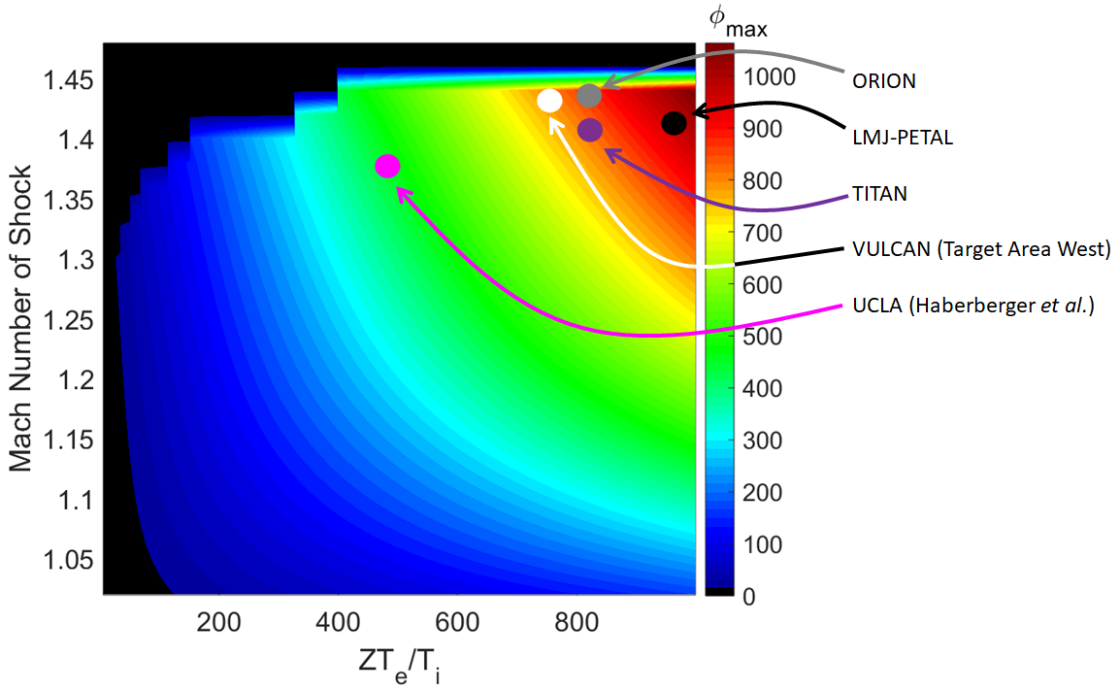



Figure 3.6: A subset of the parameter space portrayed in Figure 3.5 with sections highlighted corresponding to regions attainable (or expected to be attainable) by the UCLA system (pink), the Target Area West facility of the Vulcan laser at the Central Laser facility (white), the TITAN laser system at Lawrence Livermore National Laboratory (purple), the ORION laser system at the Atomic Weapons Establishment UK (grey), and the Laser MegaJoule-PETawatt Aquitaine Laser at the Commissariat à l'énergie et aux énergies alternatives (black).

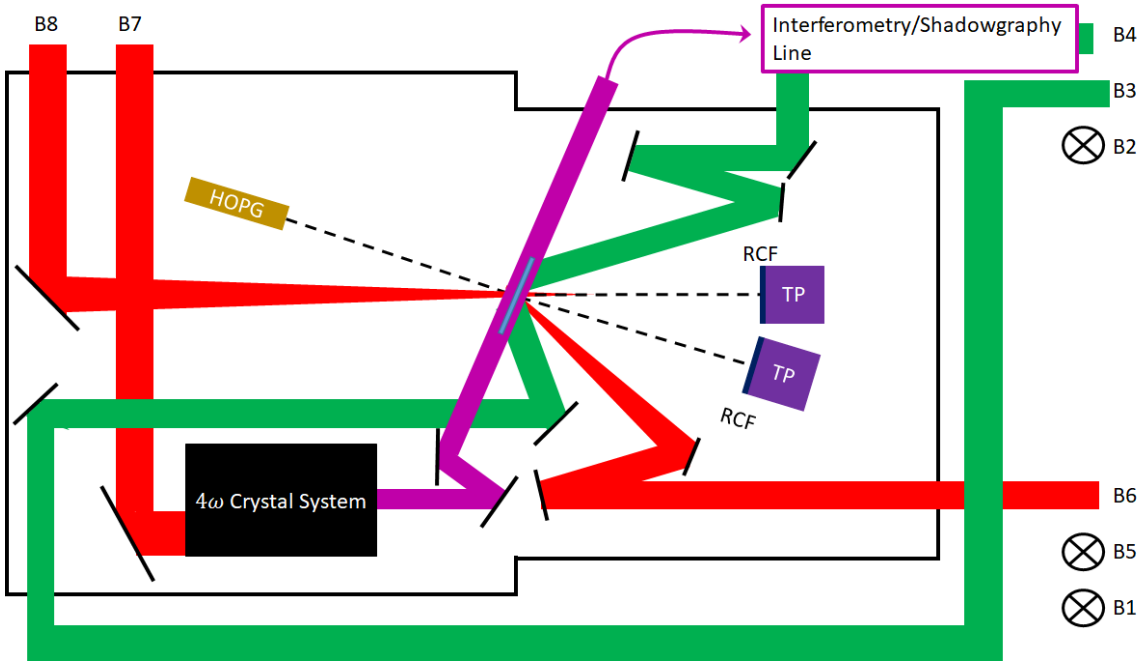



Figure 3.7: A schematic for the proposed experiment to measure Collisionless Shock Acceleration in plastic foam targets on the Vulcan laser facility. Two long pulse beams (B3 & B4 - green) will be converted to the second or third harmonic of their fundamental frequency (corresponding to $\lambda = 1\,\mu$m) and used to heat and ionise a foam target (blue rectangle). A mid- to high-intensity short pulse beam (B8 - red) will be used to drive the shock through the plasma. An additional low-intensity short pulse (B7 - red, latterly dark pink) will be passed through a "$4\omega$ crystal system" to generate a near-UV pulse that can be used for interferometry or shadowgraphy. A contingency long pulse beam (B6 - red) will be set up to generate an ablation front on the rear face of the target in the event that it is too difficult to distinguish TNSA protons from CSA protons. Thomson parabolas (TP - purple) will be set up in the laser-forward and target-normal directions to measure proton energies from accelerations due to CSA and TNSA respectively. Radiochromic film stacks (RCF - dark blue) will be placed in front of the Thomson parabolas to quickly obtain qualitative data about the proton spectra. A HOPG spectrometer (gold) will be used to diagnose the plasma's temperature.

a hydrogen-rich species such as the polyHIPE foam displayed in Figure 1.1 at a mass density of 20-50 $\mathrm{mg\,cm^{-3}}$ (corresponding to 0.9-2.3 times critical density), and 60-150 $\mu$m thick is ideally suited for the purposes of this experiment[8]. This thickness has been determined through numerical simulations, as at targets thinner than 60-150 $\mu$m (dependent on laser intensity), the effect of the high-power short pulse was simply to obliterate the target, and it was consequently impossible to set up an electrostatic shock. In general, it is desirable for the target to be as thin as possible to reduce the chance of the accelerated ions colliding with background plasma and thus broadening the ion spectrum through collisional broadening. In addition to these standard foams, some number of the targets need to be doped with small traces of copper atoms so that a temperature measurement for the plasma can be obtained via x-ray emission spectroscopy.

### 3.5.2 Laser Parameters

The Target Area West facility of the Vulcan laser has six long pulse (1 ns) beams and two short pulse (1-10 ps) beams at its disposal. For the purposes of fully diagnosing the interaction in this experiment, both short pulses (named Beams 7 & 8) and three long pulses (named Beams 3, 4 & 6) are required - a depiction of the use of these beams is in Figure 3.7. The parameters needed for each of Vulcan's beams are summarised in Table 3.3.

### 3.5.3 Diagnostics

A variety of diagnostics are expected to be needed to analyse the interaction:

- Radiochromic film (RCF) stacks to obtain preliminary data about the ion energies [95].

[8]In fact any plastic (CH) species is suitable for the purposes of this experiment, although careful consideration needs to be given to the absorption properties of the material as there is a large variation in the wavelengths of the laser beams proposed for this experiment.

| Parameter | B3 | B4 | B6 | B7 | B8 |
|---|---|---|---|---|---|
| Wavelength | 527 nm/351 nm | 527 nm/351 nm | 1053 nm | 1053 nm/263 nm | 1053 nm |
| Pulse duration | 1 ns | 1 ns | 1 ns | 3-5 ps | 3-5 ps |
| Energy | 70 J | 70 J | 50 J | 70 J | 100-120 J |

Table 3.3: The various laser beam parameters for the proposed experiment investigating Collisionless Shock Acceleration on the Vulcan laser in teh Target Area West facility.

- Thomson parabolas to obtain precise quantitative information about the fast proton energies [133].
- A Highly-Ordered Pyrolytic Graphite (HOPG) spectrometer to measure the x-ray emission from copper-doped CH foams [134].
- Interferometry and shadowgraphy lines based off the propagation of Beam 7 (converted to the $4^{\text{th}}$ harmonic) to measure the density of the plasma and potentially observe the shock propagation.

### 3.5.4 Target Chamber & Campaign Design

A schematic of the proposed target chamber layout is displayed in Figure 3.7. Two of Vulcan's long pulse beams (B2 & B4) will be converted to the second or third harmonic and used to heat and ionise the target. Although one beam would be sufficient for the purposes of reaching the necessary temperatures, the addition of a second beam will allow for symmetric heating of the foam, thus increasing the homogeneity of the plasma. A short pulse beam at fundamental frequency (B8) will then be incident onto the target with some angle of incidence, $\theta < 30°$. This should drive the electrostatic shock through the target which will accelerate ions in the plasma. It is intended to perform a scan of the dependence of CSA on incident laser intensity ranging from

$I = 10^{17}\,\mathrm{W\,cm^{-2}}$ to $I = 10^{20}\,\mathrm{W\,cm^{-2}}$. The second short pulse (B7) will be converted to the $4^{\mathrm{th}}$ harmonic and used to image interferograms and shadowgrams in the line of sight transverse to the shock front.

The accelerated ions will be collected and measured by both RCF stacks and Thomson parabolas. In the event that it is difficult to distinguish shock-accelerated ions from a TNSA background, an additional "low"-energy long-pulse beam (B6) will be used to generate an ablation front on the rear face of the plasma, thus preventing the formation of a sheath field and inhibiting TNSA. It is to be expected that setting up an ablation front on the rear surface would lead to a broadening of the spectrum, as the shock will enter a region of lower density at the rear edge of the target that is correspondingly cooler. Therefore, in this region, the Mach number of the shock will be higher, and so turbulent and collisional effects will be induced that could broaden the ion spectrum. While this will likely complicate the data analysis, it is not necessarily fatal to the working of the CSA mechanism itself in the region of the bulk plasma. In order to diagnose information about the properties of the plasma, the interferometry line can be terminated at a streak camera to obtain time-resolved information about the shock front's propagation through the plasma. To obtain temperature measurements, the standard CH foam target will be replaced by a copper-doped variant ($CH_{1-x}Cu_x$) and a HOPG will be used to collect the x-ray emission spectrum from the plasma. By measuring this emission, in particular the ratio of the copper $K_\alpha$ and $K_\beta$ lines, and comparing this with simulations using atomic-transition codes such as PrismSPECT [135] and FLYCHK [136], the electron temperature of the plasma can be inferred.

By measuring the electron temperature and number density, ion energy spectra in two independent directions, and the shock front speed; and by inferring the ion number density and temperature from hydrodynamic simulations, this experiment aims to fully validate the model presented in this chapter and establish this acceleration

mechanism as a potential source for proton radiography and heating.

## 3.6 Summary

In this chapter, the case for developing a monoenergetic or quasimonoenergetic ion source was put forward, and Collisionless Shock Acceleration was suggested as a potential candidate for the generation of such ion spectra. The experimental results of a campaign that measured Radiation Pressure Acceleration [22] was compared to a campaign that measured CSA [23], both using 10 $\mu$m $CO_2$ laser systems. Given that petawatt class laser systems operate almost exclusively at a wavelength of 1 $\mu$m [119], it is necessary to develop a model that describes CSA so that the mechanism can be successfully transposed from the 10 $\mu$m system to petawatt-class systems.

To match this need for a theoretical model, the theory proposed by Fiuza *et al.* was discussed [109]. While it was noted that their work produced an estimate of the ion energy that was attainable, it did not predict form of the distribution function of the ions and, therefore, additional modelling is desirable to complete the picture of CSA. With this in mind, a distribution function approach was presented, closely following the concepts introduced by Cairns *et al.* [55, 56]. Care was taken to explain the physical meaning behind each step in the distribution function approach and it was demonstrated that the main bulk of the equations used in this approach are solvable analytically. Most notably, an analytic form for the distribution function of the ions was attained.

This was followed by a brief segue to present a form of the distribution function approach that included relativistic effects. This approach also yielded an analytic form for the energy distribution function. It was, however, noted that given the maximum energy expected to be attained by petawatt-class laser systems through CSA falls far short of the proton rest mass energy, the classical model is entirely

sufficient for the purposes of this thesis.

Given that throughout the chapter it had been hinted that the parameter space within which CSA is viable is somewhat limited, a full mapping of the parameter space was then derived and presented. It was seen that increasing the ratio of the electron temperature to the ion temperature broadened the parameter space but that even at its widest, CSA is only viable for shocks that propagate with Mach numbers in the range $1 < M < 1.56$. With a view to possible experiments investigating CSA using pre-existing $1\,\mu$m systems, the areas of the parameter space that could be reached with various current systems, including the Vulcan laser at the Central Laser Facility, were investigated and displayed. It was seen that such systems are expected to occupy the upper limit of the parameter space, the region where the highest energy ions are expected to be produced.

With the positive result that the CSA parameter space is accessible to the Vulcan laser system confirmed, this chapter concluded with a discussion of a proposed experiment to use the Vulcan laser's Target Area West to measure the CSA-produced protons on a high-power $1\,\mu$m laser system. For future work, it is hoped that this experiment - due to be conducted towards the end of 2019 - will yield positive results and motivate developing CSA as a platform for proton radiography and heating on laser systems operating at ever-increasing energies and intensities. CSA is a potentially valuable platform for radiography, as ions are expected to be accelerated from the shock front, as though from a point source, making the proton trajectories easier to infer from radiographs, and reducing the risk of caustic features being found in the image data [102]. Further, the energies that are expected to be attainable with CSA should be sufficient to probe very high-density matter, such as that found in ICF implosions. It is also expected that high numbers of protons can be generated from this mechanism, a vital consideration of radiography where the signal must be sufficiently strong to distinguish from the background.

However, before committing to proton acceleration on the next generation of laser systems - beyond the petawatt class - it is vitally important to understand how laser-energy absorption processes at these unprecedented intensities might operate. It is this topic of absorption beyond the ponderomotive regime that forms subject of the rest of this thesis, as investigations into ion acceleration at extreme intensities require the first step of how electrons are accelerated to be well understood in order to facilitate progress.

# Chapter 4

# Beyond the Ponderomotive Regime - the Zero Vector Potential Absorption Mechanism

The next generation of high-power optical lasers promises to open experimental laser-plasma physics into a new regime, only just touched upon by the Hercules laser facility at the University of Michigan [60]. In this regime, it might be expected that the laser-plasma absorption mechanisms discussed in Chapter 2 are no longer dominant. One potential newly dominant absorption mechanism is the Zero Vector Potential (ZVP) absorption mechanism, originally proposed and described in one dimension by Baeva *et al.* [57]. Fully understanding the workings of this mechanism, and indeed the post-ponderomotive regime[1] itself, requires an extension of this theory into higher dimensions. The structure of this chapter, therefore, is as follows: firstly, the concept of a post-ponderomotive regime is explored and defined; this is followed by an exposition of a 3D ZVP theory. An intuitive model for electron energy scaling is presented and the predictions of the theoretical work contained in this chapter are

[1]The justification for labelling this regime "post-ponderomotive" will be given in this chapter.

validated by 2D PIC simulations. Results indicating the efficiency of ZVP absorption are presented, and the brief outline of a potential experiment that could be conducted on the Hercules laser facility conclude the chapter. The overwhelming bulk of the material contained within this chapter is based on recently published work [58] which itself builds on the original paper by Baeva *et al.* [57].

## 4.1 The Post-Ponderomotive Regime

The ponderomotive absorption mechanisms described in Chapter 2 have been seen to accurately predict and model the absorption of laser-energy by plasma over a wide range of plasma densities and laser intensities. However, as laser intensities are increased, it becomes necessary to be mindful of both the laser intensity and the relativistically-corrected plasma electron density before making assertions or predictions about the system's dynamics. Of particular interest is the normalised vector potential, $a_0$:[2]

$$a_0 = \frac{eA}{m_e c} \tag{4.1}$$

where $A$ is the vector potential of the laser pulse, as defined in the Lorenz gauge:

$$\nabla \cdot \vec{A} + \frac{1}{c^2}\frac{\partial \phi}{\partial t} = 0 \tag{4.2}$$

where $\phi$ is the scalar electromagnetic potential. The Lorenz gauge yields wave equations for the electromagnetic potentials:

$$\Box^2 \vec{A} = -\mu_0 \vec{J} \tag{4.3}$$

$$\Box^2 \phi = -\frac{Qn}{\epsilon_0} \tag{4.4}$$

[2] $a_0$ is defined here slightly differently, but entirely equivalently to Equation 2.27

where $\vec{J}$ is the current density in the system, and the d'Alembertian operator, $\Box$, is defined as:

$$\Box^2 = \nabla^2 - \frac{1}{c^2}\frac{\partial^2}{\partial t^2} \tag{4.5}$$

These equations can be solved to yield an integral form of the vector potential:

$$\vec{A}(\vec{r},t) = \frac{\mu_0}{4\pi}\int \frac{\vec{J}(\vec{r}',t)}{|\vec{r}-\vec{r}'|}d^3\vec{r}' \tag{4.6}$$

In addition to the normalised vector potential, another parameter of interest is the so-called relativistic similarity parameter, $S$, that indicates the ratio of the electron density to the relativistically corrected critical density [137]:

$$S = \frac{n_e}{a_0 n_c} \tag{4.7}$$

In the regime where both $a_0$ and $S$ exceed unity; the plasma frequency, $\omega_{\mathrm{p}}$, will be much greater than the incident laser frequency, $\omega_{\mathrm{L}}$. Thus, it is to be expected that the plasma electrons are able to respond adiabatically to ponderomotive forces such as the $\vec{j}\times\vec{B}$ force, i.e. the timescale over which the electrons are able to respond to electromagnetic forces is so short that the electrons are able to respond to the laser pulse without the laser causing the electron wave to break and heat the plasma collisionally. Therefore, it is predicted that the dominant absorption process in this regime will not be ponderomotive, i.e. the laser-plasma dynamics have entered a post-ponderomotive regime.

## 4.2 Propagating Vector Potential "Zeroes"

The effect of entering a post-ponderomotive regime where the electrons can respond adiabatically to the incident laser pulse is to displace the electrons in the skin layer of the plasma from the ion background leaving behind an uncompensated positive

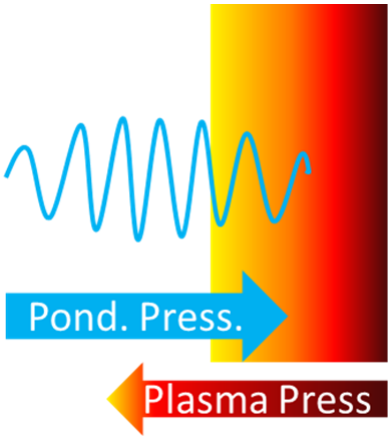



Figure 4.1: A pictorial representation of the competing effects: radiation pressure from the incident laser pulse (cyan) and electrostatic plasma pressure due to the expansion of the plasma (red fading to yellow) into vacuum. These two competing pressures form a potential well that effectively confines the plasma electrons.

space charge. The electrons then find themselves confined within a potential well. This potential well, as seen in Figure 4.1, is set up by an adiabatic balance of the ponderomotive pressure from the laser pulse, and the electrostatic pressure arising from the uncompensated positive space charge. To achieve such an adiabatic balance requires the interaction of a very intense laser pulse ($a_0 > 1$) with a relativistically over-dense plasma ($S > 1$) that has a very short scale-length ablation front (i.e. the skin depth, $\delta \ll \lambda$).

To fully grasp the workings of the ZVP absorption mechanism, it is necessary to investigate the nature of this potential well which can be described by the Hamiltonian, $\mathcal{H}$:

$$\mathcal{H} = c\sqrt{|\,\vec{p}\,|^2 + m_e^2 c^2} + e\phi \tag{4.8}$$

where the first term in the Hamiltonian arises from a simple extraction of energy from the invariant of the relativistic 4-momentum, $\mathbf{P}^\mu = (U/c, \vec{p})$:

$$\mathbf{P}^\mu \cdot \mathbf{P}_\mu = \frac{U^2}{c^2} - |\,\vec{p}\,|^2 = m^2 c^2 \tag{4.9}$$

Here, as throughout the thesis, the inner product of relativistic 4-vectors is defined using the Minkowski metric [125].

The second term in the Hamiltonian of Equation 4.8 is simply the contribution of the spatial electrostatic potential to the electron's energy. By breaking the 3-momentum term in Equation 4.8 into three orthogonal components, and recognising that the momentum parallel to the direction of polarisation of the vector potential must be equal to $eA$ as a consequence of momentum conservation, the Hamiltonian can be re-cast into a more explicit form:

$$\mathcal{H} = c\left[p_{\text{prop}}^2 + p_{\perp}^2 + e^2A^2 + m_e^2c^2\right]^{1/2} + e\phi \tag{4.10}$$

where $p_{\text{prop}}$ and $p_{\perp}$ are the components of the electron's 3-momentum in the direction of laser propagation and the third – mutually orthogonal – axis, respectively.

From Equation 4.10, it can be seen that should the vector potential, $A$, pass through zero within the plasma then the potential well confining the electrons could be disrupted and the adiabatic state of the electrons broken. Proceeding further with this hypothesis requires formulating the problem mathematically.

If one considers the case of an obliquely incident Gaussian pulse on a plasma expanding in the negative $\hat{y}$-direction at a speed, $u$, with a very short ablation front scale-length, $\delta \ll \lambda$; the direction of propagation of the laser pulse can be confined to the $\hat{x}$-$\hat{y}$ plane without loss of generality, as depicted in Figure 4.2. The angle of incidence, $\theta$, is therefore measured with respect to the $\hat{y}$-axis, and the angle polarisation, $\varphi$, with respect to the $\hat{z}$-axis.

In the rest frame of the expanding plasma (referred to more concisely as "the rest frame" for the remainder of this chapter, and denoted as the frame with primed variables), the vector potential, $\vec{A}'$, of a Gaussian laser pulse can be described as [39]:

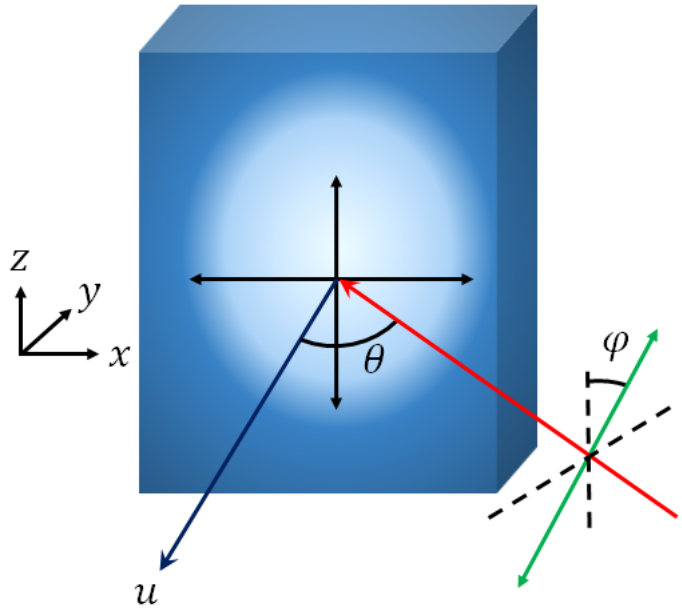



Figure 4.2: A schematic indicating the coordinate system used to describe the Zero Vector Potential absorption mechanism. A laser pulse (red) propagating in the $\hat{x}-\hat{y}$ plane is incident on an ablating plasma (blue) with an angle of incidence, $\theta$, and an angle of polarisation of $\varphi$ with respect to the $\hat{z}$-axis. The plasma is ablating in a direction anti-parallel to the $y$-axis at a speed, $u$.

$$\vec{A}'(R,l,t) = A_0\hat{P}\frac{w_0}{w(l)}\exp\left[-\left(\frac{R^2}{w(l)^2}+\frac{t^2}{\tau^2}+\frac{l}{\delta}\right)\right]\cos\left[\omega t - k\left(l+\frac{R^2}{2\mathcal{R}(l)}\right)+\psi(l)\right] \tag{4.11}$$

where $R$ is the perpendicular distance from the axis of propagation, $l$ is the distance along said axis from the position of best focus, $\hat{P}$ is the unit vector in the direction of the polarisation of the laser pulse, $w_0$ is the beam waist of the pulse at best focus, $w(l)$ is the beam waist away from focus, $\tau$ is the temporal duration of the pulse, $\mathcal{R}(l)$ is the radius of curvature of the pulse, and $\psi(l)$ is the Gouy phase of the pulse. The forms of these functions are as follows:

$$\hat{P} = \cos\varphi\cos\theta\hat{x} + \cos\varphi\sin\theta\hat{y} + \sin\varphi\hat{z} \tag{4.12}$$

$$w(l) = w_0\sqrt{1+\left(\frac{l}{z_\mathrm{R}}\right)^2} \tag{4.13}$$

$$\mathcal{R}(l) = l\left[1+\left(\frac{z_\mathrm{R}}{l}\right)^2\right] \tag{4.14}$$

$$\psi(l) = \arctan\left(\frac{l}{z_\mathrm{R}}\right) \tag{4.15}$$

where $z_\mathrm{R} = kw_0^2/2$ is the Rayleigh range of the pulse.

In the coordinate system given in Figure 4.2, the distances $R$ and $l$ can be expressed as:

$$R^2 = (x'\cos\theta - y'\sin\theta)^2 + z'^2 \tag{4.16}$$

$$l^2 = x'^2 + y'2 \tag{4.17}$$

and so the vector potential in the rest frame of the plasma can be expressed as:

$$\vec{A'} = A_0\frac{1}{\sqrt{1+\frac{x'^2+y'^2}{z_\mathrm{R}'^2}}}\exp\left(-\frac{(x'\cos\theta - y'\sin\theta)^2+z'^2}{w_0^2\left[1+\frac{x'^2+y'^2}{z_\mathrm{R}'^2}\right]} - \frac{\sqrt{x'^2+y'^2}}{\delta} - \frac{t'^2}{\tau^2}\right)$$
$$\times\cos\left[\omega t' - k'\left(\sqrt{x'^2+y'^2} + \frac{(x'\cos\theta - y'\sin\theta)^2+z'^2}{2\left(1+\frac{z_\mathrm{R}'^2}{x'^2+y'^2}\right)\sqrt{x'^2+y'^2}}\right) - \arctan\left(\frac{\sqrt{x'^2+y'^2}}{z_\mathrm{R}'}\right)\right] \tag{4.18}$$

To be able to consider what happens in the laboratory frame, i.e. the frame of any potential experiment, it is necessary to perform a simple Galilean transform to change from primed to un-primed variables:

$$\begin{pmatrix} x' \\ y' \\ z' \\ ct' \end{pmatrix} = \begin{pmatrix} 1 & 0 & 0 & 0 \\ 0 & 1 & 0 & \beta \\ 0 & 0 & 1 & 0 \\ 0 & 0 & 0 & 1 \end{pmatrix}\begin{pmatrix} x \\ y \\ z \\ ct \end{pmatrix} \tag{4.19}$$

where $\beta = u/c$.

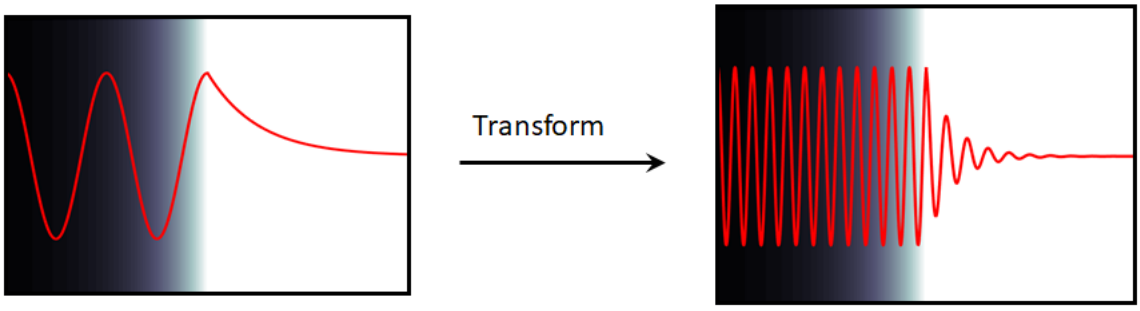



Figure 4.3: Portrayal of a laser pulse (red) propagating through vacuum (black) into a plasma (fading white) with a short ablation front scale-length and a critically overdense bulk. In the rest frame of the expanding plasma (left panel), the incident laser pulse becomes evanescent on entering the bulk plasma. In contrast, in the laboratory frame (right panel), the laser pulse completes several oscillations within the bulk plasma before completely decaying.

One consequence of the transformation in Equation 4.19 is that there is a Doppler shift in the wavelength of the laser pulse such that:

$$\frac{\lambda'}{\lambda} = \frac{k}{k'} = \frac{z_{\mathrm{R}}}{z'_{\mathrm{R}}} = 1 - \beta\cos\theta \tag{4.20}$$

By applying Equations 4.19 and 4.20 to Equation 4.18, a result for the form of the vector potential in the lab frame can be obtained:

$$\vec{A} = A_0 \frac{1}{\sqrt{1 + \frac{(1-\beta\cos\theta)^2[x^2+(y+ut)^2]}{z_{\mathrm{R}}^2}}} \exp\left[-\frac{1}{\delta}\sqrt{x^2+(y+ut)^2}\right] \cos\left[\mathcal{G}(x,y,z,t)\right] \tag{4.21}$$

where the function $\mathcal{G}$ has the form:

$$\mathcal{G} = \omega t - k\left[\sqrt{x^2+(y+ut)^2} + \frac{[x\cos\theta - (y+ut)\sin\theta]^2 + z^2}{2\left(1 + \frac{z_{\mathrm{R}}^2}{(1-\beta\cos\theta)^2[x^2+(y+ut)^2]}\right)\sqrt{x^2+(y+ut)^2}}\right] - \arctan\left[\frac{(1-\beta\cos\theta)\sqrt{x^2+(y+ut)^2}}{z_{\mathrm{R}}}\right] \tag{4.22}$$

Of particular interest in Equation 4.22 is the newly found temporal dependence in the factor associated with the wavevector, $k$. This term permits oscillations in

the vector potential to persist for a few wavelengths into the bulk of the plasma (as depicted in Figure 4.3), whereas in the rest frame of the plasma, the wave becomes instantly evanescent upon reaching the critically over-dense bulk. The persistence of oscillations in the bulk plasma in the laboratory frame means that the potential well described by the Hamiltonian in Equation 4.10 can be violently disrupted by propagating zeroes in the vector potential and so the prospect of a post-ponderomotive absorption mechanism is viable.

## 4.3 Interaction of Electrons with Vector Potential "Zeroes"

It would seem, on first consideration, that the new physics occurring in this post-ponderomotive regime is the disruption of an adiabatic potential well by the propagation of vector potential "zeroes" through the plasma. The processes of interest here, therefore, are how the electrons interact with these propagating "zeroes" and how the energy from the laser pulse is transferred to the plasma.

### 4.3.1 Generating Fast Electrons

To determine how the plasma electrons behave in the vicinity of the vector potential "zeroes" one must consider the relativistic invariant quantity in Equation 4.9. By recognising that $U = \gamma m_e c^2$ where $\gamma = (1-\beta^2)^{-1/2}$ is the Lorentz factor of the electron, then a form for the Lorentz factor can be deduced:

$$\gamma^2 = 1 + \left(\frac{|\vec{p}\,|}{m_e c}\right)^2 \tag{4.23}$$

By splitting the 3-momentum into its orthogonal components: $p_{\mathrm{pol}}$, $p_{\mathrm{prop}}$, and $p_\perp$, a number of simplifications can be made. Firstly, conserving momentum in the

direction of the polarisation of the laser yields $p_{\mathrm{pol}} = eA$. Secondly, if one assumes that the majority of the momentum from the boring effect of the laser pulse [54, 138]goes into the direction of propagation this results in $p_{\mathrm{prop}} \gg p_{\perp}$ and so:

$$\gamma^2 = 1 + a_0^2 + \left(\frac{p_{\mathrm{prop}}}{m_{\mathrm{e}}c}\right)^2 \tag{4.24}$$

and by using the definition relating $\gamma$ to $\beta$:

$$\beta = \sqrt{\frac{a_0^2 + \tilde{p}_{\mathrm{prop}}^2}{1 + a_0^2 + \tilde{p}_{\mathrm{prop}}^2}} \tag{4.25}$$

where $\tilde{p}_{\mathrm{prop}} = p_{\mathrm{prop}}/m_e c$. If the laser pulse is very intense ($a_0 \gg 1$), then the forward momentum of the hole-bored electrons will be very large, i.e. $\tilde{p}_{\mathrm{prop}} \gg 1$. Considering now the instant that the vector potential passes through zero, takes $a_0$ to zero in Equation 4.25 and so yields the result:

$$\beta = \frac{1}{\sqrt{1 + (1/\tilde{p}_{\mathrm{prop}})^2}} \approx 1 - \frac{1}{2}\frac{1}{\tilde{p}_{\mathrm{prop}}^2} \tag{4.26}$$

and so as you take the limit of the electron's forward momentum ever higher:

$$\lim_{\tilde{p}_{\mathrm{prop}} \to \infty} \{\beta\} = 1 \tag{4.27}$$

The physical interpretation of these equations is as follows: the potential well described by the Hamiltonian in Equation 4.10 sets up a pseudo-capacitor system with one "plate" formed by the displaced electron fluid, and the other by the uncompensated positive space charge. When the vector potential passes through zero, one wall of the potential well is violently disrupted and disappears. This allows the electrons in the plasma to cross the region of positive space charge reaching speeds up to the value given in Equation 4.26. The key role of the propagating "zeroes" in the absorption process led Baeva *et al.* to dub this mechanism the Zero Vector Potential

(ZVP) absorption mechanism [57].

In effect, this is entirely analogous to an electron crossing a capacitor and gaining energy by shuttling along the electric field lines. Due to the oscillatory nature of the vector potential, the "zeroes" propagate into the bulk plasma coherently. Consequently, coherent bunches of fast electrons are produced. Each coherent bunch is eventually launched back into the plasma with high momentum as each one is pushed back into the plasma when it encounters a region where the laser pulse is at peak amplitude. The nature of this model leads to three qualitative predictions about the nature of the absorption process:

1. There should be regularly spaced bunches of energetic electrons with momenta in the ***laser-forward*** direction.

2. As the vector potential never passes through zero for circularly polarised pulses, the absorption process should be observed in ***linear polarisation*** only.

3. As the motion of the electron fluid is expected to resemble that of a rapidly oscillating mirror, it is to be expected that high-frequency coherent radiation is emitted - this could manifest itself as ***High Harmonic Generation*** with the typical spectrum as described by Equation 2.82. However, in contrast to conventional HHG which is emitted in the direction of specular reflection of the laser pulse, this coherently generated light **could** be emitted in a direction that directly counter-propagates against the direction of the incident laser pulse. This particular facet of the mechanism is mostly unexplored and could be a promising avenue of future research.

### 4.3.2 Electron Energy Scaling Relations

To be able to characterise the ZVP absorption mechanism and confirm the validity of the theory, it is necessary to consider the impact varying the system's initial conditions

will have on the degree of absorption. The simplest, and most intuitive, model to consider is how the kinetic energy of a single electron acted upon by this mechanism – and subsequently the electron fluid – scales with the initial conditions of the system. It is important to note here that the model presented below does not apply to the bulk body of the electrons in the plasma; it is only applicable to those electrons in the skin layer that are accelerated by the ZVP mechanism and co-propagate with the vector potential "zeroes".

If one considers displacing an electron fluid by a small displacement vector, $\Delta\vec{r}$, then a space charge of ions, $Q$, is left behind:

$$Q = en_{\mathrm{e}}|\Delta\vec{r}|\varsigma \tag{4.28}$$

where $n_{\mathrm{e}}$ is the electron density of the plasma, and $\varsigma$ is the cross-sectional area that describes the space swept out by the electron fluid as it is displaced by $\Delta\vec{r}$.

During the adiabatic stage of the ZVP mechanism, the electrostatic force caused by the setup of the space charge, $Q$, will be precisely compensated by the radiation pressure being exerted on the electrons by the laser pulse:

$$\mathcal{P}_{\mathrm{E}} = \mathcal{P}_{\mathrm{L}} \tag{4.29}$$

where $\mathcal{P}_{\mathrm{E}}$ is the electrostatic pressure arising from the uncompensated space charge, and $\mathcal{P}_{\mathrm{L}}$ is the radiation pressure caused by the incident laser pulse. The radiation pressure can be expressed as:

$$\mathcal{P}_{\mathrm{L}} = \frac{1}{2}\epsilon_0 E_{\mathrm{L}}^2 = \frac{\epsilon_0}{2}\left(\frac{a_0\omega_{\mathrm{L}}m_{\mathrm{e}}c}{e}\right)^2 \tag{4.30}$$

where $E_{\mathrm{L}}$ is the electric field of the laser pulse, and the far right hand side of Equation 4.30 is derived by using the definition of $a_0$ in Equation 2.27.

The pressure arising due to the space charge is given by:

$$\mathcal{P}_{\mathrm{E}} = \frac{|Q\vec{E}_{\mathrm{S}}|}{\varsigma} \tag{4.31}$$

where $\vec{E}_{\mathrm{S}}$ is given by Gauss' law:

$$\iint_{\mathrm{S}} \vec{E}_{\mathrm{S}} \cdot d\vec{\varsigma} = \frac{Q}{\epsilon_0} \tag{4.32}$$

Combining Equations 4.31 and 4.32 yields a form for the electrostatic pressure:

$$\mathcal{P}_{\mathrm{E}} = \frac{Q^2}{\epsilon_0 \varsigma^2} = \frac{(en_{\mathrm{e}}|\Delta\vec{r}|)^2}{\epsilon_0} \tag{4.33}$$

It is worth noting here that the evaluation of Gauss' law is vastly simplified by recognising that the normal vector describing the surface $\vec{\varsigma}$ is simply the displacement vector $\Delta\vec{r}$.

By substituting Equations 2.36, 4.30, and 4.33 into Equation 4.29; an expression for $\Delta\vec{r}$ can be obtained:

$$|\Delta\vec{r}| = \frac{\sqrt{2}}{4\pi}\frac{a_0 n_{\mathrm{c}}}{n_{\mathrm{e}}}\lambda = \frac{\sqrt{2}}{4\pi}\frac{\lambda}{S} \tag{4.34}$$

From Equation 4.34 it is relatively easy to calculate the kinetic energy gain, $T$, of a single electron that crosses the pseudo-capacitor with electric field $\vec{E} = en_{\mathrm{e}}\Delta\vec{r}/\epsilon_0$, and therefore, the total kinetic energy of the electron fluid, $U$:

$$T = e\vec{E} \cdot \Delta\vec{r} = f_{\mathrm{ZVP}}\frac{a_0^2}{n_{\mathrm{e}}\lambda^2} \tag{4.35}$$

$$U = n_{\mathrm{e}}\varsigma|\Delta\vec{r}|T = f'_{\mathrm{ZVP}}\frac{a_0^3}{n_e\lambda^3} \tag{4.36}$$

where $f_{\mathrm{ZVP}}$ and $f'_{\mathrm{ZVP}}$ indicate some absorption efficiency associated with the ZVP

process that has not been accounted for with this simplistic, yet intuitive, model.

### 4.3.3 N-Dimensional Energy Scaling

The scaling relations in Equations 4.35 and 4.36 agree, in form, precisely with the previous one dimensional work done by Baeva *et al.* [57]. To test these with fully three-dimensional simulations, however, would be an exceptionally costly exercise. Therefore, it is desirable to establish that the scaling relation for the electron energy is independent of the number of dimensions used in the model and subsequent simulations. The key modification to make to the model presented above comes from recognising that the permittivity of free space, $\epsilon_0$, has a different form depending on the number of dimensions you consider the system to be in. If one then considers the space to be an N-dimensional cube of length, $L$, then both the radiation and electrostatic pressures and Gauss' law are modified are modified:

$$\mathcal{P}_{\mathrm{L}}^{(N)} = \frac{\epsilon_0^{(N)}}{2}\left(\frac{a_0\omega_{\mathrm{L}}m_{\mathrm{e}}c}{e}\right)^2 \tag{4.37}$$

$$\mathcal{P}_{\mathrm{E}}^{(N)} = \frac{|Q\vec{E}_{\mathrm{S}}|}{L^{N-1}} \tag{4.38}$$

$$\oint_{L^{N-1}} \vec{E}_{\mathrm{S}} \cdot d^{N-1}\vec{L} = \frac{Q}{\epsilon_0^{(N)}} \tag{4.39}$$

The exact equivalence of Equations 4.37, 4.38, and 4.39 with Equations 4.30, 4.31, and 4.32 indicates the scaling relations in Equations 4.35 and 4.36 will be exactly recovered irrespective of the number of dimensions of the system in question. Therefore, computing resources can be saved by conducting a numerical investigation into the ZVP mechanism using only two-dimensional particle-in-cell simulations.

## 4.4 Numerical Validation of the Zero Vector Potential Theory

Any numerical simulations investigating the ZVP mechanism should be able to reproduce the core facets of the theory presented above. These include the existence of zeroes in the vector potential propagating through the plasma, fast electron bunches co-propagating with said zeroes, energy scalings matching the form of Equations 4.35 and 4.36, and a significant contribution from the ZVP mechanism to the intensity of coherent x-rays produced during the laser-plasma interaction.

While Baeva *et al.* successfully saw these results in one-dimensional particle-in-cell simulations [57], at higher dimensions a number of instabilities (for example the hosing instability [139–141]) could take effect and severely disrupt the efficiency – or even the existence – of the absorption mechanism. It is therefore desirable to check that the ZVP mechanism can still be observed in systems more vulnerable to instability.

### 4.4.1 Simulation Setup

The simulations described in the remainder of this chapter were carried out using OSIRIS. OSIRIS is a fully relativistic particle-in-cell code, which when run in two spatial dimensions, retains three-dimensional calculations of the velocity and electromagnetic field spaces [49].

The grid for the simulation was set to be a square of side length $250k_0^{-1}$, where $k_0$ is the wavenumber of the incident laser pulse. In terms of number of cells, the grid was 64 cells per $k_0^{-1}$ in the $\hat{x}$-direction and 32 cells per $k_0^{-1}$ in the $\hat{y}$-direction. This was sufficient to resolve the high momentum features in the electron profiles that are presented later in the thesis. However, resolving the coherently generated x-rays required simulations to be run at a higher resolution of 250 cells per $k_0^{-1}$ in

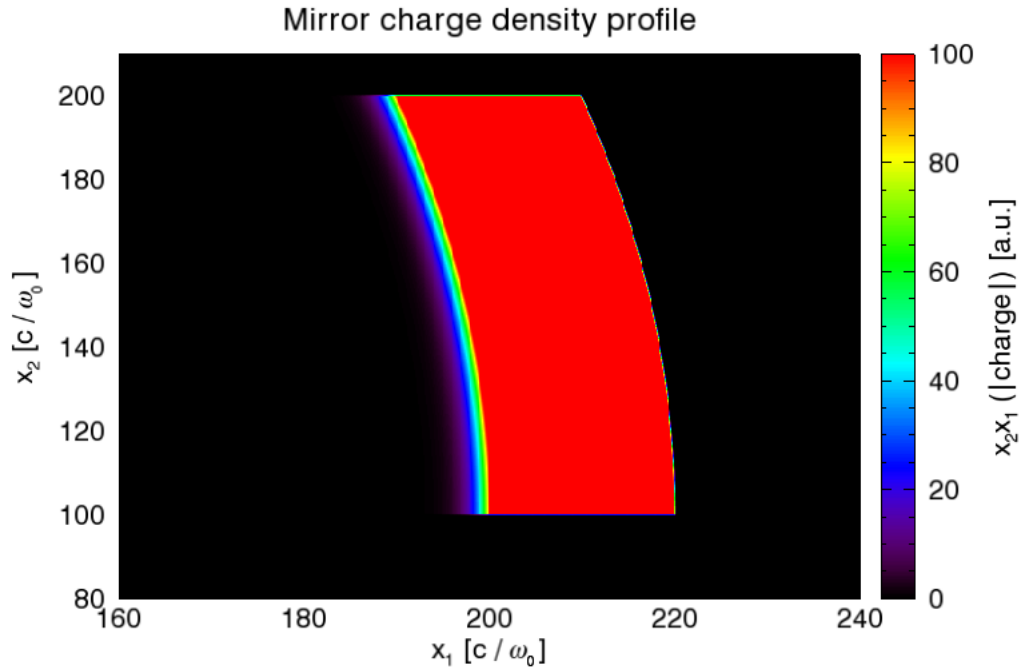



Figure 4.4: Typical initial target profile, in this case with the bulk of the plasma mirror being characterised by $n_e = 100n_c$

each direction. The simulation was run for a total time of $375\omega_0^{-1}$ with a time step of $5 \times 10^{-3}\omega_0^{-1}$.

The plasma targets were simulated using 16 electron macro-particles and 4 ion macro-particles per cell with the mass:charge ratio of the ions being set at 3660 times larger than that of the electrons. In effect, this means that the simulation modelled the interaction of an intense laser pulse with a plasma comprising a single fully ionised element heavier than Hydrogen[3]. The targets were modelled as parabolic plasma mirrors [92, 93] with a radius of curvature of $500k_0^{-1}$. This target shape was chosen as it was found that the x-rays generated from a rectangular target were significantly more divergent making the intensity spectrum of the generated radiation more difficult to extract. The front of the target was characterised with an exponentially decaying profile in the radial direction of the mirror, with a scale length of $1.25k_0^{-1}$. This

[3]The mass number of most elements is approximately double its atomic number

was done to ensure the efficient generation of coherent x-rays from the targets while maintaining a sharp density gradient to allow the potential well to be set up [76,81,82]. The density of the main body of the plasma mirror was varied from $n_e = 25n_c$ to $n_e = 100n_c$. A typical simulation target is depicted in Figure 4.4.

The laser pulse was simulated as a p-polarised Gaussian pulse to ensure that the momenta in the direction of the polarisation could be faithfully extracted. The pulse duration was set to $160\omega_0^{-1}$, where $\omega_0$ is the angular frequency of the pulse. The pulse was focused down to a spot diameter of $12\pi k_0^{-1}$. The normalised vector potential of the pulse was varied from $a_0 = 5$ to $a_0 = 100$ over the course of the simulations and included one run where a circularly polarised pulse was used to investigate the case of a vector potential that never passes through zero.

To give a more intuitive feel for what the values quoted above translate to in reality, Table 4.1 is presented to demonstrate the conversion factors between dimensionless OSIRIS variables and real-life quantities, assuming $\lambda = 1\,\mu$m.

### 4.4.2 High-Momentum Phase-Space Spikes

To qualitatively provide evidence of the existence of the ZVP mechanism, the laser pulse was set incident on the plasma in the $\hat{x}$-direction and the phase-space plots displaying the electron charge density distribution on a $p_x{-}x$ phase diagram were extracted from the results.

Figure 4.5 shows just such a phase diagram with the two insets displaying the vector potential, $A$, overlaid on the phase space in frames separated by $1/5^{\text{th}}$ of a wave cycle in time. In each case, the vector potential has been calculated by taking the current density outputs, $\vec{J}$, of the simulation and integrating them as in Equation 4.6 to yield $\vec{A}$. It can clearly be seen from inset (a) of Figure 4.5 that the emergence point of the high momentum spikes coincides with the position at which the vector potential passes through zero. In inset (b) – corresponding to a later time – it is

| Parameter | Dimensionless Value | S.I. value ($\lambda = 1\,\mu$m) |
|---|---|---|
| Grid size | $250k_0^{-1} \times 250k_0^{-1}$ | $40\,\mu$m$\times 40\,\mu$m |
| $\hat{x}$-resolution | 64 cells per $k_0^{-1}$ | 2.5 nm |
| $\hat{y}$-resolution | 32 cells per $k_0^{-1}$ | 5 nm |
| Simulation Duration | $375\omega_0^{-1}$ | 200 fs |
| Time Step | $5 \times 10^{-3}\omega_0^{-1}$ | 2.5 as |
| Radius of curvature | $500k_0^{-1}$ | $80\,\mu$m |
| Target scale-length | $1.25k_0^{-1}$ | $0.2\,\mu$m |
| Electron density | $25n_c$ | $2.8 \times 10^{22}\,\mathrm{cm}^{-3}$ |
| | $40n_c$ | $4.5 \times 10^{22}\,\mathrm{cm}^{-3}$ |
| | $50n_c$ | $5.6 \times 10^{22}\,\mathrm{cm}^{-3}$ |
| | $60n_c$ | $6.7 \times 10^{22}\,\mathrm{cm}^{-3}$ |
| | $75n_c$ | $8.4 \times 10^{22}\,\mathrm{cm}^{-3}$ |
| | $100n_c$ | $1.1 \times 10^{23}\,\mathrm{cm}^{-3}$ |
| Pulse duration | $160\omega_0^{-1}$ | 85 fs |
| Focussed spot diameter | $12\pi k_0^{-1}$ | $6\,\mu$m |
| Intensity ($a_0$) | 5 | $3.4 \times 10^{19}\,\mathrm{W\,cm}^{-2}$ |
| | 10 | $1.4 \times 10^{20}\,\mathrm{W\,cm}^{-2}$ |
| | 15 | $3.1 \times 10^{20}\,\mathrm{W\,cm}^{-2}$ |
| | 30 | $1.2 \times 10^{21}\,\mathrm{W\,cm}^{-2}$ |
| | 50 | $3.4 \times 10^{21}\,\mathrm{W\,cm}^{-2}$ |
| | 100 | $1.4 \times 10^{22}\,\mathrm{W\,cm}^{-2}$ |

Table 4.1: Conversion factors between the dimensionless variables used as inputs in OSIRIS and variables with units in the Système Internationale, assuming the laser wavelength is equal to $1\,\mu$m.

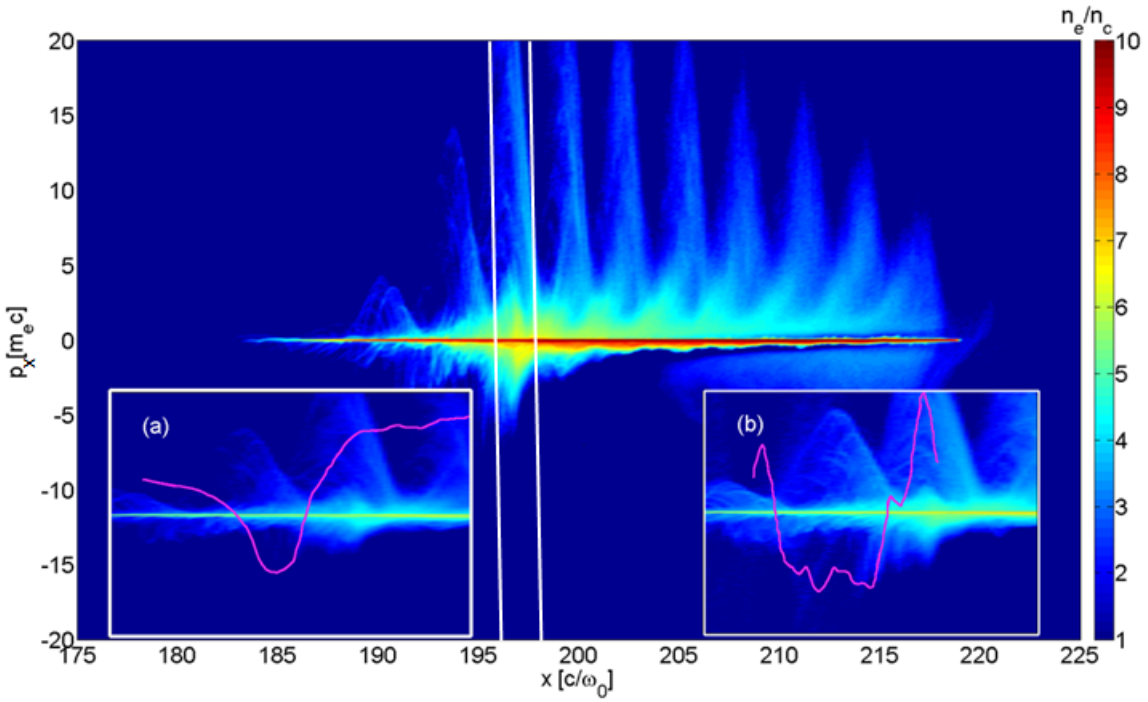
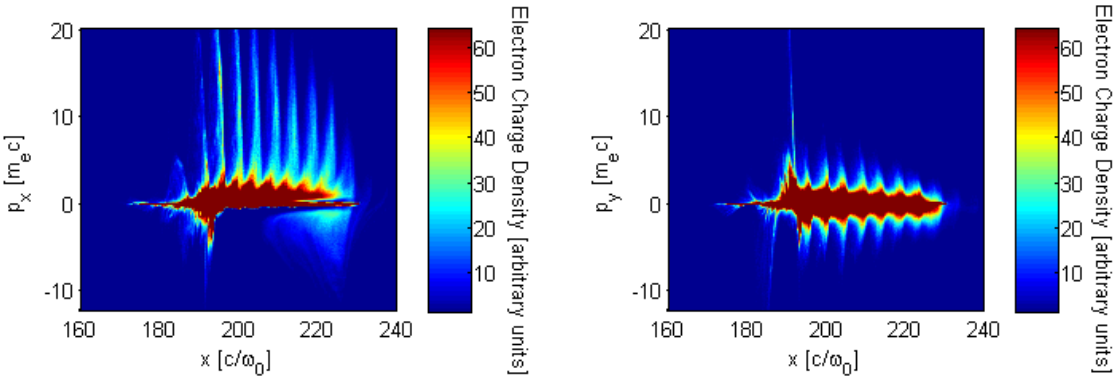



Figure 4.5: A $p_x$–$x$ phase space plot for the case of $a_0 = 30$, $n_e = 50n_c$ with the transverse vector potential (pink lines) of the system overlaid in insets (a) and (b) showing the co-timing of the onset of the high-momenta co-propagating electron bunches with zeroes in the vector potential. Inset (a) is a zoom of the main figure. Inset (b) is a zoom of the same section of the pulse $1/5^{\text{th}}$ of a wave cycle later in time. The overlaid white lines indicate the longitudinal extent of a typical bunch of electrons.




(a) $p_x - x$ (b) $p_y - x$

Figure 4.6: Momentum-position phase space plots investigating ZVP absorption of an obliquely incident laser pulse with $a_0 = 30$, $n_e = 50 n_c$. The high momentum bunches are seen to be propagating in the direction of the incident laser pulse and with no discernible high momentum electrons transverse to the beam.

evident that the momentum spikes have moved along with the pulse. This provides the first evidence, albeit qualitative, that the ZVP mechanism is at work in this regime.

At this stage, having observed indications that the ZVP mechanism is active, the three qualitative criteria of: 1. bunches propagating in the laser-forward direction, 2. bunches only existing if the laser is linearly polarised, and 3. high harmonic generation becoming prevalent should be checked.

The first criterion is most easily checked by re-orienting the target so that the pulse is incident on the target at an oblique incidence and taking the phase-space plots in momentum-directions parallel and orthogonal to the direction of laser propagation. To investigate the extent to which oblique incidence affects the launching of the fast electrons into the plasma, the target was rotated such that there was an angle of 30° between the normal of the plasma's ablating surface and the laser pulse propagating in the $\hat{x}$-direction at the point of impact. $p_x - x$ and $p_y - x$ phase spaces were then extracted, as can be seen in Figure 4.6. It is clear from Figure 4.6a, that despite the reorientation of the target, the high momentum bunches are still co-propagating with the incident pulse along the $\hat{x}$-direction, with no identifiable high momentum

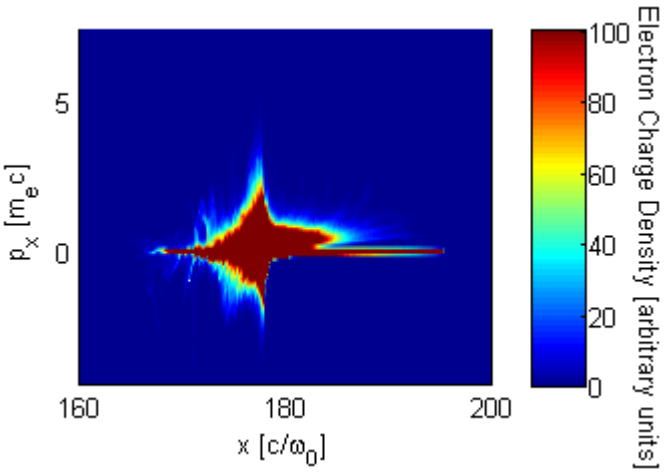
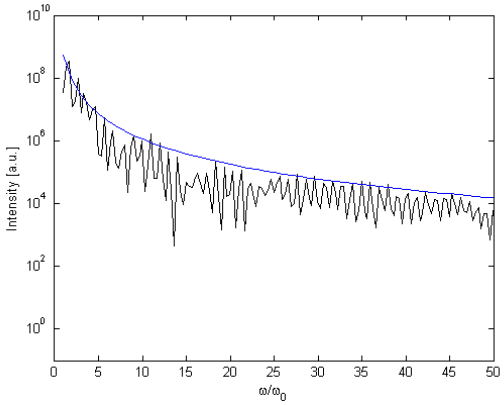


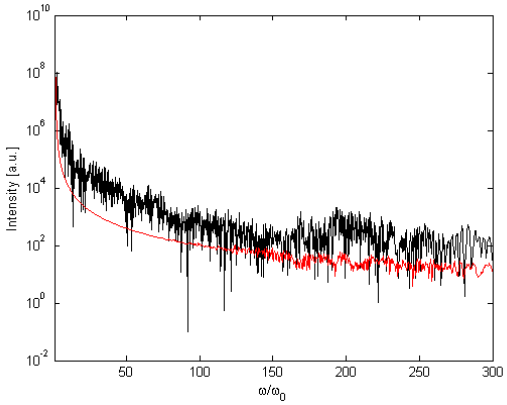

Figure 4.7: $p_x - x$ phase space plot for the case of a circularly polarised pulse with $a_0 = 30$, $n_e = 50 n_c$. Clearly, there are no high longitudinal-momenta spikes.

features in the direction transverse to the beam (as depicted in Figure 4.6b). One interesting feature of the simulation results depicted in Figures 4.6a and 4.6b is that there appears to be a symmetric oscillation in the direction perpendicular to the laser propagation. This, could, therefore manifest itself in reality as the electron bunches carving out helical trajectories into the plasma. This certainly merits further investigation with 3D simulations and experimental investigation. This, therefore, validates the prediction of the ZVP theory that the electron bunches are launched into the plasma longitudinally with respect to the incident laser pulse, and independent of any angle of incidence onto the target.

The second qualitative criterion of the ZVP mechanism, that it should only be observed with laser pulses that are linearly polarised was tested by conducting simulations with laser pulses set to be circularly polarised. Phase space plots equivalent to Figure 4.5 were extracted, an example of which is shown in Figure 4.7. Not only is the maximum momentum observed in the circular polarisation simulations significantly lower than in the linearly polarised case, but it is also immediately obvious that – as expected – the lack of zeroes in the vector potential has removed the high momentum bunches that penetrate the plasma in the linearly polarised scenario.




(a) Extracted spectrum of the coherent x-rays (black) and a $q^{-8/3}$ power law curve (blue)




(b) Comparison of the extracted spectrum for the linearly (black) and circularly (red) polarised cases.

Figure 4.8: Intensity spectra of the coherent x-rays reflected from the simulation target for the case $a_0 = 30$, $n_e = 50n_c$. 4.8a clearly shows that in the linearly polarised case, the spectrum matches well with the power law described in Equation 2.82. 4.8b clearly shows that there are orders of magnitude difference between the reflected x-ray spectra in the cases of the incident laser pulse being linearly vs. circularly polarised. It is worth noting that the circularly polarised light incident at 45° is not well represented in 2D particle in cell simulations, instead appearing as a combination of s- and p-polarised light, and so while it describes the situation sufficiently well to prevent the vector potential going through zero and so illustrate the necessary point here; the full physics, particularly with respect to conventional high harmonic generation, is not captured.

The third qualitative criterion of the ZVP mechanism, that of coherent x-ray generation – i.e. high-order harmonic generation, was also tested. The Fourier transform of the radiation reflected from the target was taken, and the spectrum plotted. Examples of these plots can be seen in Figure 4.8. The form of the spectrum in Figure 4.8a is seen to match well with the $q^{-8/3}$ spectrum predicted by Equation 2.82. Further, it is seen that when the same simulation is run with a circularly polarised pulse, the harmonic spectrum is orders of magnitude less intense, as depicted in Figure 4.8b. The correlation between reflected x-ray intensity and the presence of the ZVP mechanism strongly implies that ZVP acceleration is a significant contributor to high harmonic generation, as expected from the criterion above.

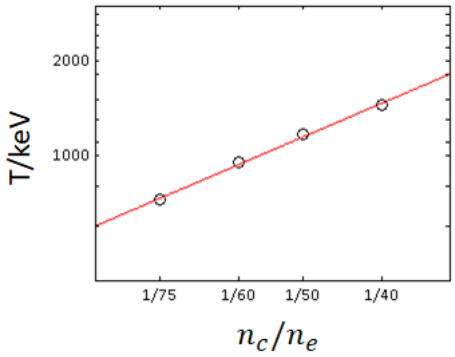



Figure 4.9: Log-log plot of the $1/n_e$ dependence of the fast electron energy. Plotted points indicate energies extracted from 2D PIC simulations for the case $a_0 = 30$ for a range of densities. The fitted red line yields a gradient of $1.11 \pm 0.04$.

### 4.4.3 Energy Scaling Relations

Having validated all three of the qualitative criteria associated with the ZVP mechanism, it seems plausible that the ZVP mechanism is in effect in the regime being investigated here. To substantiate this claim, the fast electron energy scalings of Equation 4.35 need to be validated through the simulations presented above. This was done by conducting two sets of simulations. In each set, the first high-momentum peak was identified. The energy of the 5% most energetic electrons was then extracted. The average energy of this fast 5% was calculated and plotted. This was done to ensure that when calculating the maximum energy of the fast electrons, a false result wasn't recorded by just taking the single most energetic macro-particle and leaving any measurement subject to vulnerability against rogue numerical error in the simulations. In one set of simulations, the plasma density was varied for a constant value of $a_0 = 30$; whilst in the second set, the laser intensity was varied for a constant value of $n_e = 50 n_c$.

Figure 4.9 shows that the inverse linear dependence of the fast electron kinetic energy with electron density is in a very good agreement with Equation 4.35. The

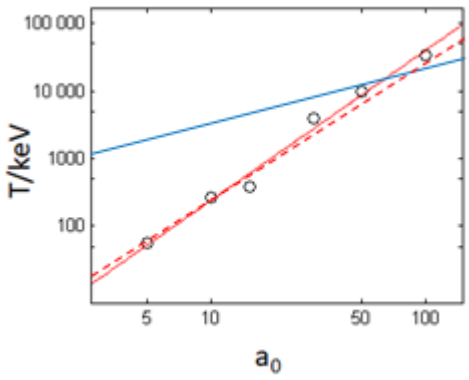



Figure 4.10: Log-log plot of the $a_0^2$ dependence of the fast electron energy. Plotted points indicate energies extracted from 2D PIC simulations for the case $n_e = 50n_c$ for a range of normalised vector potentials. The fitted red line yields a gradient of $2.15 \pm 0.17$. The solid blue line indicates the ponderomotive scaling of Equation 2.77, and the dashed red line indicates the predicted $a_0^2$ scaling.

simulations extract a dependence of energy on the density of:

$$T \propto n_e^{-1.11 \pm 0.04} \tag{4.40}$$

This matches closely with the predicted dependence of $1/n_e$.

Similarly, Figure 4.10 shows a dependence of the electron kinetic energy on the vector potential amplitude. In these simulations, the agreement with the quadratic prediction of Equation 4.35 was excellent with the result being:

$$T \propto a_0^{2.15 \pm 0.17} \tag{4.41}$$

The excellent agreement of Equations 4.40 and 4.41 with Equation 4.35, combined with the previous validation of the qualitative predictions of the ZVP theory naturally lead to the conclusion that in the limit $a_0 \gg 1$ and $S > 1$, a post-ponderomotive regime is entered and the ZVP absorption mechanism takes hold of the dynamics of the system. The potential ramifications of this are particularly interesting, laser-energy absorption could become more efficient as the fast electron energy scales lin-

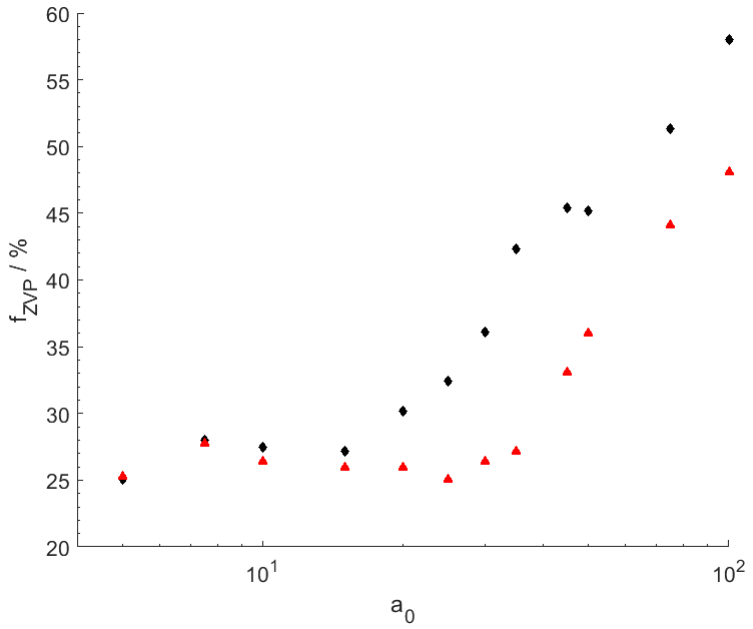



Figure 4.11: A plot of the percentage of incident laser radiation absorbed vs. laser intensity (in terms of $a_0$) for a plasma with electron density $n_e = 50n_c$ (black diamonds), and $n_e = 100n_c$ (red triangles).

early with intensity, in direct contrast to the ponderomotive regime where fast electron energy scales as $I^{1/2}$. It is also interesting that while the ponderomotive energy is higher than the ZVP energy for a wide range of $a_0$, beyond $a_0 \approx 60$, the ZVP mechanism is expected to dominate. Further, the prospect of an augmented intensity in coherently generated x-rays suggests the possibility of a coherent x-ray source with a well-defined spectrum that could be exploited in the laboratory. The potential application of these x-rays in future HEDP experiments is explored and discussed in Chapter 5.

## 4.5 Efficiency of the Zero Vector Potential Mechanism

As with all absorption mechanisms, it is not merely the dynamics of the ZVP process that are of interest, but also the efficiency of the process and the extent to which the incident laser energy is partitioned amongst the reflected light (both at the fundamental frequency and in high-order harmonics), the plasma electrons, and plasma ions. Although, there are currently no theoretical models predicting the efficiency of the ZVP mechanism, it is possible to proceed with an investigation numerically using particle-in-cell simulations.

The efficiency of the mechanism, $f_{\mathrm{ZVP}}$, is defined as:

$$f_{\mathrm{ZVP}} = \frac{U_{\mathrm{abs}}}{U_{\mathrm{L}}} = 1 - \frac{U_{\mathrm{refl}}}{U_{\mathrm{L}}} \tag{4.42}$$

where $U_{\mathrm{abs}}$ is the amount of energy absorbed by the plasma, $U_{\mathrm{L}}$ is the energy of the incident laser pulse, and $U_{\mathrm{refl}}$ is the energy of reflected laser light, whether at the fundamental frequency or as a coherent harmonic. By integrating the reflected radiation's energy spectra, such as that shown in Figure 4.8a, it is possible to implicitly extract the absorption efficiency for each simulation in which the reflected spectrum was obtained.

The absorption efficiency, $f_{\mathrm{ZVP}}$, was calculated in this way for a range of values for $a_0$, using two densities as examples: $n_{\mathrm{e}} = 50n_{\mathrm{c}}$ and $n_{\mathrm{e}} = 100n_{\mathrm{c}}$. A plot of the efficiency is shown in Figure 4.11. It is clear that a wide range of absorption efficiencies can be obtained, although it is not immediately clear what the cause of increased absorption efficiency is at higher intensities. In order to understand the difference in absorption efficiencies between plasma of different densities, the data plotted in Figure 4.11 has been re-plotted in Figure 4.12, this time with the absorption efficiency plotted against

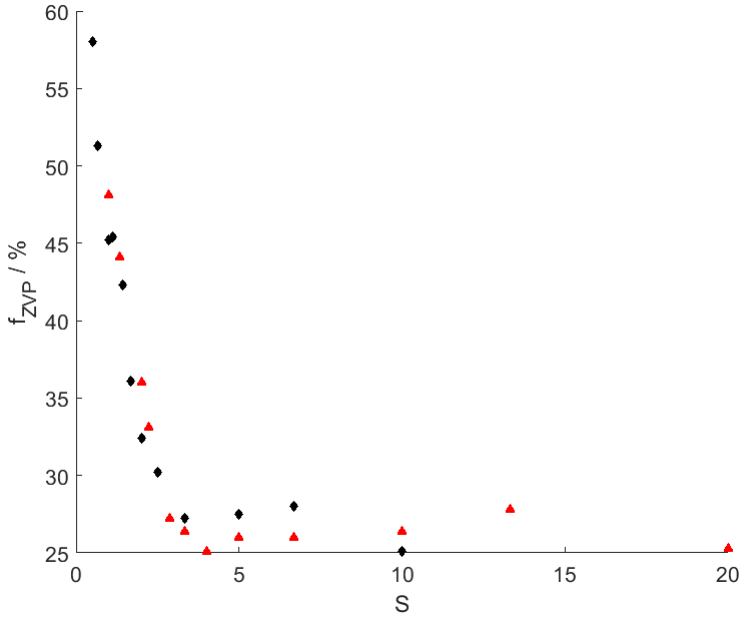



Figure 4.12: A plot of the percentage of incident laser radiation absorbed vs. the relativistic similarity parameter (as defined in Equation 4.7) for a plasma with electron density $n_e = 50n_c$ (black diamonds), and $n_e = 100n_c$ (red triangles).

the relativistic similarity parameter as given in Equation 4.7.

From Figure 4.12, it is clear that the absorption efficiency plummets from small values of $S$, until approximately $S = 4$. From $S = 4$ onward, there appears to be a roughly constant efficiency of approximately 26-28%. In fact, for both densities presented here the absorption efficiency follows a trend:

$$f_{\mathrm{ZVP}} \propto S^{-1.000(3)} \tag{4.43}$$

with the exponent being equal to 1, accurate to 4 significant figures.

The author's interpretation of this data is as follows: for high values of $S$, corresponding to low values of $a_0$, the incident laser pulse is very efficiently converted into coherent high-order harmonics. As the intensity of the laser pulse is increased, and the value of the relativistic similarity parameter falls, the incident pulse becomes more effective at hole boring [54, 138], and the plasma surface is significantly deformed, as

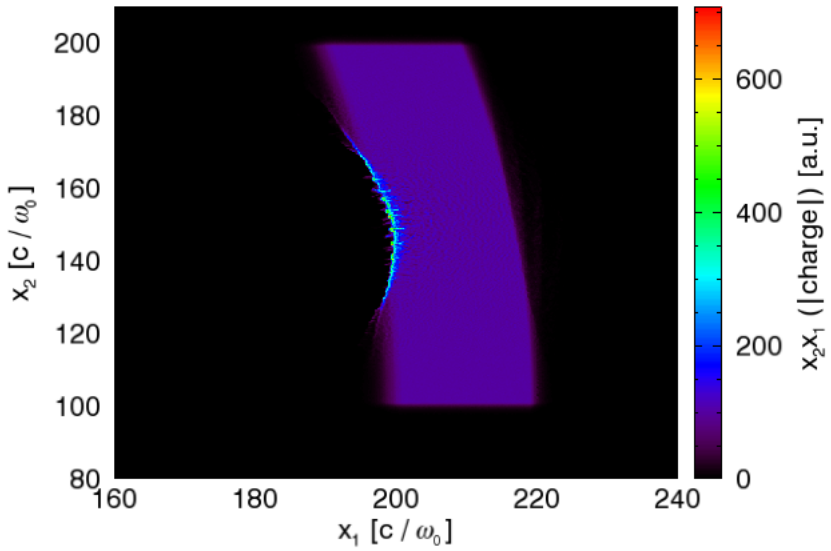



Figure 4.13: Target profile for the case of a bulk plasma with electron density $n_e = 100n_c$ having been subject to an incident laser of $a_0 = 50$. The plasma surface has clearly been deformed by the hole boring effect of the laser.

can be seen in Figure 4.13. This deformation inhibits the conversion efficiency of the incident pulse into XUV reflected radiation and so more energy is available to be absorbed by the plasma. Thus it is considered here that the relativistic similarity parameter $S$ is a linear indicator of the efficiency of high-harmonic generation.

By extracting phase-space plots of the electron and ion energies, it is also possible to determine how the incident laser energy is partitioned amongst the constituent species of the plasma. A plot representing this information is displayed in Figure 4.14. It is clear, and unsurprising given the short timescales of the mechanism, that the electrons gain the vast majority of the absorbed laser energy. However, it is interesting to note that as the laser intensity is increased, the percentage of absorbed energy that is gained by the ions increases from 8% to 30% over the course of the intensity scan. The nature of this trend is attributed to the fact that as the laser intensity is increased, the plasma ions are more susceptible to direct acceleration by the laser pulse, despite the fact that their inertia is significantly larger than that of the plasma electrons. Calculating the percentage of absorbed energy that could be

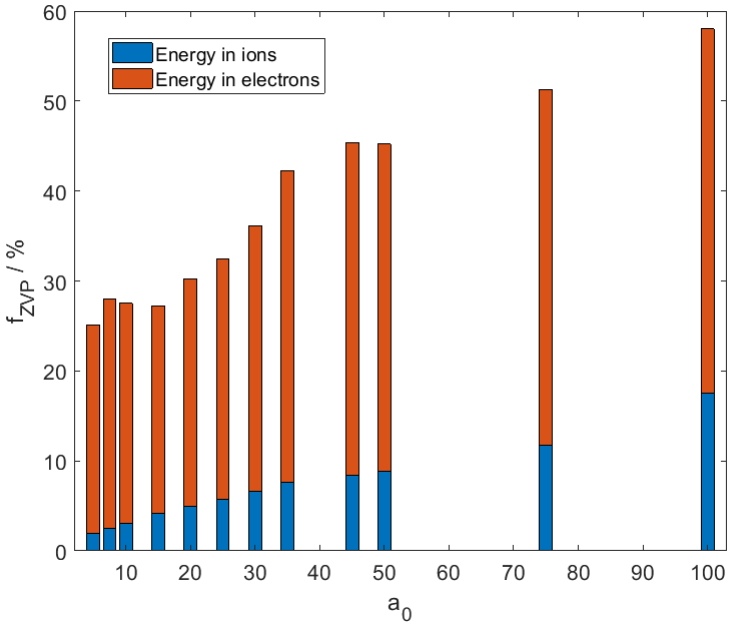



Figure 4.14: A plot of the ZVP absorption efficiency against incident laser intensity (in terms of $a_0$) for a plasma with an electron density of $n_e = 50n_c$, with the partitioning of the energy between ions (blue) and electrons (red) explicitly displayed as shaded fractions of each bar.

found in the electron and ion populations was done by considering how much energy was absorbed (as depicted in Figure 4.12) and comparing this to the amount of energy that was gained by the electron and ion populations respectively. Numerical heating was accounted for by running simulations with the same parameters but with no laser pulse and measuring how the energy of the electrons and ions increased over time. The numerical heating effect was made negligible by using the high resolutions discussed above.

## 4.6 Proposed Measurement of Zero Vector Potential Absorption

It is a well-known and well-used adage of experimental science that nothing is true until it has been measured. Therefore, in a similar vein to the previous chapter,

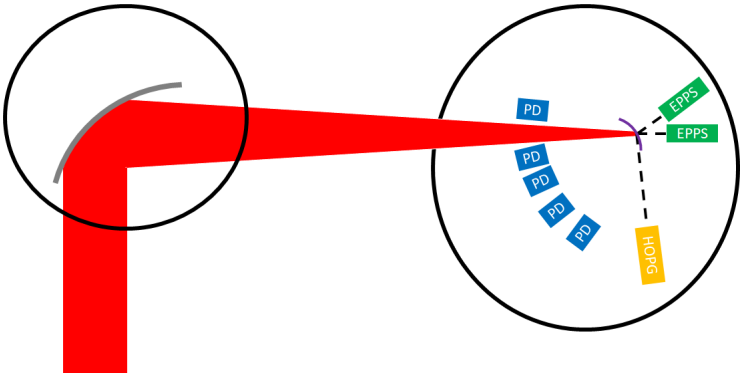



Figure 4.15: A schematic for the potential experiment that could be conducted using the HERCULES laser to investigate the existence of the ZVP mechanism. The incident laser pulse (red) is reflected from a large plasma mirror to boost the contrast of the pulse to facilitate a short scale-length pre-plasma. The pulse is incident on a target (purple). A HOPG spectrometer (yellow) diagnoses the electron temperature. EPPS's (green) set up in the laser-forward and laser-forward+45° directions measure the energy spectrum of electrons ejected from the rear of the target. A large array of photo-diodes (blue) measure the spectrum of light reflected from the front surface of the plasma to obtain measurements of coherent x-ray generation.

this chapter will be concluded with an outline of a possible experiment that could be used to determine the existence of the ZVP absorption mechanism. Again, like the experiment design described in Chapter 3, this design suggests the use of foam targets to explore the full range of plasma densities that should be considered when investigating the ZVP mechanism.

### 4.6.1 Target Parameters

Assuming the use of a $1\,\mu$m laser system, investigating the ZVP mechanism experimentally will require using plasma with densities ranging from $10n_c$ to $100n_c$, which corresponds to a density range of: $10^{22}\,\mathrm{cm}^{-3} < n_e < 10^{23}\,\mathrm{cm}^{-3}$. For a plastic (CH) foam, this therefore corresponds to a mass density range of: $220\,\mathrm{mg\,cm}^{-3} < \rho < 2.2\,\mathrm{g\,cm}^{-3}$. To obtain a full density range will therefore require using a variety of materials to create the targets ranging from plastic foils at the high-density end, to templated foams at the low-density end of the scale [29].

### 4.6.2 Laser Parameters

The laser system proposed for this potential experiment is the HERCULES 300 TW laser in the Gérard Mourou Center for Ultrafast Optical Science at the University of Michigan [60]. To date, HERCULES holds the world record for the highest focused intensity of any laser system, reaching intensities of up to $2 \times 10^{22}\,\mathrm{W\,cm^{-2}}$ with pulse durations of 30 fs [142]. As a Neodymium:Glass laser system, the laser wavelength is approximately $1\,\mu$m, and so the values of $a_0$ attainable with HERCULES range from less than 1 to 120. This makes HERCULES an ideal laser system for an experimental campaign investigating the ZVP mechanism.

### 4.6.3 Diagnostics

The list of diagnostics proposed to measure the existence of the ZVP mechanism is quite short:

- Photo-diodes sensitive to XUV radiation to measure the spatial distribution of any coherently generated harmonics.
- A Highly Oriented Pyrolytic Graphite (HOPG) Crystal spectrometer to measure the X-ray emission from the plasma to measure temperature [134].
- Electron-Positron-Proton Spectrometers (EPPS) to measure the fast electron spectrum [143].

### 4.6.4 Target Chamber & Campaign Design

A schematic of a potential target chamber set-up, using HERCULES' double chamber configuration is presented in Figure 4.15. A plasma mirror should be used to boost the contrast of HERCULES' main pulse [92, 93]. This will ensure that the scale-length of any pre-plasma ablation front is kept sufficiently short to match the conditions

in the simulations and optimise high harmonic generation [82]. It is suggested that the EPPS's are oriented in the laser-forward and laser-forward+45° directions so that more than one electron spectrum can be obtained. It is expected that the EPPS in the laser-forward direction will measure high-energy peaks in the electron energy spectrum, with a narrow transverse width on account of the relatively low transverse momentum of the accelerated electrons, that would not be seen in the data collected by the other EPPS. This measurement would test the hypothesis that fast electrons are generated in the laser-forward direction. Additional data from the HOPG spectrometer could offer further information about the plasma temperature and density from x-ray emission spectra.

Rotating targets between shots to obtain different angles of incidence would test the hypothesis that the mechanism is independent of incidence angle. Similarly alternating between s- and p-polarisation in the laser would test the hypothesis that ZVP absorption is independent of polarisation direction.

The array of photo-diodes should be used to measure the intensity and spectrum of reflected light, as well as its angular distribution, to verify that the reflected radiation possesses a spectral form matching Equation 2.82.

For quantitative verification of the ZVP mechanism, the laser intensity should be varied, as should the plasma density to obtain measurements from which experimental analogues of Figures 4.9 and 4.10 could be obtained for comparison with the results of the OSIRIS simulations.

With the measurements described above, a potential high-power laser experiment could verify the existence of the ZVP mechanism and make meaningful measurements of the absorption efficiency, $f_{\mathrm{ZVP}}$.

## 4.7 Summary

In this chapter, the concept of a post-ponderomotive regime for laser-energy absorption was introduced and discussed. It was noted that in the limit that the relativistic similarity parameter exceeds unity, the plasma electrons can respond adiabatically to the ponderomotive force of the incident laser pulse and thus the electrons are confined within a potential well set up by the laser radiation pressure on one side, and electrostatic pressure from electron-ion fluid displacement on the other. The prospect of the Zero Vector Potential absorption mechanism was introduced by demonstrating the possibility of zeroes in the vector potential propagating through dense plasma[4]. The consequence of these zeroes was shown to be a severe disruption of the aforementioned potential well. This results in a destruction of the electrons' adiabaticity and leads to energy absorption taking place over the timescale of several attoseconds.

A number of qualitative predictions regarding the ZVP mechanism were presented: the mechanism is expected to be independent of angle of incidence, only occur if the laser pulse is linearly polarised, and could contribute significantly to coherent x-ray generation. Further, quantitative predictions of how the fast electron energy could be expected to scale with both laser intensity and plasma density were made. These predictions relied on a simple, yet intuitive model outlining the expected dynamics of an electron crossing a pseudo-capacitor system and demonstrated that a significant deviation from the ponderomotive scaling is expected.

Next, the results of an extensive numerical campaign were presented and analysed. Particle-in-cell simulations using the OSIRIS code numerically validated the qualitative predictions mentioned above. More impressively, the quantitative results of the simulations were in excellent agreement with the predicted scaling relations, indicating that entry into the post-ponderomotive regime truly was being observed.

This chapter concluded with a brief exposition of the absorption efficiencies that

[4]Given that the vector potential has been defined in the Lorenz gauge.

were indicated by the OSIRIS simulation results and the presentation of an experimental campaign design for the HERCULES laser facility that could be used to verify the existence of the ZVP mechanism. The experiment could also be used to test the mechanism's hypotheses, both qualitative and quantitative.

Overall, this chapter has presented the ZVP mechanism in a reasonably complete manner but leaves open the question of how this, and other, absorption mechanisms could be impacted by increasing the laser intensity to reach even more extreme regimes.

# Chapter 5

# Applications and Extremes of the Zero Vector Potential Mechanism

The previous chapter introduced the post-ponderomotive regime, and discussed in some detail one particular absorption mechanism - ZVP - that could potentially dominate laser-energy absorption in this novel regime. Having established the parameters through which the post-ponderomotive regime is entered, it is a natural extension of the work presented in Chapter 4 to examine how and when the post-ponderomotive regime ends. Another area of the ZVP mechanism that did not receive a large amount of attention in the previous chapter is the nature and potential applicability of the coherently generated XUV radiation via high harmonic generation from the ZVP absorption mechanism. It is these two topics that form the subject of this chapter. Firstly, the Quantum Electrodynamic (QED) regime will be introduced, with a small number of first-order QED processes that one could expect to occur upon breaking out of the post-ponderomotive regime into the QED regime. A physical model, published in *Scientific Reports* [59], that modifies the ZVP mechanism will be presented, as well as the particle-in-cell simulations used to numerically validate the model. The chapter will then detour slightly to discuss the results of a campaign of hydrodynamic sim-

ulations conducted to model the heating effect of the coherent XUV radiation when incident on a tamped aluminium target. Finally, as in previous chapters, a brief experimental plan will be presented; this one for ELI Beamlines [40] some time into its commissioning period when it has reached peak performance. Given the high-risk nature of an experiment that explores a completely unknown regime, the experiment design will also include a contingency plan to measure how the high harmonics can be used to heat solid density material.

## 5.1 Relativistic Generalisation of the Zero Vector Potential Mechanism

Before considering the impact of QED effects on post-ponderomotive absorption mechanisms, it is important to verify that the mechanism will still hold under extremely relativistic conditions. To do this, it is easiest to consider a simplified form of the incident vector potential in the rest frame of the expanding plasma. Given that beyond the critical density surface, the laser's vector potential will take the form of a spatially evanescent wave, with only temporal oscillations surviving, a simplified form of the laser's vector potential can be assumed:

$$\vec{A}'_{\mathrm{L}} = A'_0 \cos(\omega' t') \exp(-r'/\delta')\hat{r}'_{\mathrm{pol}} \tag{5.1}$$

where $A_0$ is the amplitude and $\omega$ the frequency of the laser pulse, $t$ is the time of propagation, r' is the distance of propagation into the plasma beyond the critical density surface, $\hat{r}'_{\mathrm{pol}}$ is the unit vector in the direction of polarisation of the laser pulse, and primed variables indicate that the quantity is defined and measured in the rest frame. Correspondingly, non-primed variables are defined and measured in the laboratory frame.

By constraining the problem to a p-polarised pulse propagating in the $x-y$ plane, with $\hat{x}$ being the axis of plasma ablation, the unit vector $\hat{r}'_{\text{pol}}$ can be defined as:

$$\hat{r}_{\text{pol}} = \sin\theta\hat{x} - \cos\theta\hat{y} \tag{5.2}$$

where $\theta$ is the angle of incidence of the laser pulse onto the expanding plasma. Now, by taking the Lorentz transform of the electromagnetic 4-potential:

$$\mathbf{A}_\mu = (\phi/c, \vec{A}) \tag{5.3}$$

$$\mathbf{A}'^\mu = \Lambda^\mu_\nu \mathbf{A}^\nu \tag{5.4}$$

where the Lorentz transform is defined as:

$$\Lambda^\mu_\nu = \begin{pmatrix} \gamma & -\beta\gamma & 0 \\ -\beta\gamma & \gamma & 0 \\ 0 & 0 & 1 \end{pmatrix} \tag{5.5}$$

By considering only the $y$-components of Equation 5.4, it becomes immediately clear that:

$$A'\cos\theta' = A\cos\theta \tag{5.6}$$

and by making use of the headlight effect[1] [125]:

$$\cos\theta' = \frac{\cos\theta - \beta}{1 - \beta\cos\theta} \tag{5.7}$$

a form for the vector potential in the laboratory frame can be derived:

[1] A derivation for the headlight effect is provided in the Appendix.

$$A = \frac{1 - \beta \sec\theta}{1 - \beta \cos\theta} A'_0 \cos(\omega' t') \exp(-r'/\delta') \tag{5.8}$$

By next exploiting the relativistic transformation of space-time coordinates:

$$\begin{aligned} ct' &= \gamma ct - \beta\gamma x \\ x' &= \gamma x - \beta\gamma ct \end{aligned} \tag{5.9}$$

this yields:

$$A = A_0 \cos(\omega t - kx) \exp\left(-\frac{[(x - \beta ct)^2 + (y/\gamma)^2]^{1/2}}{\delta}\right) \tag{5.10}$$

where:

$$\begin{aligned} A_0 &= \frac{1 - \beta \sec\theta}{1 - \beta \cos\theta} A'_0 \\ \omega &= \gamma\omega' \\ k &= \frac{\beta\gamma\omega'}{c} \\ \delta &= \frac{\delta'}{\gamma} \end{aligned} \tag{5.11}$$

It is clear from Equation 5.10 that zeroes in the vector potential can continue to propagate into the over-dense plasma for relativistic ablation velocities, just as they do in the more classical case described by Equations 4.21 and 4.22. With this principle established, it is now possible to consider how QED processes will impact the electron energy scaling of Equation 4.41.

## 5.2 Entering a Quantum Electrodynamic Regime

Historically, there has been significant work exploring electron-positron cascade production [144–147] and laser energy absorption [148–151] far into the QED regime - that is, the regime in which quantum electrodynamic processes play a crucial and

dominant role in the evolution of a system. However, a critical area of interest which has received less attention in the literature, is the nature of how breaching the cusp of the QED regime alters the physics of laser-plasma interactions [59]. However, before considering how the laser-energy absorption itself could change at this regime boundary, it is necessary to consider some of the basic processes that become prevalent at QED-relevant conditions.

### 5.2.1 Radiation Reaction

Radiation reaction is a somewhat natural consequence of combining the ideas of radiation pressure and radiation from an accelerating charge. Originally dubbed a "self force", radiation reaction is the recoil, or jerk, that a charged particle is subjected to by the radiation that the particle itself emits. The form for this force can be derived by considering the Larmor formula from Equation 2.78 [152, 153]:

$$\int \vec{F}_{\text{r.r.}} \cdot \vec{v} dt = -\int \frac{dW}{dt} dt = -\int \frac{\mu_0 Q^2}{6\pi c} \dot{v}^2 dt \tag{5.12}$$

where $\vec{F}_{\text{r.r.}}$ is the radiation reaction force.

If Equation 5.12 is integrated by parts, and periodic boundary conditions are assumed[2], then it is relatively simple to retrieve a form for the so-called Abraham-Lorentz, or radiation reaction, force:

$$\vec{F}_{\text{r.r.}} = \frac{\mu_0 Q^2}{6\pi c} \frac{d^3 \vec{r}}{dt^3} \tag{5.13}$$

Dirac subsequently provided a relativistic generalisation for this - the Abraham-Lorentz-Dirac force [155]:

[2]Periodic boundary conditions are not strictly speaking necessary, but they avoid being forced to use an Effective Field Theory. Both approaches yield the same result, so the simplification here is made for illustrative purposes [154].

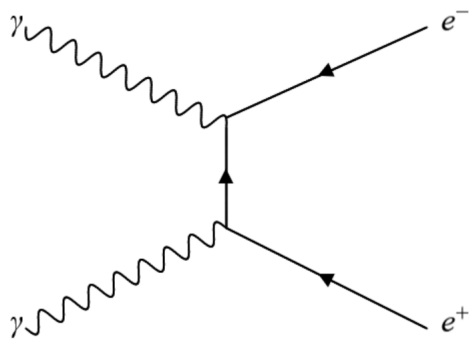



Figure 5.1: A Feynman diagram of the Breit-Wheeler process.

$$\mathbf{F}_{\mu} = \frac{\mu_0 Q^2}{6\pi mc}\left[\frac{d^2\mathbf{P}_{\mu}}{d\tau_{\mathrm{p}}^2} - \frac{\mathbf{P}_{\mu}}{m^2c^2}\left(\frac{d\mathbf{P}_{\nu}}{d\tau_{\mathrm{p}}}\frac{d\mathbf{P}^{\nu}}{d\tau_{\mathrm{p}}}\right)\right] \tag{5.14}$$

where $\mathbf{P}_{\mu}$ is the momentum 4-vector, and $\tau_{\mathrm{p}}$ is the proper time. An interval of proper time, $\Delta\tau_{\mathrm{p}}$, can be expressed as[3]:

$$\Delta\tau_{\mathrm{p}} = \int \frac{dt}{\gamma(t)} \tag{5.15}$$

where $\gamma$ is the Lorentz gamma-factor.

The crucial result of both Equations 5.13 and 5.14 is that the Abraham-Lorentz force is directly proportional to the "jerk" of the charge: the time derivative of the particle's acceleration.

### 5.2.2 Pair Production – the Breit-Wheeler Process

According to QED theory, two high-energy photons can interact to produce a fermion-antifermion pair [156]. The lowest energy version of this yields an electron-positron pair via the Breit-Wheeler process, in which a virtual electron mediates the interaction between the two high-energy photons and a real electron and positron are produced as a result. A Feynman diagram of this process is depicted in Figure 5.1.

A critical issue with realising the Breit-Wheeler process experimentally is that

[3]A derivation of the equation for proper time can be found in the Appendix.

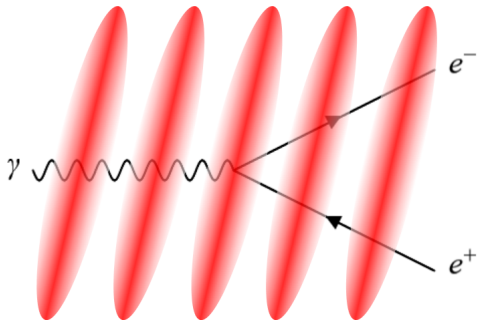



Figure 5.2: A Feynman diagram of the multi-photon Breit-Wheeler process.

it requires the sum of photon energies to exceed twice the rest mass of an electron (1.02 MeV). This requires each successful interaction to be between two photons, each of wavelength 2.4 nm[4]. However, it has been established that it is possible to undergo a multi-photon Breit-Wheeler process, a Feynman diagram of which is depicted in Figure 5.2 [157]. In multi-photon Breit-Wheeler, the usual formula:

$$\gamma + \gamma \longrightarrow e^- + e^+ \tag{5.16}$$

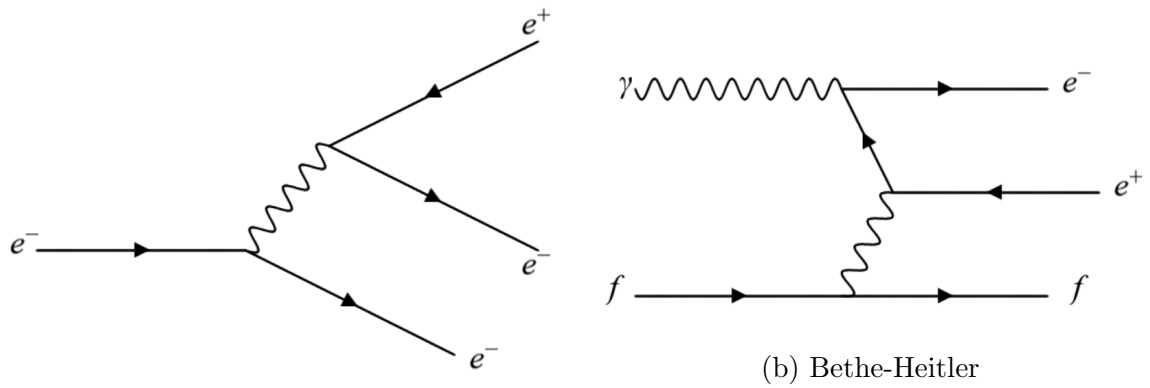
is modified to:

$$\gamma + n\omega \longrightarrow e^- + e^+ \tag{5.17}$$

where $n$ is some arbitrarily high number of photons of frequency, $\omega$. In this process, a high-energy photon decays into an electron-positron pair when propagating through an intense electromagnetic field. It is this version of the Breit-Wheeler process, as opposed to the pure version, that has been successfully measured using X-ray Free Electron Lasers [158][5], although has yet to be measured using high-power optical laser systems.

[4]This is easily verified using Planck's formula for photon energy $E = hc/\lambda$.

[5]It should be noted here that although the Breit-Wheeler process was measured using the Stanford Linear Accelerator, the bulk of the pair production was achieved through the Trident process.




(a) Trident

(b) Bethe-Heitler

Figure 5.3: Feynman diagrams of (a) the Trident and (b) the Bethe-Heitler processes.

### 5.2.3 Alternative Routes to Pair Production – the Trident and Bethe-Heitler Processes

For completeness, it is worth noting that the Breit-Wheeler process is not the only mechanism by which pair production can occur; although it is the lowest order-QED process for electron-positron production from pure light. Other mechanisms, such as the Trident [159] and Bethe-Heitler [160] processes, can also be significant contributors to pair production, amongst many other production routes. In Trident pair production, an accelerating electron radiates a virtual photon that spontaneously produces an electron-positron pair. In Bethe-Heitler pair production, a high-energy photon decays into an electron-positron pair after interaction with a spectator fermion[6], with said interaction mediated by a virtual photon. It is in fact these interactions, as opposed to Breit-Wheeler production, that has been researched the most [144,158,161], as it is significantly easier to stimulate pair production with high-energy particle beams as opposed to attempting to exploit photon-photon collisions.

[6]This spectator could be a quark, hadron, or lepton.

## 5.3 Combining ZVP & QED

In the original model for the ZVP absorption mechanism, the fast electron energy was deduced by assuming that the laser pressure displaces the electron fluid from the ionic background to set up a pseudo-capacitor system with the two charge fluids (of charge $Q$) acting as the "plates" of the pseudo-capacitor. As seen in Chapter 4, the scaling relation of Equation 4.41 holds up to a value of $a_0 = 100$.

Beyond $a_0 = 100$, QED effects – such as radiation reaction and pair production mentioned above – have the potential to contribute to laser-plasma interactions. Thus, the beginning of the new model considers applying these effects to perturb the pseudo-capacitor described in the previous chapter. Once pair production begins to occur, the rate of pair production has been demonstrated theoretically to increase logarithmically with laser intensity [144] and radiation is expected to inhibit the onset of relativistic transparency, thus maintaining the plasma's opacity [149]. In this scenario, ultra-high intensity laser pulses are expected to provide a sufficiently intense background electromagnetic field for the multi-photon Breit-Wheeler pair production process to be stimulated [157]. When these predictions are applied to the pre-existing ZVP model, this leads to the natural assumption that the rate of pair production will be maximal at the point of the laser's peak intensity.

The position of peak intensity has already been shown to coincide with the position to which the electron fluid is displaced by the laser pulse [58]. This is a direct consequence of the fact that the pseudo-capacitor's spatial extent is determined by balancing the radiation pressure of the incident laser pulse with the electrostatic pressure set up by the uncompensated, undisplaced positive space charge. With electron-positron pairs being produced at one of the pseudo-capacitor's "plates", it is necessary to modify the model described in Chapter 4 to account for the introduction of these additional particles. A pictorial representation of their addition is depicted in Figure 5.4.

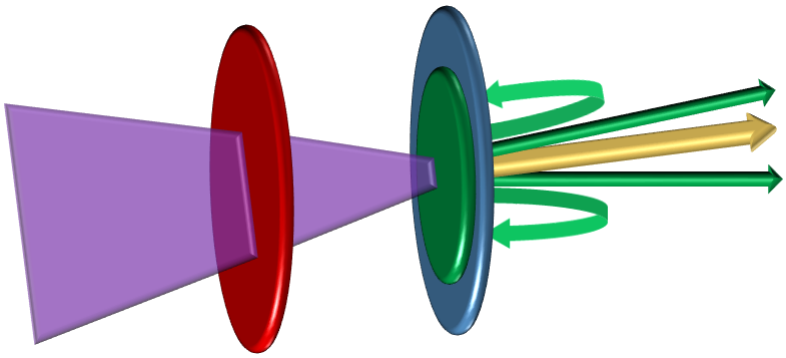


Figure 5.4: A pictorial representation of the proposed modification to the ZVP mechanism that includes QED effects. The pseudo-capacitor – characterised by a displaced electron fluid (blue) and a consequent region of net positive space charge (red) – is augmented by pair production at the peak intensity of the incident laser pulse (faded purple) on the negative "plate". The positrons (yellow) are not subjected to a restoring force and therefore propagate into the bulk plasma, leaving the region of interest. In contrast, some of the pair-produced electrons (green) feel a restoring force which keeps some fraction of them within the region of interest. This effectively increases the net charge in the region of the original negative "plate".

The electron-positron pairs will be created with high energies and high momenta directed predominantly in the laser-forward direction. Thus, although all the pair-produced particles will be immediately subjected to the electric field of the pseudo-capacitor, it is predicted that the positrons will propagate unhindered into the quasi-neutral bulk of the plasma. This prediction is made because the direction of the electric field within the pseudo-capacitor should act to expel the positrons from the region of interest. In contrast, some fraction, $\mathcal{F}$, of the pair-produced electrons could be captured onto the negative "plate" by the electric field of the pseudo-capacitor, as shown in Figure 5.4. It transpires, and will be shown imminently, that the number of captured electrons dramatically changes the energy scaling relation of Equation 4.41.

## 5.4 New Energy Scaling

To determine how many pair-produced electrons will be captured and bound to the negative pseudo-capacitor "plate", it is necessary to compare the kinetic energy re-

quired to escape from the pseudo-capacitor's electric field, $T_{\text{esc}}$, with the average energy of the pair produced electronic energy distribution, $\langle U \rangle$.

The escape energy, one would expect, will be equal to the energy required to break free from the electric field of the pseudo-capacitor, and so ought to be of the same order of magnitude as the energy that an electron would gain by crossing the capacitor. This has been shown to be proportional to $a_0^2$ in Chapter 4 (*cf.* Equation 4.41).

Meanwhile, numerical investigations into the Bethe-Heitler process have found that the average energy of pair-produced positrons is proportional to $1/a_0$ [161]. By considering the symmetry of the Bethe-Heitler, and the other pair production processes depicted in Figures 5.1,5.2 and 5.3, it is inferred that the pair-produced electronic energy distribution will share this $a_0^{-1}$ scaling.

If one considers the pair-produced electronic energy distribution $f(\varepsilon)$, where $\varepsilon$ is the ratio of energy to $\langle U \rangle$, then the number of captured electrons can be expressed by:

$$\mathcal{F} \propto f(\varepsilon \leq T_{\text{esc}}/\langle U \rangle) \tag{5.18}$$

To simplify the consideration of the distribution function in Equation 5.18, it is useful to compare the order of magnitude of $T_{\text{esc}}$ to $\langle U \rangle$. Research into pair production deep into the QED regime has found that typical distribution functions have average energies on the order of giga-electronvolts (GeV) [147,161]. In contrast, extrapolating the results presented in Figure 4.10, suggests that even at values of $a_0$ as extreme as 500, the escape energy should not at any point exceed 300 MeV. Given the order of magnitude difference - if not more - between $T_{\text{esc}}$ and $\langle U \rangle$, it is both possible and reasonable to Taylor expand the distribution function $f(\varepsilon)$. Preserving only first-order terms means that Equation 5.18 becomes:

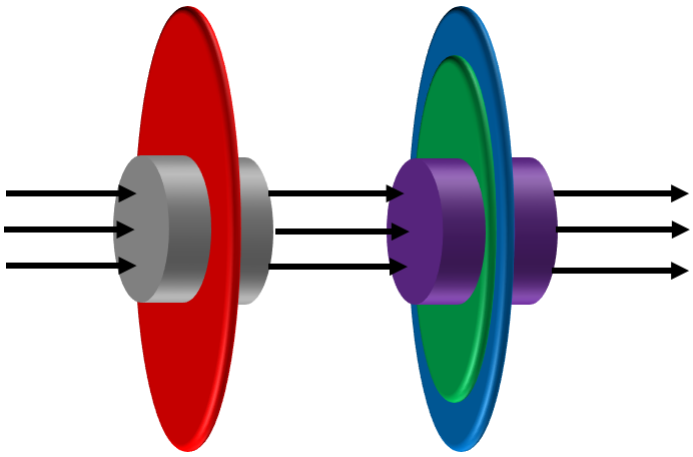


Figure 5.5: A schematic indicating the Gaussian surfaces used to modify the ZVP theory to include QED effects. One Gaussian surface (grey) envelops the positive space charge "plate" (red), while the other Gaussian surface (purple) envelops the combination of both the original displaced electron fluid (blue) and the captured pair-produced electrons (green). The calculated electric field (black arrows) intersects the flat faces of both Gaussian surfaces at normal incidence.

$$\mathcal{F} \propto \frac{T_{\mathrm{esc}}}{\langle U \rangle} \equiv a_0^3 \tag{5.19}$$

The final consideration, now, is to examine how these additional electrons on the negative "plate" of the pseudo-capacitor impact the energy scaling of the fast electrons. The first step is to consider how the electric field of the pseudo-capacitor is modified. At QED-relevant intensities, the positive space charge of magnitude $Q$ is unaffected, but the charge associated with the net negative region must be modified to account for the additional electrons that disrupt the displaced electron fluid. The total charge of the highly localised negative region can be expressed as:

$$Q_{-} = -Q(1 + \mathcal{F}) \tag{5.20}$$

The next step is to apply Gauss' law to the Gaussian surface depicted in Figure

5.5 such that:

$$\begin{aligned} \iint \vec{E}_+ \cdot d\vec{\varsigma} &= \frac{Q}{\epsilon_0} \\ \iint \vec{E}_- \cdot d\vec{\varsigma} &= -\frac{Q}{\epsilon_0}(1+\mathcal{F}) \end{aligned} \tag{5.21}$$

which leads to:

$$\begin{aligned} E_+ &= \frac{Q}{2\varsigma\epsilon_0} \\ E_- &= \frac{Q}{2\varsigma\epsilon_0}(1+\mathcal{F}) \end{aligned} \tag{5.22}$$

where $\varsigma$ is again the cross-sectional area of the pseudo-capacitor "plates" and Equation 5.21 has been evaluated to yield Equation 5.22 with the zeroes of each plate's coordinate system defined as being in the centre of each plate. By applying the solutions in Equation 5.22 to a coordinate system with a common zero, it is easily deduced that:

$$E' = E_+ - E_- = \frac{Q}{\varsigma\epsilon_0}\left(1+\frac{1}{2}\mathcal{F}\right) \tag{5.23}$$

Therefore, the kinetic energy, $T$, of the fast electrons can be calculated by considering the energy gained as an electron crosses the quasi-neutral region under the influence of the electric field given in Equation 5.23, from the area of uncompensated negative charge to the uncompensated ion charge:

$$T = e\vec{E}' \cdot \Delta\vec{r} \propto \frac{a_0^2}{n_\mathrm{e}\lambda^2}\left(1+\frac{1}{2}\mathcal{F}\right) \tag{5.24}$$

By using the scaling relation derived in Equation 5.19, this yields:

$$T \propto a_0^5 \tag{5.25}$$

provided that $\mathcal{F} \geq 6.4$. With a cubic increase in the dependence of $T$ on $a_0$ it is

expected that upon entering the QED regime, the change in electron energy scaling with incident laser intensity will become swiftly apparent.

It is important to note here that while the scaling relation for the energy of the most energetic electrons is predicted to transition from Equation 4.41 to Equation 5.25 upon entry into the QED regime, this does not necessarily mean that the scaling of total laser-energy absorption will follow the same relation. Indeed, it has already been highlighted in Chapter 4 that while in the post-ponderomotive regime the fastest electrons' energies scale with $a_0^2$, the total amount of laser-energy absorbed will scale with $a_0^3$. However, when considering the total absorption after entering the QED regime, it is more difficult to predict the scaling relation as the energy could be partitioned amongst the original electrons, ions, re-radiated as coherent x-rays, distributed in surface waves as plasmons [162], radiated as high-energy bremsstrahlung, partitioned into the pair-produced leptons, or eventually re-radiated as post-annihilation gamma-ray photons. For this reason, it is expected that the scaling of the highest energy in the electron energy spectrum with laser intensity (as opposed to total absorption) will provide the clearest potential experimental signature of entry into the QED regime.

## 5.5 Numerical Validation of the QED-ZVP Model

As in Chapter 4, in lieu of experimental measurements to verify the model described above, fully relativistic and kinetic particle-in-cell simulations are needed to model the interaction. In this case, however, the PIC codes must also be QED-inclusive. To this end, while OSIRIS was the code of choice for the work presented in Chapter 4, the need to include QED calculations led to the use of a different code, EPOCH [50]. Unlike OSIRIS, EPOCH is an open-source code and its QED package is well-established and recorded in the literature [163][7]. In the case of EPOCH (and indeed OSIRIS), the

[7]The author must insist at this point that OSIRIS and EPOCH are both excellent and professional standard codes. The decision to switch from one to the other was a matter of personal taste and

QED package appends a Monte Carlo integrator that calculates the probabilities and subsequently rates of pair-production and radiation reaction, amongst other QED effects. These probabilities and rates are then combined with a pre-determined random seed number (part of the input of any PIC simulation) to output QED processes in a semi-random way that reflects the probabilistic, as opposed to deterministic, nature of quantum events.

Another difference between EPOCH and OSIRIS is that while OSIRIS takes the previously mentioned dimensionless inputs, EPOCH operates in a blissful reality where all units are defined in the Système Internationale. Therefore to ensure that the conversion from the OSIRIS results of Chapter 4 to the EPOCH results in this Chapter is accurate, a number of overlaps were made in the intensity scan discussed below. OSIRIS was used to run simulations for values of $a_0$ in the range 100-250, to ensure that the results of Chapter 4 could be faithfully extended. EPOCH was then used to run simulations for values of $a_0$ in the range 100-560 to ensure that the unit conversion from OSIRIS' system to the SI units was faithful to reality before extending into new regimes of physics.

### 5.5.1 Simulation Setup

The grid for the simulations presented in this chapter was set to be a square of side length $125\,k_0^{-1}$ ($20\,\mu$m). For resolution, there were 16 cells per $k_0^{-1}$ ($100\,\mu\text{m}^{-1}$) in the $\hat{x}$-direction and 4 cells per $k_0^{-1}$ ($25\,\mu\text{m}^{-1}$) in the $\hat{y}$-direction. The simulation was run for a total time of $375\,\omega_0^{-1}$ (200 fs) with a time step of $5 \times 10^{-3}\,\omega_0^{-1}$ (2.5 as).

The plasma targets were simulated using 500 macro-electrons and 20 macro-ions per cell with the mass:charge ratio of the ions being set at 3660 times larger than that of the electron (fully ionised aluminium in the EPOCH simulations[8]). In contrast

convenience - OSIRIS' QED package is also fully functional and has been seen to produce some fantastically interesting results [164]

[8]The mass:charge ratio of fully ionised aluminium is approximately $2m_\text{p}/m_\text{e}$, where $m_\text{p}$ is the

to the simulations presented in Chapter 4, the targets in these simulations were modelled as simple rectangular slabs with a thickness of $6.25\,k_0^{-1}$ ($1\,\mu$m). The front of the target was characterised with an exponentially decaying density profile of decay-scale length $1.25\,k_0^{-1}$ ($0.2\,\mu$m). The density of the bulk of the slab was set to $50n_c$ ($5.55 \times 10^{22}\,\mathrm{cm}^{-3}$).

The laser pulse was simulated as a Gaussian pulse with pulse duration $160\,\omega_0^{-1}$ (85 fs) and a wavelength of $1\,\mu$m specified in the EPOCH simulations. The laser was polarised in the $\hat{y}$-direction and focused down to a spot diameter of $12\pi k_0^{-1}$ ($6\,\mu$m). The normalised vector potential of the pulse was varied from $a_0 = 100$ to $a_0 = 600$ over the course of the simulation campaign. Similar to Chapter 4, Table 5.1 is provided to demonstrate the conversion factors between the variables used in OSIRIS and EPOCH simulations.

### 5.5.2 Extracted Energy Scaling

The process for determining the energy scaling of the fast electrons with laser intensity in the simulations presented in this chapter is the same as that described in Chapter 4. When extracting the energy of the 5% most energetic electrons, averaging, and plotting for values of $a_0$ between 100 and 600, this led to the data presented in Figure 5.6. The first point of note is that there is a near-perfect level of agreement between the EPOCH and OSIRIS simulations. This is a particularly important result as it confirms that the results presented both here, and in Chapter 4, are genuine numerical results and not computational errors arising from a quirk in the compiling of either code.

It also seems apparent from Figure 5.6 that there is an acceleration in the trend for fast electron energy vs. incident laser $a_0$. Before being able to attribute this to QED effects, it is important to identify when the QED regime has been entered.

proton rest mass.

| Parameter | Dimensionless Value | S.I. value ($\lambda = 1\,\mu$m) |
|---|---|---|
| Grid size | $125k_0^{-1} \times 125k_0^{-1}$ | $20\,\mu\text{m} \times 20\,\mu\text{m}$ |
| | | |
| $\hat{x}$-resolution | 16 cells per $k_0^{-1}$ | 10 nm |
| $\hat{y}$-resolution | 4 cells per $k_0^{-1}$ | 40 nm |
| | | |
| Simulation Duration | $375\omega_0^{-1}$ | 200 fs |
| Time Step | $5 \times 10^{-3}\omega_0^{-1}$ | 2.5 as |
| | | |
| Target scale-length | $1.25k_0^{-1}$ | $0.2\,\mu$m |
| | | |
| Electron density | $50n_c$ | $5.6 \times 10^{22}\,\text{cm}^{-3}$ |
| | | |
| Pulse duration | $160\omega_0^{-1}$ | 85 fs |
| Focussed spot diameter | $12\pi k_0^{-1}$ | $6\,\mu$m |
| | | |
| | 100 | $1.4 \times 10^{22}\,\text{W cm}^{-2}$ |
| | 150 | $3.1 \times 10^{22}\,\text{W cm}^{-2}$ |
| | 200 | $5.6 \times 10^{22}\,\text{W cm}^{-2}$ |
| | 250 | $8.8 \times 10^{22}\,\text{W cm}^{-2}$ |
| | 300 | $1.3 \times 10^{23}\,\text{W cm}^{-2}$ |
| Intensity ($a_0$) | 350 | $1.8 \times 10^{23}\,\text{W cm}^{-2}$ |
| | 400 | $2.2 \times 10^{23}\,\text{W cm}^{-2}$ |
| | 450 | $2.8 \times 10^{23}\,\text{W cm}^{-2}$ |
| | 500 | $3.5 \times 10^{23}\,\text{W cm}^{-2}$ |
| | 550 | $4.2 \times 10^{23}\,\text{W cm}^{-2}$ |
| | 600 | $5 \times 10^{23}\,\text{W cm}^{-2}$ |

Table 5.1: Conversion factors between the dimensionless variables used as inputs in OSIRIS and variables with units in the Système Internationale (as used in EPOCH), assuming the laser wavelength is equal to $1\,\mu$m.

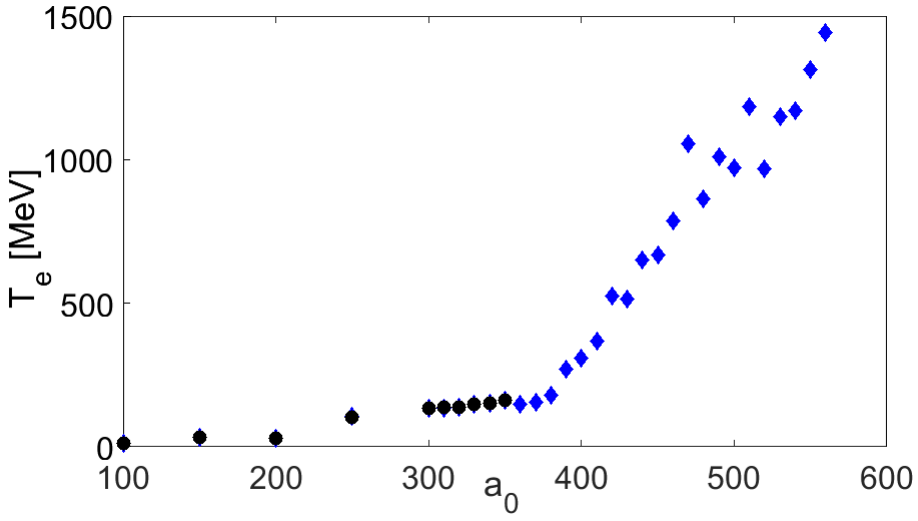



Figure 5.6: Plot of extracted fast electron energy against incident laser $a_0$. Filled-in black circles indicate the results from OSIRIS simulations, while blue diamonds indicate the results from the EPOCH simulations. The QED Monte Carlo package is active. Although mostly obscured, there is an EPOCH data point corresponding to each OSIRIS data point; this indicates that there is an excellent level of agreement between the two codes.

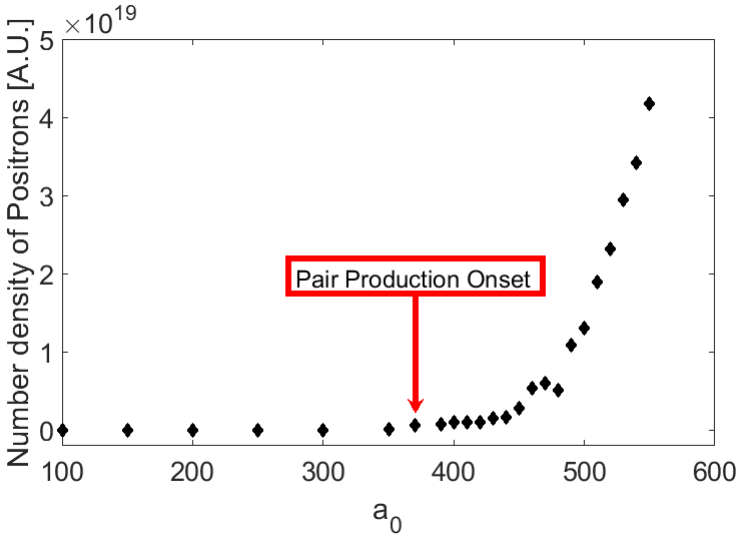



Figure 5.7: Number density of positrons measured in EPOCH simulations within a region of interest bounded by the point of laser focus and extending 0.2 $\mu$m into the bulk plasma.

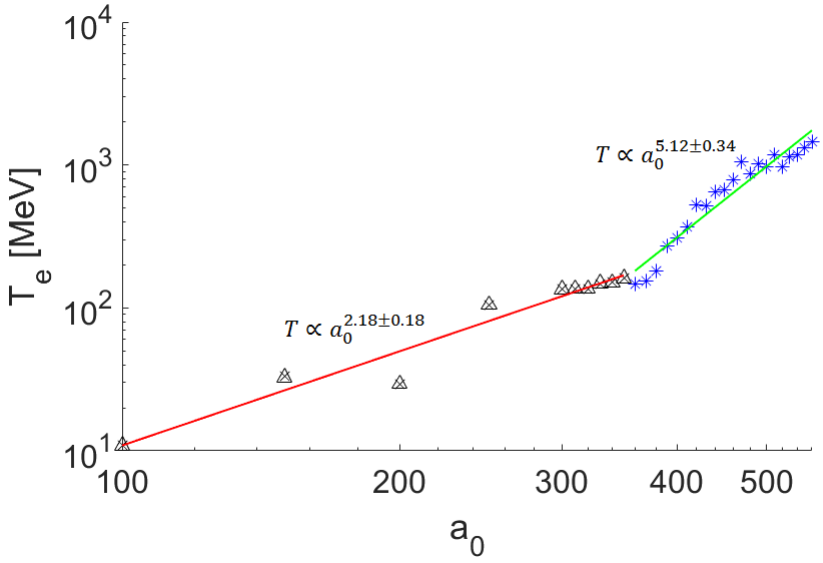



Figure 5.8: Plot of extracted fast electron energy against incident laser $a_0$. Black triangles indicate EPOCH simulations for which no positrons were measured, while the black crosses indicate equivalent OSIRIS simulations. The red line is a fit to both sets of data corresponding to $T \propto a_0^{2.18\pm0.18}$. The blue asterisks indicate results from EPOCH simulations for which positrons were detected. The green line is a fit corresponding to $T \propto a_0^{5.12\pm0.34}$. There is a clear correlation between the onset of pair production and the dramatic shift in energy scaling.

The easiest measure of this in the simulations is to extract the positron density from a region of interest. In the case of this simulation campaign, the region of interest was bounded by the the position of the laser focus, extending $1\,\mu$m into the bulk plasma, and bounded by the full transverse width of the plasma slab. A plot of the extracted positron number density is shown in Figure 5.7. From this, it is clear that pair-production onsets at a value of $a_0 = 360$, corresponding to approximately $1.9 \times 10^{23}\,\mathrm{W\,cm^{-2}}$. This then motivates cleaving the simulation data presented in Figure 5.6 into two sets: the QED and non-QED data sets.

Figure 5.8 displays the information that can be obtained by dividing the data into QED-apparent and QED-absent data sets. In the non-QED regime:

$$T \propto a_0^{2.18\pm0.18} \tag{5.26}$$

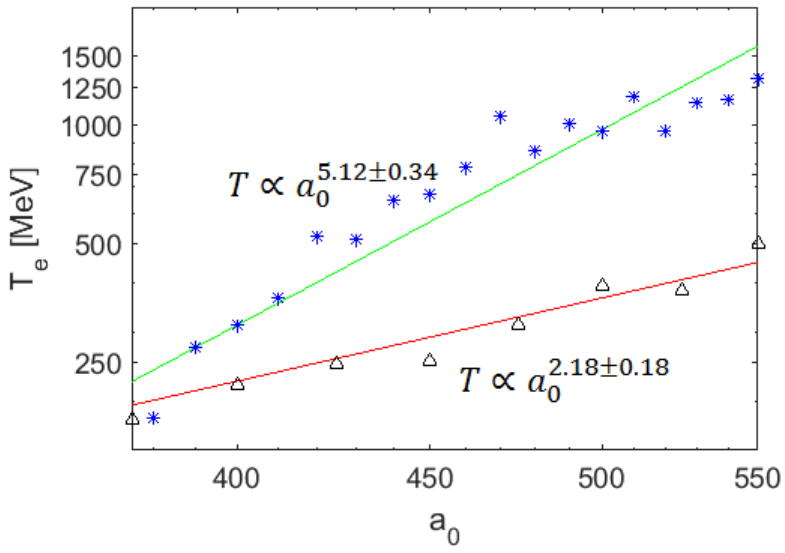



Figure 5.9: A comparison of QED-inclusive (blue asterisks with green fitted line) and QED-exclusive (black triangles with red fitted line) results from EPOCH simulations of the ZVP mechanism for values of $a_0$ between 350 and 550. The divergence between the two cases is evidently significant and increases quickly with $a_0$. Both sets of data follow the same power law scaling as in Figure 5.8.

which, somewhat unsurprisingly, agrees to within error with the results of Chapter 4 and published work investigating the ZVP mechanism [57, 58].

In contrast, upon entering the QED regime, the dependence of the fast electron energy on the laser intensity changes dramatically to:

$$T \propto a_0^{5.12\pm0.34} \tag{5.27}$$

This is in excellent agreement with the prediction of Equation 5.25, and so lends confidence to the notion that the simulation data validates the hypothesis expressed in Equation 5.25.

To definitively ascertain that the dramatic change in the scaling relation is due to QED effects such as pair production, additional EPOCH simulations were run with the Monte Carlo QED package suppressed. The results in these simulations were then compared to the results from the QED-inclusive simulations, as shown in Figure 5.9.

From these results, it can be seen that the immediate change to an $a_0^5$ scaling relation, as predicted in Equation 5.25, leads to a significant divergence from the workings of the ZVP mechanism, as described by Equation 4.41.

## 5.6 Exploiting High-Intensity HHG XUV Radiation

Given the distinct regime change for electronic energy absorption that is coincident with the onset of quantum electrodynamic effects, it seems plausible to conclude that QED processes such as pair production dramatically augment absorption in the post-ponderomotive regime. Such a significant change in energy scaling potentially makes experimental measurements of the ZVP mechanism a candidate for being a clear and unambiguous indicator that future high-power laser systems (such as the Extreme Light Infrastructure) have truly breached the energy barrier into the QED regime. This clarity could provide future experimental campaigns that access a wealth of unexplored physics with confidence that quantum electrodynamics is truly playing a role in extreme high energy density physics.

Due to the potentially high risk nature of conducting an experimental campaign to investigate an entirely new and previously unobserved phenomenon, any responsible approach to such a campaign should include a contingency plan or "back-up experiment". A natural candidate for such a contingency plan is the investigation of the applicability of the coherent HHG XUV radiation to warm dense matter studies. One particular application is the potential for using high-order harmonics to heat solid matter to temperatures of interest to the warm dense matter community [165]. In order to better inform any potential experiment, an extensive set of hydrodynamics simulations were conducted investigating the potential heating effect of the high-order harmonics on a tamped aluminium target, using the one-dimensional

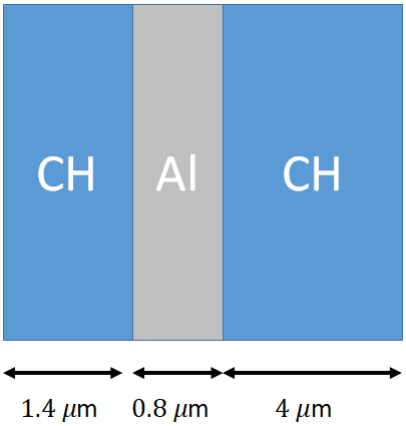



Figure 5.10: A schematic of the aluminium, target tamped in plastic, used in the hydrodynamics HELIOS simulations.

radiative-hydrodynamics code HELIOS [47].

### 5.6.1 Target Profile

The target design is an aluminium slab, tamped on either side by a thick layer of plastic, a schematic can be seen in Figure 5.10. The use of tamping layers increases the relevance of the investigation to warm dense matter studies, as the plastic inhibits the aluminium's expansion into vacuum: thus obtaining a better approximation to isochoric heating [94, 165].

### 5.6.2 Harmonic Profile

The radiation profile required the intensity of each harmonic to be inputted individually. HELIOS then combined the inputted photon fluxes to form a single radiation flux source with several frequencies.

The inputted frequencies can be deduced by considering the conservation of energy:

$$f_{\mathrm{HHG}} I_0 \varsigma_0 = \sum_q I_q \varsigma_q \tag{5.28}$$

where $f_{\mathrm{HHG}}$ is the efficiency of the high-harmonic generation, $I_0$ is the intensity of the incident fundamental beam, $\varsigma_0$ is the area of the focal spot, and $I_q$ is the intensity and $\varsigma_q$ the focal spot area of the $q^{\mathrm{th}}$ harmonic.

By recognising that the radius of the potential focal spot for each harmonic must scale inversely with the harmonic order[9], such that $\varsigma_q = \varsigma_0 q^{-2}$ and employing Equation 2.82, Equation 5.28 can be re-written as:

$$f_{\mathrm{HHG}} I_0 = I_1 \sum_q q^{-14/3} \tag{5.29}$$

By noting that the sum in Equation 5.29 is simply a Riemann-zeta function, the Intensity of each harmonic can be expressed as:

$$I_q = \frac{f_{\mathrm{HHG}} I_0}{\zeta(\frac{14}{3})} q^{-8/3} \tag{5.30}$$

where $\zeta(\frac{14}{3}) \approx 1.05$ is the known value of the Riemann-zeta function.

### 5.6.3 Hydrodynamics Simulations

The heating of the tamped aluminium target depicted in Figure 5.10 by a HHG XUV source with spectral intensities matching Equation 5.30 was modelled using the hydrodynamics code HELIOS [47]. HELIOS uses a Lagrangian approach to solving Equations 1.7-1.11. The incident radiation was modelled to have a spectrum comprising a series of delta peaks of amplitude matching Equation 5.30 for each harmonic frequency. Varying numbers of harmonics were modelled in each simulation run, but HELIOS required a minimum of two radiation frequencies to be inputted in order to compile without error. Most simulations considered harmonic orders with $q > 15$, and no simulations exceeded a harmonic order of $q = 46$. The front tamp was modelled to be $1.4\,\mu$m thick by 50 hydrodynamic zones, while the rear tamp was also modelled by

[9]The size of the focal spot scales with wavelength, as a consequence of the diffraction limit, and therefore inversely with harmonic order.

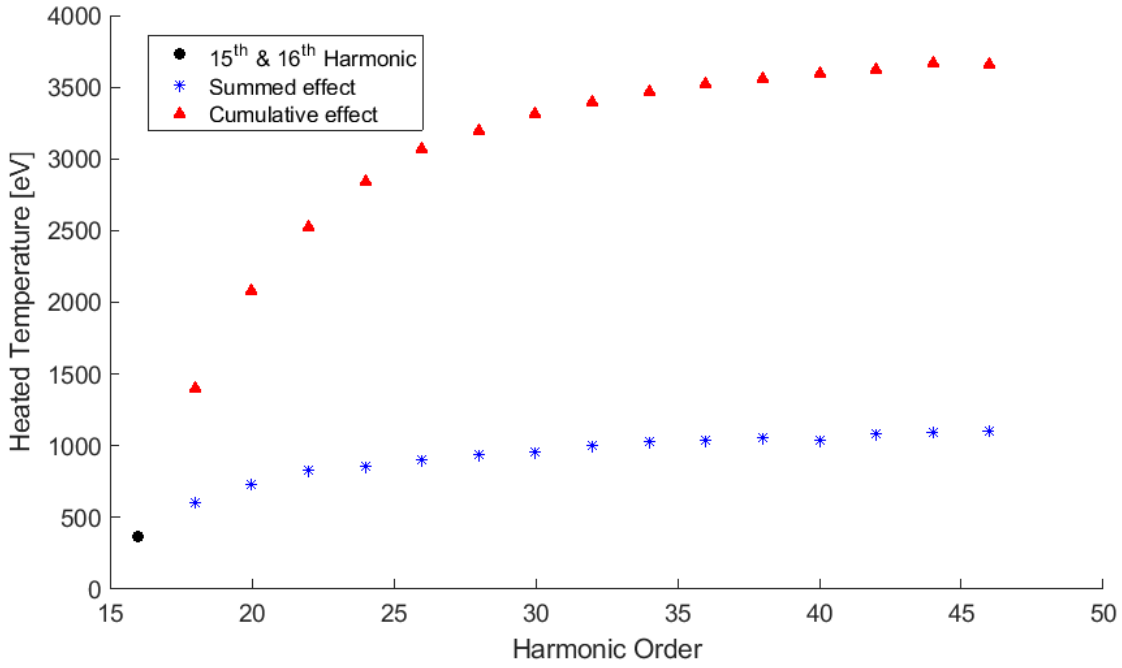



Figure 5.11: Plot of the temperature to which a tamped aluminium slab is heated by coherent XUV radiation. Red triangles indicate the cumulative effect of heating using all harmonics from the $15^{\text{th}}$ up to the harmonic indicated on the $x$-axis simultaneously. Blue asterisks indicate the summed effect of the heating from each pair of harmonics (e.g. $15^{\text{th}}$ & $16^{\text{th}}$ or $21^{\text{st}}$ & $22^{\text{nd}}$) used separately. The black circle indicates the mutual point of the effect of heating from the $15^{\text{th}}$ & $16^{\text{th}}$ harmonic.

50 hydrodynamic zones but set to a thickness of 4 $\mu$m. The central aluminium slab was modelled with a higher resolution: using 40 zones to span a 0.8 $\mu$m thickness. The entirety of the target was initiated at room temperature (0.025 eV), and was run to model 2 ns of heating with the time step automatically adjusted by the HELIOS code to ensure the Courant condition (*cf.* Equation 1.20) was satisfied for all time steps.

The simulation data was divided into two sets. In both sets, each data point corresponded to a different harmonic being the highest-order harmonic in the spectrum. In the first data set, the hereafter named "cumulative heating" data set, for data point, $n$, all of the harmonics from $q = 15$ up to the highest-order harmonic $q = 14 + 2n$ were included in the radiation flux input file. In contrast, for the second

data set – now named the "summed heating" data set, a series of simulations was conducted modelling the heating effect of individual pairs of harmonics, starting from the $q = 15\,\&\,16$ pair and increasing incrementally in a sequence:

$$q = 15\,\&\,16,\ \ 17\,\&\,18,\ \ 19\,\&\,20, ....., 13 + 2n \& 14 + 2n, ....., \tag{5.31}$$

$$q_k = 13 + 2k\,\&\,14 + 2k \tag{5.32}$$

The $n^{\text{th}}$ data point in the summed heating data set was obtained by summing the individual effects of all the pairs starting from $q_1$ up and including $q_n$.

The results of both data-sets (including the shared data point corresponding to the effects of the $15^{\text{th}}$ and $16^{\text{th}}$ harmonics) are displayed in Figure 5.11. One point of note is that while the summed heating effect barely exceeds 1 keV; the cumulative effect of simultaneously incident harmonics heats the aluminium block to over 3.5 keV. This is easily explained by the fact that in the cumulative case, the photon flux is sufficient to penetrate through the front plastic tamp layer, and so the x-rays directly heat the aluminium slab. In contrast, in the summed case, the bulk of the photons for each pair are absorbed within the plastic tamp, and the aluminium is heated via thermal conduction from the heated plastic layer.

## 5.7 Proposed Measurement of QED-augmented ZVP Absorption

Continuing the theme of the previous two chapters, this chapter will conclude with an outline of a possible experiment that could be used to determine the validity of the QED modification to the ZVP theory. Failing that, it contains the contingency plan to measure the heating effect of the HHG XUV radiation, as described in the previous section. Again maintaining the theme of the previous chapters, this experiment design

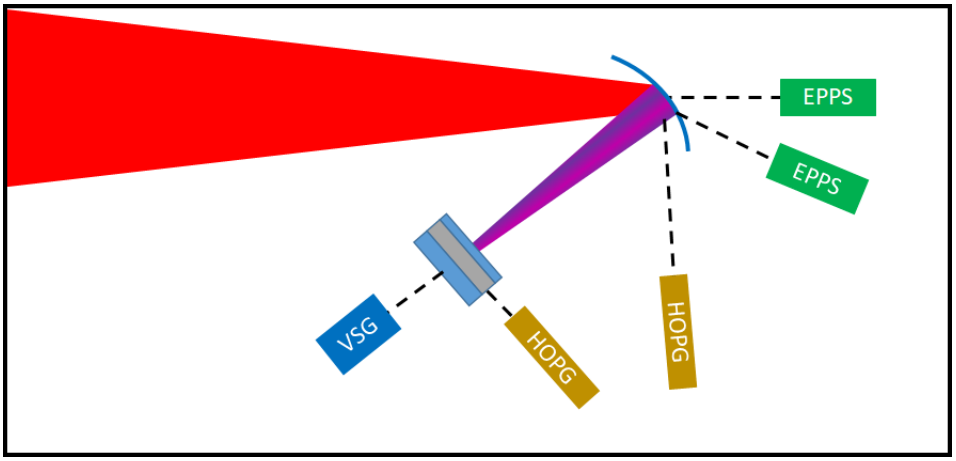



Figure 5.12: A schematic for the potential experiment that could be conducted using an ELI-like system to investigate the QED modification to the ZVP mechanism, and the potential heating effect of the coherently generated XUV radiation. The incident laser pulse (red) is fired incident on the "ZVP target" (light blue). Radiation from High Harmonic Generation (pink/purple) is focused onto the tamped aluminium target. An EPPS (green) is set up in the laser-forward direction, and another in the laser-forward+30° direction, to measure the fast electron energy spectrum as well as the number and spectrum of pair-produced positrons. A HOPG spectrometer is set to measure the temperature of the "ZVP target" via X-ray emission spectroscopy. A second HOPG spectrometer is set to measure the temperature of the tamped target by the same method. Finally, a VSG spectrometer is used to measure the temperature of the tamped target via absorption spectroscopy. It should be noted that, as discussed in Chapter 4, there is a strong possibility that the high harmonics generated on the plasma surface will not be in the direction of specular reflection, but rather counter-propagating against the laser pulse's direction of incidence. As noted in Chapter 4, this possibility merits further investigation: both numerical and experimental.

includes the use of foam targets to optimise the plasma homogeneity and obtain the desired plasma density.

### 5.7.1 Target Parameters

Provided the laser system operates at a wavelength of 1 $\mu$m, using a plasma with density of $5.5 \times 10^{22}\,\mathrm{cm}^{-3}$ is a practical and suitable choice for the ZVP generation target as it is easily manufactured as a solid density target, and the density is sufficiently high that the relativistiv similarity parameter $S > 1$, meaning that the ZVP mechanism is viable. Ideally, this target would be curved into a parabola, with radius of

curvature equal to approximately 80 $\mu$m. This would allow the harmonics generated on the front surface to be focused onto a secondary target.

This secondary target – the harmonic heating target – matches the schematic of Figure 5.10: a 0.8 $\mu$m section of aluminium tamped between a pair of polyethylene slices of thicknesses 1.4 $\mu$m on the harmonic-facing side, and 4 $\mu$m on the opposite side.

### 5.7.2 Laser Parameters

The laser system proposed for this potential experiment does not yet exist, although a mid-lifetime upgrade to the Extreme Light Infrastructure's ATON laser [40] could enable laser systems to reach intensities of $10^{24}\,\mathrm{W\,cm^{-2}}$ - corresponding to an $a_0$ of 850 (assuming a wavelength of 1 $\mu$m).

### 5.7.3 Diagnostics

The list of diagnostics proposed to measure both the existence of the QED modification to the ZVP mechanism and the potential heating effect of any harmonics is as follows:

- A pair of Highly Oriented Pyrolytic Graphite (HOPG) Crystal spectrometers to measure the X-ray emission from the ZVP, and heating targets respectively [134].
- A pair of Electron-Positron-Proton Spectrometers (EPPS) to measure the fast electron spectrum. The EPPS's will also be used to measure the existence, and number of produced positrons [143].
- A Variable Spaced Grating (VSG) spectrometer to measure the absorption spectrum of the heated tamped target [166].

### 5.7.4 Target Chamber & Campaign Design

A schematic of a potential target chamber set-up, using a fictional rectangular target chamber is presented in Figure 5.12. In a similar vein to the previous chapter, it is suggested orienting the two EPPS's at different angles to obtain more than one electron spectrum. The use of two EPPS's also serves an additional purpose: it will provide information about the number of pair-produced positrons, as well as their energy spectrum and the angular distribution of these particles.

A HOPG spectrometer aimed at the "ZVP target" will serve to measure the plasma temperature and density. Meanwhile, a second HOPG spectrometer oriented at the tamped aluminium target will perform the same measurement on the tamped target.

To obtain corroborating information about the temperature measurement of the tamped target, a VSG spectrometer will be set up along the axis of XUV-propagation to measure the absorption spectrum of the tamped aluminium. Informed by previous experimental campaigns, a strong magnet ($\mathcal{O} \sim 1\,\mathrm{T}$) needs to be placed immediately in front of the VSG to divert any potentially co-propagating fast electrons [165]. These fast electrons, when incident on a VSG could induce fluorescence inside the spectrometer.

Provided QED effects are achievable with the laser system in use, the two EPPS's should be sufficient to measure the fast electron energy scaling and the successful production of positrons. Regardless of the success of the main aim of the experiment, the combination of a HOPG and VSG is expected to successfully measure the heating effect of the coherent XUV radiation on the tamped aluminium target.

## 5.8 Summary

In this chapter the work of Chapter 4 was continued. The classical theory presented in the previous chapter was generalised to a relativistically-inclusive model, where it was seen that the ZVP mechanism should still persist in relativistic conditions.

Some of the lowest-order processes by which pair-production can take place were introduced and briefly described. This was followed by an exposition of a theory that models how the onset of QED processes dramatically modifies the ZVP absorption mechanism. It was shown that the fast electron energy scaling immediately and evidently shifts from a quadratic scaling with $a_0$ to a quintic scaling. The theory was followed by a discussion of the results from an extensive particle-in-cell simulation campaign to test the model. The results were seen to be in excellent agreement with the predictions of the newly introduced theory, validating the prediction that the change from quadratic to quintic scaling coincides with the onset of pair production.

Following the results of the particle-in-cell simulations, the chapter changed tack. The findings of a series of hydrodynamics simulations were presented. These simulations investigated the potential heating effect of the coherent XUV radiation generated by High Harmonic Generation at the plasma surface on a tamped aluminium target. It was found that the tamped aluminium could reach temperatures in excess of 3.5 keV.

The chapter was concluded with a brief description of a potential experiment that could test the results of both sets of simulation campaigns presented in this chapter. While the experiment relies on the existence of laser technology that has yet to be realised, the trajectory of laser performance depicted in Figure 1.3, leaves the author optimistically confident that this experiment will be realisable in the near future.

# Chapter 6

# Conclusions

## 6.1 Summary of Results

This thesis has presented analytical and numerical research focusing on designing experimental campaigns for the next generation of high-power laser experiments. The experimental designs presented within this thesis have been informed by the large number of experiments the author has worked on and led across a diverse range of laser facilities: from femtosecond-class systems such as the Astra-Gemini laser at the Central Laser Facility [167], to petawatt-class systems such as Vulcan [44], kilojoule-class systems such as the National Ignition Facility's Advanced Radiographic Capability [168], and even free electron laser systems such as the FLASH facility at the Deutsches Elektronen-Synchroton [169].

In Chapter 3, the case for developing a quasimonoenergetic ion source as a platform for quantitative measurements of proton radiography was put forward. It was noted that Haberberger *et al.*'s results measuring Collisionless Shock Acceleration using the 10 $\mu$m $CO_2$ laser at UCLA ought to be transferable to petawatt- and kilojoule-class laser systems operating at 1 $\mu$m. By expanding on a distribution function model introduced by Cairns *et al.* [55, 56] an analytic form for the distribution function of

CSA-produced ions was derived. This was seen to match well with historical experimental data.

Further, a wholly new relativistic generalisation of this approach was derived and presented. Both the classical and relativistic formulations of the distribution functions were used to definitively map out the parameter space within which one could expect CSA to be a viable mechanism for accelerating ions. It was found that while the parameter space is narrow, by increasing the ratio of the electron temperature to the ion temperature, it is possible to extend the viable parameter space to one where the Mach number of the electrostatic shock is within the range $1 < M < 1.56$.

A series of 1D hydrodynamics simulations were then used to establish where in the viable parameter space that current petawatt- and kilojoule-class laser systems ~~were~~are able to reach. It was seen that these systems all occupy the upper limit of the parameter space where the most energetic ions are anticipated to be produced. Motivated by these results, an experiment was designed for the Vulcan laser to investigate CSA. Given that CSA is only possible in plasma only slightly denser than the critical density [109], a key part of the experiment design was the implementation of novel "mid-density" targets made of plastic-based foams.

Chapter 3 ended with an acknowledgement that current understanding of laser-energy absorption at intensities relevant to the next generation of high-power laser systems (i.e. the multi-petawatt-scale systems of the future) may not be sufficient to model laser-plasma interactions in this potentially new regime. Understanding laser-plasma interactions, in particular laser-energy absorption is of critical importance when considering designing and conducting experimental investigations into more complicated phenomena such as ion acceleration.

This line of reasoning inevitably led to a segue into the research presented in Chapters 4 and 5. The arguments for considering the possibility of a post-ponderomotive regime of laser-energy absorption were presented. One particular candidate for post-

ponderomotive absorption mechanisms, the Zero Vector Potential mechanism was introduced. The initially 1D model devised by Baeva *et al.* [57] was fully expanded into three dimensions. A physically intuitive model for how the energy of electrons that have absorbed laser light scales with both incident laser intensity and plasma electron number density was derived and presented.

The predictions of the ZVP model, both qualitative and quantitative were then comprehensively validated through an extensive campaign of particle-in-cell simulations. The results of these simulations showed excellent agreement with all facets of the ZVP theory, including the propagation of "zeroes" in the vector potential beyond the critical density surface, efficient high harmonic generation and the fast electron energy scaling of $T \propto a_0^2/n_\mathrm{e}$.

The validation of the predictions of the ZVP theory was followed by a numerical investigation into the efficiency of the absorption process. It was found that the efficiency of ZVP absorption scaled as $f_\mathrm{ZVP} \propto S^{-1}$, where $S$ is Gordienko's relativistic similarity parameter [137], up to a value of $\sim 60\%$. One potential explanation for this is that at lower intensities, the laser is less capable of channelling or hole boring through the plasma. Thus, at lower intensities the plasma surface is less disrupted and this yields a higher efficiency for high harmonic generation - it seems plausible that the efficiency of high harmonic generation scales linearly with $S$. With more energy in the reflected harmonics, there is less incident laser light for the electrons to interact with and absorb energy from. Thus, it is sensible that the efficiency of the ZVP mechanism scales inversely with the relativistic similarity parameter.

Chapter 5 took the work presented in Chapter 4 through to its natural continuation: investigating the interaction of progressively more intense laser pulses with critically over-dense plasma. As intensities rise to levels where spontaneous electron-positron pair production is possible, it is necessary to modify the theory behind laser-energy absorption to include quantum electrodynamic effects.

Due to this need for a new theory, just such a model was devised and presented in Chapter 5. An assumption was made that in the "low" intensity part of the laser-QED regime, the pseudo-capacitor model characteristic of ZVP absorption would still feature. It was also assumed that pair production would predominantly take place at the point of best focus for the laser, corresponding to the position of the negative "plate" of the pseudo-capacitor. Thus, any pair-produced positrons were hypothesised to leave the region of interest and not play a leading role in the absorption dynamics of the system.

In contrast, some fraction of the pair-produced electrons are expected to be captured onto the negative plate of the pseudo-capacitor. This then introduces a perturbation to the ZVP system which modifies the fast electron energy scaling with intensity from a quadratic dependence on $a_0$, to a quintic dependence. This theory predicts that while radiation reaction is not expected to alter the fast electron energy scaling, the onset of pair production - which occurs at slightly higher intensities than the onset of radiation reaction - will immediately induce a dramatic shift in the energy scaling from $T \propto a_0^2$ to $T \propto a_0^5$.

Similar to the approach demonstrated in Chapter 4, an extensive campaign of particle-in-cell simulations was conducted and presented to verify the validity of the hypothesis regarding the QED modification to the ZVP theory. This campaign was a notable success for the newly minted theory. Not only was the shift in scaling perfectly coincident with the first detection of positrons in the simulation space, it was eminently clear that the deviation from an extrapolated quadratic scaling with $a_0$ is significant. The deviation is potentially sufficiently significant to use it as an experimental signature of a laser-plasma experiment's entry into the laser-QED regime.

As a corollary to the relatively high efficiency of High Harmonic Generation, a potential application of this XUV radiation was investigated. Namely, the potential

heating effect on solid density matter to create material in the regime of warm dense matter. By running numerous hydrodynamics simulations, it was determined that an unfiltered, focused HHG-XUV spectrum could heat a tamped aluminium block to over 3.5 keV but that with a judicious choice of filtering, heating across a broad temperature range from 500 eV up to 3.5 keV could be achieved.

## 6.2 Future Work

It is a rare piece of good fortune in scientific endeavours for the future direction of research to be clear and relatively straightforward to define. However, in the case of the work presented in this thesis, there are a number of immediately obvious avenues to pursue.

In the case of shock acceleration, it is clear that the most immediate next step is to conduct the experiment proposed in Section 3.5, as planned, at the end of 2019. This experiment is designed and hoped to be a proof-of-principle campaign to establish the viability of Collisionless Shock Acceleration on 1 $\mu$m laser systems. Provided the experiment is successful, the Vulcan campaign could pave the way for a series of laser-plasma experiments to establish a ~~qualitative~~quantitative proton radiography platform for imaging hohlraums used in Inertial Confinement Fusion experiments based on CSA. This could be achieved by developing the platform on progressively larger laser systems, moving from Vulcan to Orion at the Atomic Weapons Establishment or the OMEGA-EP system at the Laboratory for Laser Energetics in the University of Rochester, and finally to the National Ignition Facility's Advanced Radiographic Capability (NIF ARC) or the Laser MegaJoule PETawatt Aquitaine Laser (LMJ-PETAL) systems.

In addition to the potential for developing a proton radiography platform, CSA generated ions could also have an application in hadron therapy [18]. In order to

make hadron therapy a reality, narrow-band 200 MeV ion sources are needed, and they need to be producible by tabletop-scale laser systems (otherwise they won't fit in hospitals!). Given the enormous physical scale of current petawatt-class laser systems, it is likely to be innovative target design that pushes experiments towards the medically applicable threshold.

In the context of investigating the post-ponderomotive and laser-QED regime, there are still clearly experimental, numerical, and theoretical investigations to conduct. Experimentally, the immediately obvious next step is to apply for access to the ~~Hercules~~HERCULES laser system and conduct the experiment outlined in Section 4.6. This could then be logically followed by an experimental campaign on the Extreme Light Infrastructure Beamlines, as discussed in Section 5.7.

These experiments will need to be accompanied by extensive numerical and theoretical work. The numerical work that discovered the inverse dependence of ZVP absorption efficiency with the relativistic similarity parameter merits further investigation. In particular, it is desirable to construct a mathematical model that captures the physics of the system and explains the origin of this dependence. It is possible, and indeed plausible, that the hypothesis that the ZVP absorption efficiency is linked to the efficiency of coherent x-ray generation; this could form the starting point for the search for a theoretical model that includes considerations of absorption efficiency.

The research discussed in Chapter 5 can also be pursued further. As it stands, the post-ponderomotive regime has been modelled up to the cusp of the laser-QED regime. The next logical step is to develop a theory that joins this entry into the laser-QED regime with numerical results and theories that have considered processes deep into the QED regime, where quantum electrodynamics is the dominant dynamical system, as opposed to a perturbation (as is the case for the regime discussed in Chapter 5) [144, 146–148, 151, 161, 163, 170, 171]. To supplement this, a rigourous and extensive campaign of particle-in-cell simulations is required to model the dynamics

as descriptions transition from the barely-QED regime to the deeply-QED regime[1].

Finally, the hydrodynamics modelling that investigated the applications of focused XUV harmonics onto a tamped aluminium target indicated that coherently generated high harmonics could heat solid material to keV-scale temperatures. These results need to be systematically and thoroughly compared with modelling and experimental data for the heating effect of other x-ray sources such as synchrotons and free electron lasers. Regardless of how the XUV-harmonics stack up against these larger-scale sources, the utility of these harmonics as a source is undeniable. It has the potential to make dozens more high-power laser facilities suitable laboratories for warm dense matter investigations, something that is critically important to the high energy-density physics community given the scarcity of free electron lasers in the world.

It is hopefully clear to the reader from this chapter that there are a multitude of different avenues in this field that are ready for exploration. This thesis has explored the prospect of exploiting new technologies, both in terms of current state-of-the-art target design and impending extremely-high-power laser systems to investigate new regimes of laser-plasma interactions. The theoretical and numerical work presented herein is just one small part of the necessary and exciting work that will take the high energy-density physics community's understanding of the fundamentals of plasma dynamics to novel frontiers. For many, including the author, the most exciting prospect from this field is the possibility of using this research to develop new platforms that can contribute to realising dramatic sociological advances such as thermonuclear fusion and novel medical treatments.

[1]The author anticipates that developing a theory for this intermediary regime will be difficult, somewhat analogously to the theoretical description for atomic line splitting in the presence of a magnetic field: weak field perturbations are well described by the theory of the Zeeman effect and strong field perturbations are well described by the Paschen-Back effect. The intermediate regime between the two, however, is ill-described by analytic models.

# Appendix A

# Derivations in Full

This appendix contains the full derivations for some of the equations presented in the main body of the thesis, where the full derivation would obscure the results or descriptions provided.

## A.1 Equation 1.19: Velocity calculated for PIC codes via Leapfrogging

Beginning with Equation 1.18:

$$\vec{v}_{t+1/2} = \vec{v}_{t-1/2} + \frac{Q}{m}\left(\vec{E}_t + \frac{\vec{v}_{t+1/2} + \vec{v}_{t-1/2}}{2} \times \vec{B}_t\right)\Delta t \tag{A.1}$$

Re-writing $\vec{v}_{t+1/2} = \vec{v}$ and $\vec{v}_{t-1/2} = \vec{u}$ and re-arranging yields:

$$\vec{v} - \frac{Q\Delta t}{2m}(\vec{v} \times \vec{B}) = \vec{u} + \frac{Q\Delta t}{m}\left(\vec{E} + \frac{\vec{u}}{2} \times \vec{B}\right) \tag{A.2}$$

The components of Equation A.2 can be written into a matrix:

$$\begin{pmatrix} 1 & -GB_z & GB_y \\ GB_z & 1 & -GB_x \\ -GB_y & GB_x & 1 \end{pmatrix} \begin{pmatrix} v_x \\ v_y \\ v_z \end{pmatrix} = \begin{pmatrix} \mathcal{G}_x \\ \mathcal{G}_y \\ \mathcal{G}_z \end{pmatrix} \tag{A.3}$$

where $G = Q\Delta t/2m$ and $\mathcal{G}_i = u_i + G(2E_i + \epsilon_{ijk}u_jB_k)$ is the $i^{\text{th}}$ component of the right-hand side of Equation A.2, and $\epsilon_{ijk}$ is the Levi-Civita symbol.

The inverse of the matrix in Equation A.3 is:

$$\frac{1}{1+G^2|B|^2} \begin{pmatrix} 1+G^2B_x^2 & G^2B_xB_y + GB_z & G^2B_xB_z - GB_y \\ G^2B_xB_y - GB_z & 1+G^2B_y^2 & G^2B_yB_z + GB_x \\ G^2B_xB_z + GB_y & G^2B_yB_z - GB_x & 1+G^2B_z^2 \end{pmatrix} \tag{A.4}$$

Which can be written in index notation[1] as:

$$M_{ij} = \delta_{ij} + G\epsilon_{ijk}B_k + G^2B_iB_j \tag{A.5}$$

where $\delta_{ij}$ is the Kronecker delta.

Therefore, Equation A.3 can be re-written in index notation:

$$v_i = M_{ij}\mathcal{G}_j \tag{A.6}$$

$$v_i = \frac{(\delta_{ij} + G\epsilon_{ijk}B_k + G^2B_iB_j) \times [u_j + G(2E_j + \epsilon_{jlm}u_lB_m)]}{1+G^2|B|^2} \tag{A.7}$$

$$v_i = \frac{1}{1+G^2|B|^2} \times \big((u_i + G\epsilon_{ijk}u_jB_k + G^2u_jB_jB_i 2GE_i + 2G^2\epsilon_{ijk}E_jB_k + 2G^3E_jB_jB_i + G\epsilon_{ilm}u_lB_m + G^2\epsilon_{ijk}\epsilon_{jlm}u_lB_kB_m + G^3\epsilon_{jlm}B_lu_lB_mB_i\big) \tag{A.8}$$

[1]Einstein's summation convention is applied throughout all uses of index notation.

By using the permutability of the Levi-Civita symbol and the identity:

$$\epsilon_{ijk}\epsilon_{ilm} = \delta_{jl}\delta_{km} - \delta_{jm}\delta_{kl} \tag{A.9}$$

Equation A.8 can be simplified:

$$v_i = \frac{1}{1+G^2|B|^2} \times \left[u_i\left(1 - G^2 B_k B_k\right) + 2GE_i + 2G\epsilon_{ijk}(u_j + GE_j)B_k + 2G^2(u_j + GE_j)B_j B_i\right] \tag{A.10}$$

From this stage, it is relatively trivial to recover Equation 1.19:

$$\begin{aligned}\vec{v}_{t+1/2} = \frac{1}{1+(Q\Delta t|B_t|/2m)^2} \times \Bigg\{ &\left[1 - \left(\frac{Q\Delta t}{2m}\right)^2\right]\vec{v}_{t-1/2} + \frac{Q\Delta t}{m}(\vec{E}_t + \vec{v}_{t-1/2} \times \vec{B}_t) \\ &+ \left(\frac{Q\Delta t}{2m}\right)^2 \left[2\left(\vec{v}_{t-1/2} + \frac{Q\Delta t}{2m}\vec{E}_t\right)\cdot \vec{B}_t\right]\vec{B}_t + \frac{1}{2}\left(\frac{Q\Delta t}{m}\right)^2 \vec{E}_t \times \vec{B}_t \Bigg\}\end{aligned} \tag{A.11}$$

## A.2 Resonant Absorption - Section 2.4

Beginning with Equation 2.38:

$$\nabla^2\vec{E} - \frac{\eta^2(z)}{c^2}\frac{\partial^2\vec{E}}{\partial t^2} = 0 \tag{A.12}$$

Assuming that $\eta$ is given by Equation 2.37, and that the conditions are those portrayed in Figure 2.2; in the case of s-polarisation, Equation A.12 can be written as:

$$\frac{\partial^2 E_x}{\partial y^2} + \frac{\partial^2 E_x}{\partial z^2} + \frac{\omega^2}{c^2}\eta^2(z)E_x = 0 \tag{A.13}$$

This can be expressed as a separable partial differential equation as in Equation 2.39:

$$-\frac{1}{E_x}\frac{\partial^2 E_x}{\partial y^2} = \frac{1}{E_x}\frac{\partial^2 E_x}{\partial z^2} + \frac{\omega^2}{c^2}\eta^2(z) = k_y^2 \tag{A.14}$$

Considering just the $y$-dependence of $E_x$ yields:

$$E_x = E(z)\left[G_1 \exp(ik_y y) + G_2 \exp(-ik_y y)\right] \tag{A.15}$$

which by applying the boundary condition of the incident wave travelling in the negative $y$-direction, and by recognising that the wave-vector, $k_y$ is not involved in any interactions and is therefore conserved to be that when far from the plasma (i.e. $k_y = \omega \sin\theta/c$, $G_2 = 0$) recovers Equation 2.41:

$$E_x = E(z) \exp\left[-i\omega(t - \frac{y}{c}\sin\theta)\right] \tag{A.16}$$

Substituting Equation A.16 into Equation A.14 and taking the Fourier transform gives an equation for the $z$-component of the wave-vector:

$$k_z^2 = \frac{\omega^2}{c^2}(\eta^2(z) - \sin^2\theta) \tag{A.17}$$

Given that the reflection must happen when $k_z$ is zero, this implies that the reflection surface occurs at $\eta^2(z) = \sin^2\theta$. As the refractive index of a plasma can be written as:

$$\eta^2(z) = 1 - \frac{\omega_{\mathrm{p}^2}(z)}{\omega^2} \equiv 1 - \frac{n_{\mathrm{e}}(z)}{n_{\mathrm{c}}} \tag{A.18}$$

which then naturally yields Equation 2.43:

$$n_{\mathrm{refl}} = n_{\mathrm{c}} \cos^2\theta \tag{A.19}$$

If p-polarised light is now considered, it has been shown in Equation 2.45 that there is clearly a resonance in the electric field when $n_{\mathrm{e}} = n_{\mathrm{c}}$. To evaluate the magnitude of the electric field at the critical density surface, it is easiest to consider the s-polarised

magnetic field:

$$\vec{B} = B(z) \exp\left[-i(\omega t - \omega y \sin\theta/c)\right] \hat{x} \tag{A.20}$$

Given that Ampere's law can be written as:

$$\nabla \times \vec{B} = \mu\sigma\vec{E} + \epsilon\mu\frac{\partial\vec{E}}{\partial t} = \frac{-i\omega}{c^2}\left(1 - \frac{n_{\mathrm{e}}(z)}{n_{\mathrm{c}}}\right)\vec{E} \tag{A.21}$$

Which, if considering only the $z$-component of this equation yields:

$$\frac{-i\omega}{c}\sin\theta B(z) = \frac{-i\omega}{c^2}\left(1 - \frac{n_{\mathrm{e}}(z)}{n_{\mathrm{c}}}\right)E_z \tag{A.22}$$

$$\therefore E_z = \frac{cB(z)\sin\theta}{1 - n_{\mathrm{e}}(z)/n_{\mathrm{c}}} \tag{A.23}$$

If a linear density ramp is considered such that:

$$n_{\mathrm{e}}(z) = \begin{cases} 0, & z < 0 \\ n_{\mathrm{c}} z/\delta, & 0 < z < \delta \\ n_{\mathrm{c}}, & z > \delta \end{cases} \tag{A.24}$$

and that the magnetic field will be exponentially attenuated from the reflection surface to the critical density surface such that Equation 2.47 holds:

$$B(z = \delta) = B(z = \delta\cos^2\theta) \times e^{-\alpha} \tag{A.25}$$

Then it follows that the first term to identify is $B(z = \delta\cos^2\theta)$ from a modified form of Equation A.13:

$$\frac{\mathrm{d}^2 B}{\mathrm{d}z^2} + \frac{\omega^2}{c^2}\left(1 - \frac{n_{\mathrm{e}}(z)}{n_{\mathrm{c}}} - \sin^2\theta\right)B = 0 \tag{A.26}$$

which can be readily simplified to:

$$\frac{\mathrm{d}^2 B}{\mathrm{d}z^2} - \frac{\omega^2}{c^2}\left(\frac{z - \delta\cos^2\theta}{\delta}\right) B = 0 \tag{A.27}$$

By employing the substitution $\tilde{z} = (z - \delta\cos^2\theta)(\omega^2/\delta c^2)^{1/3}$, Equation A.27 can be simplified to the Airy Equation:

$$\frac{\mathrm{d}^2 B}{\mathrm{d}\tilde{z}^2} - \tilde{z}B = 0 \tag{A.28}$$

The solutions to this equation are the Airy functions. Given that the second Airy function diverges for ever-increasing arguments, it can be discounted on physical grounds. This leaves the solution for the magnetic field amplitude as:

$$B = \begin{cases} G \times \mathrm{Ai}(\tilde{z}) & z > 0 \\ E_0/c & z < 0 \end{cases} \tag{A.29}$$

Equating these two cases at $z = 0$, and numerically evaluating the Airy function [64] yields:

$$G = \frac{E_0}{c}\mathrm{Ai}\left[-\cos^2\theta\left(\frac{\omega\delta}{c}\right)^{2/3}\right] \approx \frac{2}{\sqrt{\pi}}\frac{E_0}{c}\left(\frac{c}{\omega\delta}\right)^{1/6} \tag{A.30}$$

Thus it is possible to calculate the value of the magnetic field at the reflection surface as given in Equation 2.50:

$$B(z = \delta\cos^2\theta) \approx 0.9\frac{E_0}{c}\left(\frac{c}{\omega\delta}\right)^{1/6} \tag{A.31}$$

The next step in the derivation is to consider the exponential decay factor, $\alpha$, which is an integral of the index of refraction, $\eta$, from the reflection surface to the

critical density surface:

$$\alpha = \int_{\delta\cos^2\theta}^{\delta} \frac{\mathrm{d}z}{c}\sqrt{\omega_{\mathrm{p}}^2(z) - \omega^2\cos^2\theta} \equiv \int_{\delta\cos^{\theta}}^{\delta} \mathrm{d}z\frac{\omega}{c}\left(\frac{z}{\delta} - \cos^2\theta\right)^{1/2} = \frac{2}{3}\frac{\omega\delta}{c}\sin^3\theta \tag{A.32}$$

By combining Equations A.31 and A.32 an expression for the magnetic field at the critical density surface can be obtained:

$$B(z=\delta) \approx 0.9\frac{E_0}{c}\left(\frac{c}{\omega\delta}\right)^{1/6} \times \exp\left[-\frac{2}{3}\frac{\omega\delta}{c}\sin^3\theta\right] \tag{A.33}$$

If the function $\xi$, is now defined such that:

$$\xi = 2.3\left(\frac{\omega\delta}{c}\right)^{1/3}\sin\theta \times \exp\left[-\frac{2}{3}\frac{\omega\delta}{c}\sin^3\theta\right] \tag{A.34}$$

then Equation A.23 is solved (as in Equation 2.52) to be:

$$E_z \approx \frac{E_0\xi}{1 - z/\delta}\sqrt{\frac{c}{2\pi\omega\delta}} \tag{A.35}$$

In order to consider the absorption fraction, $f_{\mathrm{res}}$, for resonant absorption processes, it is necessary to include damping in the description of the electric field. This is done trivially by recalling that the $1-z/\delta$ term originates from $1-\omega_{\mathrm{p}}^2/\omega^2$, which can easily be modified:

$$1 - \frac{z}{\delta} \longrightarrow 1 - \frac{z}{\delta}\left(1 - i\frac{\nu}{\omega}\right) \tag{A.36}$$

Thus, when considering the fraction of light that is absorbed, the following integral (as seen in Equation 2.54) is recovered:

$$f_{\mathrm{res}} = \frac{1}{E_0^2}\int_0^{\infty}\frac{\nu E_z^2}{c}\mathrm{d}z = \frac{\nu\xi^2}{2\pi\omega\delta}\int_0^{\infty}\frac{\mathrm{d}z}{(1-z/\delta)^2 + (\nu/\omega)^2} \tag{A.37}$$

which can be calculated exactly:

$$\int_0^\infty \frac{\mathrm{d}z}{(1-z/\delta)^2+(\nu/\omega)^2} = \frac{\pi\omega\delta}{\nu} \tag{A.38}$$

and thus Equation 2.55 can be recovered:

$$f_{\mathrm{res}} = \frac{1}{2}\xi^2 \tag{A.39}$$

## A.3 Vacuum Heating - Section 2.5

Beginning with Equation 2.60:

$$\frac{\omega}{\omega_{\mathrm{p}}}\sin\omega_{\mathrm{p}}t_{\mathrm{c}} - \sin\omega t_{\mathrm{c}} = -\frac{2\pi x_0}{a_0\lambda}\left(\frac{\omega_{\mathrm{p}}^2}{\omega^2}-1\right) \tag{A.40}$$

To determine the skin depth, $\delta$, beyond which no electron will be pulled out into the vacuum, consider that the electric field of the laser must be forcing the electron back into the plasma, i.e. $-\sin\omega t$ must be positive. For the maximum possible value of $x_0$, the $\sin\omega_{\mathrm{p}}t$ term in Equation A.40 must be in anti-phase with this laser term and so:

$$1+\frac{\omega}{\omega_{\mathrm{p}}} = \frac{2\pi}{a_0\lambda}\left(\frac{\omega_{\mathrm{p}}^2}{\omega^2}-1\right)\delta \tag{A.41}$$

This then recovers Equation 2.61:

$$\delta = \lambda\frac{a_0}{2\pi}\frac{\omega/\omega_{\mathrm{p}}}{(\omega_{\mathrm{p}}/\omega)-1} \tag{A.42}$$

To determine the absorption fraction, $f_{\mathrm{vh}}$, from vacuum heating, begin with Equation 2.62:

$$\frac{1}{2}m_{\mathrm{e}}v_{\mathrm{osc}}^2 n_{\mathrm{e}}\delta\frac{\omega}{2\pi} = \frac{1}{2}f_{\mathrm{vh}}\epsilon_0 c E_L^2\cos\theta \tag{A.43}$$

By taking the maximum possible amplitude for the velocity from Equation 2.59 as:

$$v_{\mathrm{osc}} = \frac{2a_0 c}{(\omega_{\mathrm{p}}/\omega)^2 - 1} \tag{A.44}$$

and subsequently substituting Equations 2.14, 2.27, A.42, and A.44 into Equation A.43 yields:

$$\frac{1}{2} m_e \frac{4a_0^2 c^2}{[(\omega_{\mathrm{p}}/\omega)^2 - 1]^2} \omega_{\mathrm{p}}^2 \frac{m_{\mathrm{e}} \epsilon_0}{e^2} \frac{\lambda a_0}{2\pi} \frac{\omega/\omega_{\mathrm{p}}}{(\omega_{\mathrm{p}}/\omega) - 1} \frac{\omega}{2\pi} = \frac{1}{2} f_{\mathrm{vh}} \epsilon_0 \frac{m_{\mathrm{e}}^2 \omega^2 c^3}{e^2} a_0^2 \tag{A.45}$$

This can be drastically simplified to the form given in Equation 2.64:

$$f_{\mathrm{vh}} = \left[ \frac{2}{\pi} \frac{1}{(\omega_{\mathrm{p}}^2/\omega^2 - 1)^2 (1 - \omega/\omega_{\mathrm{p}})} \frac{1}{\cos\theta} \right] a_0 \tag{A.46}$$

## A.4 Integrating the Error Function - Section 3.2

Integrating the error function by parts yields:

$$\int \mathrm{erf}(x)\mathrm{d}x = x\mathrm{erf}(x) - \int \frac{2x}{\sqrt{\pi}} \exp(-x^2)\mathrm{d}x \tag{A.47}$$

Therefore:

$$\int \mathrm{erf}(x)\mathrm{d}x = x\mathrm{erf}(x) + \frac{e^{-x^2}}{\sqrt{\pi}} + C \tag{A.48}$$

## A.5 Combination of Relativistic Velocities - Section 3.3.2

Suppose three velocities: $w$ being a combination of $u$ and $v$; the differential forms for small spatial and temporal displacements in the frame relevant to $w$ can be linked to

those in the frame relevant to $u$ by a Lorentz boost using the speed $v$:

$$\mathrm{d}x_w = \gamma_\mathrm{v}\left(\mathrm{d}x_u + v\mathrm{d}t_u\right) \tag{A.49}$$

$$\mathrm{d}t_w = \gamma_v\left(\mathrm{d}t_u + \frac{v}{c^2}\mathrm{d}x_u\right) \tag{A.50}$$

This therefore yields:

$$w = \frac{u+v}{1+\frac{uv}{c^2}} \tag{A.51}$$

Now considering the Lorentz factor for the speed, $w$:

$$\gamma_w^2 = \frac{1}{1-w^2/c^2} = \frac{\left(1+\frac{uv}{c^2}\right)^2}{1+-\frac{u^2}{c^2}-\frac{v^2}{c^2}+\frac{u^2v^2}{c^4}} \tag{A.52}$$

By factorising the denominator, a form for $\gamma_w$ can be deduced:

$$\gamma_w = \gamma_u\gamma_v\left(1+\frac{uv}{c^2}\right) \tag{A.53}$$

## A.6 Equation 5.7 - The Headlight Effect

Consider the momentum 4-vector of a photon propagating in the $x-y$ plane at an angle $\theta$ to the $\hat{x}$-axis:

$$\mathbf{P}_\mu = (E/c, \vec{p}) = \left(\frac{E}{c}, \frac{E}{c}\cos\theta, \frac{E}{c}\sin\theta\right) \tag{A.54}$$

and apply the Lorentz transform:

$$\mathbf{P}'^\mu = \Lambda^\mu_\nu \mathbf{P}'^\nu \tag{A.55}$$

to yield three simultaneous equations:

$$E' = \gamma E(1 - \beta \cos\theta) \tag{A.56}$$

$$E' \cos\theta' = \gamma E(\cos\theta - \beta) \tag{A.57}$$

$$E' \sin\theta' = E \sin\theta \tag{A.58}$$

and so the results for the headlight effect can be derived:

$$\cos\theta' = \frac{\cos\theta - \beta}{1 - \beta\cos\theta} \tag{A.59}$$

$$\sin\theta' = \frac{1}{\gamma}\frac{\sin\theta}{1 - \beta\cos\theta} \tag{A.60}$$

## A.7 Equation 5.15 - The Proper Time Interval

The proper time interval can be defined as [125]:

$$\Delta\tau_{\mathrm{p}} = \int \frac{1}{c}\sqrt{-g_{\mu\nu}\mathrm{d}\mathbf{x}^{\mu}\mathrm{d}\mathbf{x}^{\nu}} \tag{A.61}$$

where $g_{\mu\nu}$ is the Minkowski metric defined as:

$$g_{\mu\nu} = \begin{pmatrix} -1 & 0 & 0 & 0 \\ 0 & 1 & 0 & 0 \\ 0 & 0 & 1 & 0 \\ 0 & 0 & 0 & 1 \end{pmatrix} \tag{A.62}$$

Using the metric as defined in Equation A.62, Equation A.61 can be simplified to:

$$\Delta\tau_{\mathrm{p}} = \int \sqrt{\mathrm{d}t^2 - \frac{\mathrm{d}x^2 + \mathrm{d}y^2 + \mathrm{d}z^2}{c^2}} = \int \sqrt{1 - \beta^2}\mathrm{d}t \tag{A.63}$$

This finally yields the result in Equation A.61:

$$\Delta\tau_{\mathrm{p}} = \int \frac{\mathrm{d}t}{\gamma(t)} \tag{A.64}$$

# References


[1] T. H. Maiman, "Stimulated Optical Radiation in Ruby," *Nature*, vol. 187, pp. 493–494, 1960.

[2] W. Paul, "Electromagnetic traps for charged and neutral particles," *Rev. Mod. Phys.*, vol. 62, pp. 531–540, 1990.

[3] R. E. Kidder, "Energy gain of laser-compressed pellets: a simple model calculation," *Nucl. Fusion*, vol. 16, p. 405, 1976.

[4] R. Betti, P. Y. Chang, B. K. Spears, K. S. Anderson, J. Edwards, M. Fatnejad, J. D. Lindl, R. L. McCrory, R. Nora, and D. Shvarts, "Thermonuclear ignition in inertial confinement fusion and comparison with magnetic confinement," *Phys. Plasmas*, vol. 17, p. 058102, 2010.

[5] J. Nuckolls, L. Wood, A. Thiessen, and G. Zimmerman, "Laser Compression of Matter to Super-High Densities: Thermonuclear (CTR) Applications," *Nature*, vol. 239, pp. 139–142, 1972.

[6] D. Strickland and G. Mourou, "Compression of amplified chirped optical pulses," *Opt. Commun.*, vol. 56, pp. 219 – 221, 1985.

[7] W. L. Kruer, *The physics of laser plasma interactions.* Redwood City, CA, USA: Wokingham: Addison-Wesley, 1988.

[8] F. F. Chen, *Introduction to Plasma Physics and Controlled Fusion.* Plenum Press, 1984.

[9] B. A. Remington, R. P. Drake, and D. D. Ryutov, "Experimental astrophysics with high power lasers and Z pinches," *Rev. Mod. Phys.*, vol. 78, pp. 755–807, 2006.

[10] P. Chabert and N. Braithwaite, *Physics of radio-frequency plasmas.* Cambridge University Press, 2011.

[11] A. L. Perrat, "Advances in Numerical Modeling of Astrophysical and Space Plasmas," *Astrophys. Space Sci.*, vol. 256, no. 1, pp. 51–75, 1997.

[12] V. D. Shafranov, "The initial period in the history of nuclear fusion research of the Kurchatov Institute," *Phys.-Usp.+*, vol. 44, no. 8, pp. 835–865, 2001.

[13] M. G. Haines, "The Joule Heating of a Stable Pinched Plasma," *Proc. Prog. Phys. Soc.*, vol. 76, no. 2, p. 250, 1960.

[14] P. K. Carroll and E. T. Kennedy, "Laser-produced plasmas," *Contemp. Phys.*, vol. 22, no. 1, pp. 61–96, 1981.

[15] R. Stenzel and A. Y. Wong, "Threshold and Saturation of Parametric Decay Instability," *Phys. Rev. Lett.*, vol. 28, no. 5, p. 274, 1972.

[16] T. Tajima and J. M. Dawson, "Laser Electron Accelerator," *Phys. Rev. Lett.*, vol. 43, pp. 267–270, 1979.

[17] A. Caldwell, K. Lotov, A. Pukhov, and F. Simon, "Proton-driven plasma-wakefield acceleration," *Nat. Phys.*, vol. 5, pp. 363–367, 2009.

[18] S. V. Bulanov, J. J. Wilkens, T. Z. Esirkepov, G. Korn, G. Kraft, S. D. Kraft, M. Molls, and V. S. Khoroshkov, "Laser ion acceleration for hadron therapy," *Usp. Fiz. Nauk+*, vol. 57, pp. 1149–1179, 2014.

[19] V. Malka, S. Fritzler, E. Lefebvre, E. d'Humières, R. Ferrand, G. Grillon, C. Albaret, S. Meyroneinc, J.-P. Chambaret, A. Antonetti, and D. Hulin, "Practicability of proton therapy using compact laser systems," *Med. Phys.*, vol. 31, pp. 1587–1592, 2004.

[20] J. H. Nuckolls, "Grand Challenges of Inertial Fusion Energy," *J. Conf. Ser.*, vol. 244, p. 012007, 2010.

[21] J. Colvin and J. Larsen, *Extreme Physics*. Cambridge University Press, 2014.

[22] C. A. J. Palmer, N. P. Dover, I. Pogorelsky, M. Babzien, G. I. Dudnikova, M. Ispiriyan, M. N. Polyanskiy, J. Schreiber, P. Shkolnikov, V. Yakimenko, and Z. Najmudin, "Monoenergetic Proton Beams Accelerated by a Radiation Pressure Driven Shock," *Phy. Rev. Lett.*, vol. 106, p. 014801, 2011.

[23] D. Haberberger, S. Tochitsky, F. Fiuza, C. Gong, R. A. Fonseca, L. O. Silva, W. B. Mori, and C. Joshi, "Collisionless shocks in laser-produced plasma generate monoenergetic high-energy proton beams," *Nat. Phys.*, vol. 8, pp. 95–99, 2011.

[24] S. C. Wilks, W. L. Kruer, M. Tabak, and A. B. Langdon, "Absorption of Ultra-Intense Laser Pulses," *Phys. Rev. Lett.*, vol. 69, pp. 1383–1386, 1992.

[25] S. C. Wilks and W. L. Kruer, "Absorption of Ultrashort, Ultra-Intense Laser Light by Solids and Overdense Plasmas," *IEEE J. Quantum Elect.*, vol. 33, pp. 1954–1968, 1997.

[26] R. A. Snavely, M. H. Key, S. P. Hatchett, T. E. Cowan, M. Roth, T. W. Phillips, M. A. Stoyer, E. A. Henry, T. C. Sangster, M. S. Singh, S. C. Wilks, A. MacKinnon, A. Offenberger, D. M. Pennington, K. Yasuike, A. B. Langdon, B. F. Lasinski, J. Johnson, M. D. Perry, and E. M. Campbell, "Intense High-

Energy Proton Beams from Petawatt-Laser Irradiation of Solids," *Phys. Rev. Lett.*, vol. 85, pp. 2945–2948, 2000.

[27] O. A. Hurricane, D. A. Callahan, D. T. Casey, P. M. Celliers, C. Cerjan, E. L. Dewald, T. R. Dittrich, T. Döppner, D. E. Hinkel, L. F. Berzak-Hopkins, J. L. Kline, S. LePape, T. Ma, A. G. MacPhee, J. L. Milovich, A. Pak, H.-S. Park, P. K. Patel, B. A. Remington, J. D. Salmonson, P. T. Springer, and R. Tommasini, "Fuel gain exceeding unity in an inertially confined fusion implosion," *Nature*, vol. 506, pp. 343–348, 2014.

[28] J. Limpouch, N. N. Demchenko, S. Y. Gus'kov, M. Kálal, A. Kasperczuk, V. N. Kondrashov, E. Krouský, K. Mašek, P. Pisarczyk, T. Pisarczyk, and V. B. Rozanov, "Laser interactions with plastic foam – metallic foil layered targets," *Plasma Phys. Control. Fusion*, vol. 46, pp. 1831–1841, 2004.

[29] K. Nagai, C. S. A. Musgrave, and W. Nazarov, "A review of low density porous materials used in laser plasma experiments," *Phys. Plasmas*, vol. 25, p. 030501, 2018.

[30] F. Pérez, J. D. Colvin, M. J. May, S. Charnvanichborikarn, S. O. Kucheyev, T. E. Felter, and K. B. Fournier, "High-power laser interaction with low-density C-Cu foams," *Phys. Plasmas*, vol. 22, p. 113112, 2015.

[31] L. Willingale, S. R. Nagel, A. G. R. Thomas, C. Bellei, R. J. Clarke, A. E. Dangor, R. Heathcote, M. C. Kaluza, C. Kamperidis, S. Kneip, K. Krushelnick, N. Lopes, S. P. D. Mangles, W. Nazarov, P. M. Nilson, and Z. Najmudin, "Characterization of High-Intensity Laser Propagation in the Relativistic Transparent Regime through Measurements of energetic Proton Beams," *Phys. Rev. Lett.*, vol. 102, p. 125002, 2009.

[32] W. P. Steckle Jr. and A. Nobile Jr., "Low-Density Materials for Use in Inertial Fusion Targets," *Fusion Sci. Technol.*, vol. 43, no. 3, pp. 301–306, 2003.

[33] K. S. W. Sing, D. H. Everett, R. A. W. Haul, L. Moscou, R. A. Pierotti, J. Roquérol, and T. Siemieniewska, "Reporting Physisorption Data for Gas/Solid Systems with Special Reference to the Determination of Surface Area and Porosity," *Pure Appl. Chem.*, vol. 57, no. 603, pp. 603–619, 1985.

[34] S. Slomkowski, J. V. Alemán, R. G. Gilbert, M. Hess, K. Horie, R. G. Jones, P. Kubisa, I. Meisel, W. Mormann, S. Penczek, and R. F. T. Stepto, "Terminology of polymers and polymerization processes in dispersed systems (IUPAC Recommendations 2011)," *Pure Appl. Chem.*, vol. 83, no. 12, pp. 2229–2259, 2011.

[35] K. Okada, S. Sakabe, H. Shiraga, T. Mochizuki, and C. Yamanaka, "Efficient Laser Absorption in Low Density Foam Target," *Jpn. J. Appl. Phys.*, vol. 21, no. 5, pp. L257–L259, 1982.

[36] W. L. Perry, R. C. Dye, P. G. Apen, L. Foreman, and E. Peterson, "Metallization of poly(4-methyl-1-pentene) microcellular foams," *Appl. Phys. Lett.*, vol. 66, no. 3, pp. 314–316, 1995.

[37] M. McHugh and V. Krukonis, *Supercritical Fluid Extraction.* Elsevier, 2013.

[38] A. Einstein, "Zur quantentheorie der strahlung," *Phys. Z*, vol. 18, no. 121, 1917.

[39] S. Hooker and C. Webb, *Laser Physics.* Oxford University Press, 2010.

[40] G. A. Mourou, C. L. Labaune, M. Dunne, N. Naumova, and V. T. Tikhonchuk, "Relativistic laser-matter interaction: from attosecond pulse generation to fast ignition," *Plasma Phys. Control. Fusion*, vol. 49, pp. B667–B675, 2007.

[41] A. Dubietis, G. Jonušauskas, and A. Piskarkas, "Powerful femtosecond pulse generation by chirped and stretched pulse parametric amplification in BBO crystal," *Opt. Commun.*, vol. 88, pp. 437–440, 1992.

[42] I. N. Ross, J. L. Collier, P. Matousek, C. N. Danson, D. Neely, R. M. Allott, D. A. Pepler, C. Hernandez-Gomez, and K. Osvay, "Generation of terawatt pulses by use of optical parametric chirped pulse amplification," *Appl. Optics*, vol. 39, no. 15, pp. 2422–2427, 2000.

[43] O. V. Chekhlov, J. L. Collier, I. N. Ross, P. K. Bates, M. Notley, C. Hernandez-Gomez, W. Shaikh, C. N. Danson, D. Neely, P. Matousek, S. Hancock, and L. Cardoso, "35 J broadband femtosecond optical parametric chirped pulse amplification system," *Opt. Lett.*, vol. 31, no. 24, pp. 3665–7, 2006.

[44] I. Musgrave, M. Galimberti, A. Boyle, C. Hernandez-Gomez, A. Kidd, B. Parry, D. Pepler, T. Winstone, and J. Collier, "Review of laser diagnostics at the Vulcan laser facility," *Laser Science and Engineering*, vol. 3, p. e26, 2015.

[45] J. P. Zou, C. LeBlanc, P. Audebert, S. Janicot, A. M. Sautivet, L. Martin, C. Sauteret, J. L. Paillard, S. Jacquemot, and F. Amiranoff, "Recent progress on LULI high power laser facilities," *J. Phys. Conf. Ser.*, vol. 112, p. 032021, 2008.

[46] J. P. Zou, C. LeBlanc, D. N. Papadopoulos, G. Chériaux, P. Georges, G. Mennerat, F. Druon, L. Lecherbourg, A. Pellegrina, P. Ramirez, F. Giambruno, A. Fréneaux, F. Leconte, D. Badarau, J. M. Boudenne, D. Fournet, T. Valloton, J. L. Paillard, J. L. Veray, M. Pina, P. Monot, J. P. Chambaret, P. Martin, F. Mathieu, P. Auderbert, and F. Amiranoff, "Design and current progress of the Apollon 10 PW project," *High Power Laser Science and Engineering*, vol. 3, p. e2, 2015.

[47] J. J. MacFarlane, I. E. Golovkin, and P. R. Woodruff, "HELOS-CR – a 1-D radiation-magnetohydrodynamics code with inline atomic kinetics modeling," *J. Quant. Spectrosc. Ra.*, vol. 99, no. 1-3, pp. 381–397, 2006.

[48] B. Fryxell, K. Olson, P. Ricker, F. X. Timmes, M. Zingale, D. Q. Lamb, P. MacNeice, R. Rosner, J. W. Truran, and H. Tufo, "FLASH: An Adaptive Mesh Hydrodynamics Code for Modeling Astrophysical Thermonuclear Flashes," *Astrophys. J. Suppl. S.*, vol. 131, no. 1, pp. 273–334, 2000.

[49] R. A. Fonseca, L. O. Silva, F. S. Tsung, V. K. Decyk, W. Lu, C. Ren, W. B. Mori, S. Deng, S. Lee, T. Katsouleas, and J. C. Adam, "OSIRIS: A Three-Dimensional, Fully Relativistic Particle in Cell Code for Modeling Plasma Based Accelerators," *Lect. Notes. Comput. Sci.*, vol. 2231, p. 342, 2002.

[50] T. D. Arber, K. Bennett, C. S. Brady, A. Lawrence-Douglas, M. G. Ramsay, N. J. Sircombe, P. Gillies, R. G. Evans, H. Schmitz, A. R. Bell, and C. P. Ridgers, "Contemporary particle-in-cell approach to laser-plasma modelling," *Plasma Phys. Control. Fusion*, vol. 57, p. 113001, 2015.

[51] S. P. Lyon and J. D. Johnson, "SESAME: The Los Alamos National Laboratory Equation of State Database," *LANL Technical Report LA-UR-92-3407, Los Alamos National Laboratory, Los Alamos, NM*, 1992.

[52] A. Dubey, C. Daley, J. ZuHone, P. M. Ricker, K. Weide, and C. Graziani, "Imposing a Lagrangian particle framework on an Eulerian hydrodynamics infrastructure in FLASH," *Astrophys. J. Suppl. S.*, vol. 201, no. 2, p. 27, 2012.

[53] C. K. Birdsall and A. B. Langdon, *Plasma Physics via Computer Simulation*. McGraw-Hill, 1985.

[54] L. Ceurvorst, A. Savin, N. Ratan, M. F. Kasim, J. Sadler, P. A. Norreys, H. Habara, K. A. Tanaka, S. Zhang, M. S. Wei, S. Ivancic, D. H. Froula,

and W. Theobald, "Channel optimization of high-intensity laser beams in millimeter-scale plasmas," *Phys. Rev. E*, vol. 97, p. 043208, 2018.

[55] R. A. Cairns, R. Bingham, P. Norreys, and R. Trines, "Laminar shocks in high power laser plasma interactions," *Phys. Plasmas*, vol. 21, p. 022112, 2014.

[56] R. A. Cairns, R. Bingham, R. M. G. M. Trines, and P. Norreys, "Weak collisionless shocks in laser-plasmas," *Plasma Phys. Control. Fusion*, vol. 57, p. 044008, 2015.

[57] T. Baeva, S. Gordienko, A. P. L. Robinson, and P. A. Norreys, "The zero vector potential mechanism of attosecond absorption," *Phys. Plasmas*, vol. 18, p. 056702, 2011.

[58] A. F. Savin, A. J. Ross, M. Serzans, R. M. G. M. Trines, L. Ceurvorst, N. Ratan, B. Spiers, R. Bingham, A. P. L. Robinson, and P. A. Norreys, "Attosecond-scale absorption at extreme intensities," *Phys. Plasmas*, vol. 24, p. 113103, 2017.

[59] A. F. Savin, A. J. Ross, R. Aboushelbaya, M. W. Mayr, B. Spiers, R. H.-W. Wang, and P. A. Norreys, "Energy absorption in the laser-QED regime," *Sci. Rep.*, vol. 9, p. 8956, 2019.

[60] V. Yanovsky, V. Chvykov, G. Kalinchenko, P. Rousseau, T. Planchon, T. Matsuoka, A. Maksimchuk, J. Nees, G. Cheriaux, G. Mourou, and K. Krushelnick, "Ultra-high intensity- 300-TW laser at 0.1 Hz repetition rate.," *Opt. Express*, vol. 16, pp. 2109–2114, 2008.

[61] J. Dawson and C. Oberman, "High Frequency Conductivity and the Emission and Absorption Coefficients of a Fully Ionized Plasma," *Phys. Fluids*, vol. 5, no. 5, pp. 517–524, 1962.

[62] C. D. Decker, W. B. Mori, J. M. Dawson, and T. Katsouleas, "Nonlinear collisional absorption in laserdriven plasmas," *Phys. Plasmas*, vol. 1, no. 12, pp. 4043–4049, 1994.

[63] D. W. Forslund, J. M. Kindel, and K. Lee, "Theory of Hot-Electron Spectra at High Laser Intensity," *Phys. Rev. Lett.*, vol. 39, no. 5, 1977.

[64] A. K. Ghatak, R. L. Gallawa, and I. C. Goyal, *Modified Airy Functions and WKB Solutions to the Wave Equation*. Natl. Inst. Stud. Technol. Mono., 1991.

[65] P. Mulser, D. Bauer, and H. Ruhl, "Collisionless Laser-Energy Conversion by Anharmonic Resonance," *Phys. Rev. Lett.*, vol. 101, p. 225002, 2008.

[66] P. Gibbon and A. R. Bell, "Collisionless Absorption in Sharp-Edged Plasmas," *Phys. Rev. Lett.*, vol. 68, no. 10, 1992.

[67] M. Cerchez, R. Jung, J. Osterholz, T. Toncian, O. Willi, P. Mulser, and H. Ruhl, "Absorption of Ultrashort Laser Pulses in Strongly Overdense Targets," *Phys. Rev. Lett.*, vol. 100, p. 245001, 2008.

[68] R. Sauerbury, J. Fure, S. P. LeBlanc, B. van Wonterghem, U. Teubner, and F. P. Schäfer, "Reflectivity of laser-produced plasmas generated by a high intensity ultrashort pulse," *Phys. Plasmas*, vol. 1, no. 5, pp. 1635–1642, 1994.

[69] F. Brunel, "Not-So-Resonant, Resonant Absorption," *Phys. Rev. Lett.*, vol. 59, no. 1, pp. 52–55, 1987.

[70] S. Kato, B. Bhattacharyya, A. Nishiguchi, and K. Mima, "Wave breaking and absorption efficiency for short pulse p-polarized laser light in a very steep density gradient," *Phys. Fluids B-Plasma*, vol. 5, p. 564, 1993.

[71] G. Bonnaud, P. Gibbon, J. Kindel, and E. Williams, "Laser interaction with a sharp-edged overdense plasma," *Laser Part. Beams*, vol. 9, no. 2, pp. 339–354, 1991.

[72] W. L. Kruer and K. Estabrook, "JxB heating by very intense laser light," *Phys. Fluids*, vol. 28, no. 1, pp. 430–432, 1985.

[73] G. Malka and J. L. Miquel, "Experimental Confirmation of Ponderomotive-Force Electrons Produced by an Ultrarelativistic Laser Pulse on a Solid Target," *Phys. Rev. Lett.*, vol. 77, pp. 75–78, 1996.

[74] J. Larmor, "LXIII. On the theory of the magnetic influence on spectra; and on the radiation from moving ions," *Lond. Edinb. Dubl. Phil. Mag.*, vol. 44, no. 271, pp. 503–512, 1897.

[75] U. Teubner and P. Gibbon, "High-order harmonics from laser-irradiated plasma surfaces," *Rev. Mod. Phys.*, vol. 81, pp. 445–479, 2009.

[76] M. Zepf, G. D. Tsakiris, G. Pretzler, I. Watts, D. M. Chambers, P. A. Norreys, U. Andiel, A. E. Dangor, K. Eidmann, C. Gahn, A. Machacek, J. S. Wark, and K. Witte, "Role of the plasma scale length in the harmonic generation from solid targets," *Phys. Rev. E*, vol. 58, pp. R5253–R5256, 1998.

[77] P. A. Norreys, M. Zepf, S. Moustaizis, A. P. Fews, J. Zhang, P. Lee, M. Bakarezos, C. N. Danson, A. Dyson, P. Gibbon, P. Loukakos, D. Neely, F. N. Walsh, J. S. Wark, and A. E. Dangor, "Efficient Extreme UV Harmonics Generated from Picosecond Laser Pulse Interactions with Solid Targets," *Phys. Rev. Lett.*, vol. 276, pp. 1832–1835, 1996.

[78] B. Dromey, M. Zepf, A. Gopal, K. Lancaster, M. S. Wei, K. Krushelnick, M. Tatarakis, N. Vakakis, S. Moustaizis, R. Kodama, M. Tampo, C. Stoeckl,

R. Clarke, H. Habara, D. Neely, S. Karsch, and P. Norreys, "High harmonic generation in the relativistic limit," *Nat. Phys.*, vol. 2, pp. 456–459, 2006.

[79] B. Dromey, S. Kar, C. Bellei, D. C. Carroll, R. J. Clarke, J. S. Green, S. Kneip, K. Markey, S. R. Nagel, P. T. Simpson, L. Willingale, P. McKenna, D. Neely, Z. Najmudin, K. Krushelncik, P. A. Norreys, and M. Zepf, "Bright Multi-keV Harmonic Generation from Relativistically Oscillating Plasma Surfaces," *Phys. Rev. Lett.*, vol. 99, p. 085001, 2007.

[80] T. Baeva, S. Gordienko, and A. Pukhov, "Theory of high-order harmonic generation in relativistic laser interaction with overdense plasma," *Phys. Rev. E*, vol. 75, p. 046404, 2006.

[81] A. Tarasevitch, A. Orisch, D. von der Linde, Ph. Balcou, G. Rey, J.-P. Chambert, U. Teubner, D. Klöpfel, and W. Theobald, "Generation of high-order spatially coherent harmonics from solid targets by femtosecond laser pulses," *Phys. Rev. A*, vol. 62, p. 023816, 2000.

[82] F. Dollar, P. Cummings, V. Chvykov, L. Willingale, M. Vargas, V. Yanovsky, C. Zulick, A. Maksimchuk, A. G. R. Thomas, and K. Krushelnick, "Scaling High-Order Harmonic Generation from Laser-Solid Interactions to Ultrahigh Intensity," *Phys. Rev. Lett.*, vol. 110, p. 175002, 2013.

[83] A. McPherson, G. Gibson, H. Jara, U. Johann, T. S. Luk, I. A. McIntyre, K. Boyer, and C. K. Rhodes, "Studies of multiphoton production of vacuum-ultraviolet radiation in the rare gases," *J. Opt. Soc. Am.*, vol. 4, p. 595, 1987.

[84] M. Ferray, A. L'Hullier, X. F. Li, L. A. Lompre, G. Mainfray, and C. Manus, "Multiple-harmonic conversion of 1064 nm radiation in rare gases," *J. Phys. B: At. Mol. Opt. Phys.*, vol. 21, p. L31, 1988.

[85] P. B. Corkum, "Plasma perspective on strong field multiphoton ionization," *Phys. Rev. Lett.*, vol. 71, p. 1994, 1993.

[86] M. Lewenstein, Ph. Balcou, M. Y. Ivanov, A. L'Hullier, and P. B. Corkum, "Theory of high-harmonic generation by low-frequency laser fields," *Phys. Rev. A*, vol. 49, p. 2117, 1994.

[87] C. Grebogi, V. K. Tripathi, and H. H. Chen, "Harmonic-Generation of Radiation in a Steep Density Profile," *Phys. Fluids*, vol. 26, no. 7, pp. 1904–1908, 1983.

[88] W. Yu, M. Y. Yu, Z. M. Sheng, and J. Zhang, "Model for fast electrons in ultrashort-pulse laser interaction with solid targets," *Phys. Rev. E*, vol. 58, pp. 2456–2460, 1998.

[89] S. V. Bulanov, N. M. Naumova, and F. Pegoraro, "Interaction of an ultrashort, relativistically strong laser pulse with an overdense plasma," *Phys. Plasmas*, vol. 1, no. 3, pp. 745–757, 1994.

[90] R. Lichters, J. Meyer-ter-Vehn, and A. Pukhov, "Short-pulse laser harmonics from oscillating plasma surfaces driven at relativistic intensity," *Phys. Plasmas*, vol. 3, p. 3425, 1996.

[91] S. Gordienko, A. Pukhov, O. Shorokhov, and T. Baeva, "Relativistic Doppler Effect: Universal Spectra and Zeptosecond Pulses," *Phys. Rev. Lett.*, vol. 93, p. 115002, 2004.

[92] C. Thaury, F. Quéré, J.-P. Geindre, A. Levy, T. Ceccotti, P. Monot, M. Bougeard, F. Réau, P. D'Oliveira, P. Audebert, R. Marjoribanks, and Ph. Martin, "Plasma mirrors for ultrahigh-intensity optics," *Nat. Phys.*, vol. 3, pp. 424–429, 2007.

[93] H. Vincenti, S. Monchocé, S. Kahaly, G. Bonnaud, Ph. Martin, and F. Quéré, "Optical properties of relativistic plasma mirrors," *Nat. Commun.*, vol. 5, p. 3403, 2014.

[94] M. Roth, I. Alber, V. Bagnoud, C. R. D. Brown, R. Clarke, H. Daido, J. Fernandez, K. Flippo, S. Gaillard, C. Gauthier, M. Geissel, S. Glenzer, G. Gregori, M. Günther, K. Harres, R. Heathcote, A. Kritcher, N. Kugland, S. LePape, B. Li, M. Makita, J. Mithen, C. Niemann, F. Nürnberg, D. Offermann, A. Otten, A. Pelka, D. Riley, G. Schaumann, M. Schollmeier, J. Schütrumpf, M. Tampo, A. Tauschwitz, and A. Tauschwitz, "Proton acceleration experiments and warm dense matter research using high power lasers," *Plasma Phys. Control. Fusion*, vol. 51, no. 12, p. 124039, 2009.

[95] M. Borghesi, D. H. Campbell, A. Schiavi, M. G. Haines, O. Willi, A. J. MacKinnon, P. Patel, L. A. Gizzi, M. Galimberti, R. J. Clarke, F. Pegoraro, H. Ruhl, and S. Bulanov, "Electric field detection in laser-plasma interaction experiments via the proton imaging technique," *Phys. Plasmas*, vol. 9, p. 2214, 2002.

[96] M. Roth, T. E. Cowan, M. H. Key, S. P. Hatchett, C. Brown, W. Fountain, J. Johnson, D. M. Pennington, R. A. Snavely, S. C. Wilks, K. Yasuike, H. Ruhl, F. Pegoraro, S. V. Bulanov, E. M. Campbell, M. D. Perry, and H. Powell, "Fast Ignition by Intense Laser-Accelerated Proton Beams," *Phys. Rev. Lett.*, vol. 86, p. 436, 2001.

[97] J. C. Fernández, J. J. Honrubia, B. J. Albright, K. Flippo, D. C. Gautier, B. M. Hegelich, M. J. Schmitt, M. Temporal, and L. Yin, "Progress and prospects of ion-driven fast ignition," *Nucl. Fusion*, vol. 49, p. 065004, 2009.

[98] A. Maksimchuk, S. Gu, K. Flippo, D. Umstadter, and V. Y. Bychenkov, "Forward Ion Acceleration in Thin Films Driven by a High-Intensity Laser," *Phys.*

*Rev. Lett.*, vol. 84, p. 18, 2000.

[99] S. C. Wilks, A. B. Langdon, T. E. Cowan, M. Roth, M. Singh, S. Hatchett, M. H. Key, D. Pennington, A. MacKinnon, and R. A. Snavely, "Energetic proton generation in ultra-intense laser-solid interactions," *Phys. Plasmas*, vol. 8, p. 542, 2001.

[100] J. Fuchs, P. Antici, E. D'Humières, E. Lefebvre, M. Borghesi, E. Brambrink, C. A. Cecchetti, M. Kaluza, V. Malka, M. Manclossi, S. Meyroneinc, P. Mora, J. Schreiber, T. Toncian, H. Pépin, and P. Audebert, "Laser-driven proton scaling laws and new paths towards energy increase," *Nat. Phys.*, vol. 2, pp. 48–54, 2006.

[101] A. Yogo, K. Mima, N. Iwata, S. Tosaki, A. Morace, Y. Arikawa, S. Fujioka, T. Johzaki, Y. Sentoku, H. Nishimura, A. Sagisaka, K. Matsuo, N. Kamitsukasa, S. Kojima, H. Nagatomo, M. Nakai, H. Shiraga, M. Murakami, S. Tokita, J. Kawanaka, N. Miyanaga, K. Yamanoi, T. Norimatsu, H. Sakagami, S. V. Bulanov, K. Kondo, and H. Azechi, "Boosting laser-ion acceleration with multi-picosecond pulses," *Sci. Rep.*, vol. 7, p. 42451, 2017.

[102] A. F. A. Bott, C. Graziani, P. Tzeferacos, T. G. White, D. Q. Lamb, G. Gregori, and A. A. Schekochihin, "Proton imaging of stochastic magnetic fields," *J. Plasma Phys.*, vol. 83, no. 6, p. 905830614, 2017.

[103] T. Esirkepov, M. Borghesi, S. V. Bulanov, G. Mourou, and T. Tajima, "Highly Efficient Relativistic-Ion Generation in the Laser-Piston Regime," *Phys. Rev. Lett.*, vol. 92, p. 17, 2004.

[104] G. Marx, "Interstellar Vehicle Propelled by Laser Beam," *Nature*, vol. 211, pp. 22–23, 1966.

[105] A. P. L. Robinson, M. Zepf, S. Kar, R. G. Evans, and C. Bellei, "Radiation pressure acceleration of thin foils with circularly polarized laser pulses," *New J. Phys*, vol. 10, p. 013021, 2008.

[106] A. Henig, S. Steinke, M. Schnürer, T. Sokollik, R. Hörlein, D. Kiefer, D. Jung, J. Schreiber, B. M. Hegelich, X. Q. Yan, J. Meyer-ter-Vehn, T. Tajima, P. V. Nickles, W. Sandner, and D. Habs, "Radiation-Pressure Acceleration of Ion Beams Driven by Circularly Polarized Laser Pulses," *Phys. Rev. Lett.*, vol. 103, p. 245003, 2009.

[107] S. Kar, K. F. Kakolee, B. Qiao, A. Macchi, M. Cerchez, D. Doria, M. Geissler, P. McKenna, D. Neely, J. Osterholz, R. Prasad, K. Quinn, B. Ramakrishna, G. Sarri, O. Willi, X. Y. Yuan, M. Zepf, and M. Borghesi, "Ion Acceleration in Multispecies Targets Driven by Intense Laser Radiation Pressure," *Phys. Rev. Lett.*, vol. 109, p. 185006, 2012.

[108] B. M. Hegelich, B. J. Albright, J. Cobble, K. Flippo, S. Letzring, M. Paffett, H. Ruhl, J. Schreiber, R. K. Schulze, and J. C. Fernández, "Laser acceleration of quasi-monoeneretic MeV ion beams," *Nature*, vol. 439, pp. 441–444, 2006.

[109] F. Fiuza, A. Stockem, E. Boella, R. A. Fonseca, L. O. Silva, D. Haberberger, S. Tochitsky, C. Gong, W. B. Mori, and C. Joshi, "Laser-Driven Shock Acceleration of Monoenergetic Ion Beams," *Phys. Rev. Lett.*, vol. 109, p. 215001, 2012.

[110] A. Stockem, E. Boella, F. Fiuza, and L. O. Silva, "Relativistic generalization of formation and ion-reflection conditions in electrostatic shocks," *Phys. Rev. E*, vol. 87, p. 043116, 2013.

[111] L. Yin, B. J. Albright, B. M. Hegelich, and J. C. Fernandez, "GeV laser ion acceleration from ultrathin targets: The laser break-out afterburner," *Laser Part. Beams*, vol. 24, no. 2, pp. 291–298, 2006.

[112] A. Henig, D. Kiefer, K. Markey, D. C. Gautier, K. A. Flippo, S. Letzring, R. P. Johnson, T. Shimada, L. Yin, B. J. Albright, K. J. Bowers, J. C. Fernández, S. G. Rykovanov, H.-C. Wu, M. Zepf, D. Jung, V. K. Liechtenstein, J. Schreiber, D. Habs, and B. M. Hegelich, "Enhanced Laser-Driven Ion Acceleration in the Relativistic Transparency Regime," *Phys. Rev. Lett.*, vol. 103, p. 045002, 2002.

[113] L. Yin, B. J. Albright, K. J. Bowers, D. Jung, J. C. Fernández, and B. M. Hegelich, "Three-Dimensional Dynamics of Breakout Afterburner Ion Acceleration Using High-Contrast Short-Pulse Laser and Nanoscale Targets," *Phys. Rev. Lett.*, vol. 107, p. 045003, 2011.

[114] O. Buneman, "Excitation of Field Aligned Sound Waves by Electron Streams," *Phys. Rev. Lett.*, vol. 10, pp. 285–287, 1963.

[115] D. T. Farley Jr., "Two-Stream Plasma Instability as a Source of Irregularities in the Ionosphere," *Phys. Rev. Lett.*, vol. 10, pp. 279–282, 1963.

[116] A. Higginson, R. J. Gray, M. King, R. J. Dance, S. D. R. Williamson, N. M. H. Butler, R. Wilson, R. Capdessus, C. Armstrong, J. S. Green, S. J. Hawkes, P. Martin, W. Q. Wei, S. R. Mirfayzi, X. H. Yuan, S. Kar, M. Borghesi, R. J. Clarke, D. Neely, and P. McKenna, "Near-100 MeV protons via laser-driven transparency-enhanced hybrid acceleration scheme," *Nat. Commun.*, vol. 9, no. 724, 2018.

[117] H. Daido, M. Nishiuchi, and A. S. Pirozhkov, "Review of laser-driven ion sources and their applications," *Rep. Prog. Phys.*, vol. 75, p. 056401, 2012.

[118] L. O. Silva, M. Marti, J. R. Davies, R. A. Fonseca, C. Ren, F. S. Tsung, and W. B. Mori, "Proton Shock Acceleration in Laser-Plasma Interactions," *Phys. Rev. Lett.*, vol. 92, p. 015002, 2004.

[119] C. Danson, D. Hillier, N. Hopps, and D. Neely, "Petawatt class lasers worldwide," *High Power Laser Science and Engineering*, vol. 3, p. e3, 2015.

[120] R. Z. Sagdeev, *Reviews of Plasma Physics*. Consultants Bureau, 1966.

[121] S. Betti, F. Ceccherini, F. Cornolti, and F. Pegoraro, "Expansion of a finite-size plasma in vacuum," *Plasma Phys. Control. Fusion*, vol. 47, pp. 521–529, 2005.

[122] P. Mora, "Plasma Expansion into a Vacuum," *Phys. Rev. Lett.*, vol. 90, p. 185002, 2003.

[123] A. M. Bykov and R. A. Treumann, "Fundamentals of collisionless shocks for astrophysical application, 2. Relativistic shocks," *Astron. Astrophys. Rev.*, 2011.

[124] D. W. Forslund and J. P. Freidberg, "Theory of Laminar Collisionless Shocks," *Phys. Rev. Lett.*, vol. 27, no. 18, 1971.

[125] A. M. Steane, *Relativity Made Relatively Easy*. Oxford, United Kingdom: OUP, 2012.

[126] N. Hopps, K. Oades, J. Andrew, C. Brown, G. Cooper, C. Danson, S. Daykin, S. Duffield, R. Edwards, D. Egan, S. Elsmere, S. Gales, M. Girling, E. Gumbrell, E. Harvey, D. Hillier, D. Hoarty, C. Horsfield, S. James, A. Leatherland, S. Masoero, A. Meadowcroft, M. Norman, S. Parker, S. Rothman, M. Rubery, P. Treadwell, D. Winter, and T. Bett, "Comprehensive description of the Orion laser facility," *Plasma Phys. Control. Fusion*, vol. 57, p. 064002, 2015.

[127] B. C. Stuart, J. D. Bonlie, J. A. Britten, J. A. Caird, R. Cross, C. A. Ebbers, M. J. Eckart, A. C. Erlandson, W. A. Molander, A. Ng, P. K. Patel, and

D. F. Price, "The Titan Laser at LLNL," in *Conference on Lasers and Electro-Optics/Quantum Electronics and Laser Science Conference and Photonic Applications Systems Technologies*, p. JTuG3, Optical Society of America, 2006.

[128] A. Casner, T. Caillaud, S. Darbon, A. Duval, I. Thfouin, J. P. Jadaud, J. P. LeBreton, C. Reverdin, B. Rosse, R. Rosch, N. Blanchot, B. Villette, R. Wrobel, and J. L. Miquel, "LMJ/PETAL laser facility: Overview and opportunities for laboratory astrophysics," *High Energ. Den. Phys.*, vol. 17, pp. 2 – 11, 2015.

[129] D. Batani, S. Baton, A. Casner, S. Depierreux, M. Hohenberger, O. Klimo, M. Koenig, C. Labaune, X. Ribeyre, C. Rousseaux, G. Schurtz, W. Theobald, and V. T. Tikhonchuk, "Physics issues for shock ignition," *Nucl. Fusion*, vol. 54, p. 054009, 2014.

[130] J. Meinecke, H. W. Doyle, F. Miniati, A. R. Bell, R. Bingham, R. Crowston, R. P. Drake, M. Fatnejad, M. Koenig, Y. Kuramitsu, C. C. Kuranz, D. Q. Lamb, D. Lee, M. J. MacDonald, C. D. Murphy, H.-S. Park, A. Pelka, A. Ravasio, Y. Sakawa, A. A. Schekochihin, A. Scopatz, P. Tzeferacos, W. C. Wan, N. C. Woolsey, R. Yurchak, B. Reville, and G. Gregori, "Turbulent amplification of magnetic fields in laboratory laser-produced shock waves," *Nat. Phys.*, vol. 10, pp. 520–524, 2014.

[131] P. M. Celliers, D. K. Bradley, G. W. Collins, D. G. Hicks, T. R. Boehly, and W. J. Armstrong, "Line-imaging velocimeter for shock diagnostics at the OMEGA laser facility," *Rev. Sci. Instrum.*, vol. 75, p. 4916, 2004.

[132] A. Grassi, L. Fedeli, A. Sgattoni, and A. Macchi, "Vlasov simulation of laser-driven shock acceleration and ion turbulence," *Plasma Phys. Control. Fusion*, vol. 58, p. 034021, 2016.

[133] D. C. Carroll, P. Brummitt, D. Neely, F. Lindau, O. Lundh, C.-G. Wahlström, and P. McKenna, "A modified Thomson parabola spectrometer for high resolution multi-MeV ion measurements – Application to laser-driven ion acceleration," *Nucl. Instrum. Meth. A*, vol. 620, pp. 23–27, 2010.

[134] K. U. Akli, P. K. Patel, R. Van Maren, R. B. Stephens, M. H. Key, D. P. Higginson, B. Westover, C. D. Chen, A. J. Mackinnon, T. Bartal, F. N. Beg, S. Chawla, R. Fedosejevs, R. R. Freeman, D. S. Hey, G. E. Kemp, S. LePape, A. Link, T. Ma, A. G. MacPhee, H. S. McLean, Y. Ping, Y. Y. Tsui, L. D. Van Woerkom, M. S. Wei, T. Yabuuchi, and S. Yuspeh, "A dual channel X-ray spectrometer for fast ignition research," *J. Instrum.*, vol. 5, p. P07008, 2010.

[135] J. J. MacFarlane, I. Golovkin, P. R. Woodruff, D. R. Welch, B. V. Oliver, T. Mahlhorn, and R. B. Campbell, "Simulation of the ionization dynamics of aluminium irradiated by short-pulse lasers," *Inertial Fusion Sciences and Applications 2003*, pp. 457–460, 2004.

[136] H.-K. Chung, M. H. Chen, W. L. Morgan, Y. Ralchenko, and R. W. Lee, "FLYCHK: Generalized population kinetics and spectral model for rapid spectroscopic analysis for all elements," *High Energ. Den. Phys.*, vol. 1, p. 3, 2005.

[137] S. Gordienko and A. Pukhov, "Scalings for ultrarelativistic laser plasmas and quasimonoenergetic electrons," *Phys. Plasmas*, vol. 12, p. 043109, 2005.

[138] G. Sarri, K. L. lancaster, R. Trines, E. L. Clark, S. Hassan, J. Jiang, N. Kageiwa, N. Lopes, R. Ramis, A. Rehman, X. Ribeyre, C. Russo, R. H. H. Scott, T. Tanimoto, M. Temporal, M. Borghesi, J. R. Davies, Z. Najmudin, K. A. Tanaka, M. Tatarakis, and P. A. Norreys, "Creation of persistent, straight, 2 mm long laser driven chanels in underdense plasmas," *Phys. Plasmas*, vol. 17, p. 113303, 2010.

[139] G. Li, R. Yan, C. Ren, T.-L. Wang, J. Tonge, and W. B. Mori, "Laser Channeling in Millimeter-Scale Underdense Plasmas of Fast-Ignition Targets," *Phys. Rev. Lett.*, vol. 100, p. 125002, 2008.

[140] L. Ceurvorst, N. Ratan, M. C. Levy, M. F. Kasim, J. Sadler, R. H. H. Scott, R. M. G. M. Trines, T. W. Huang, M. Skramic, M. Vranic, L. O. Silva, and P. A. Norreys, "Mitigating the hosing instability in relativistic laser-plasma interactions," *New J. Phys.*, vol. 18, p. 053023, 2016.

[141] Z. Najmudin, K. Krushelnick, M. Tatarakis, E. L. Clark, C. N. Danson, V. Malka, D. Neely, M. I. K. Santala, and A. E. Dangor, "The effect of high intensity laser propagation instabilities on channel formation in underdense plasmas," *Phys. Plasmas*, vol. 10, p. 438, 2003.

[142] G. W. Records, *Guiness World Records 2008*. Jim Pattison Group, 2008.

[143] H. Chen, A. J. Link, R. van Maren, P. K. Patel, R. Shepherd, S. C. Wilks, and P. Beiersdorfer, "High performance compact magnetic spectrometers for energetic ion and electron measurement in ultraintense short pulse laser solid interactions," *Rev. Sci. Instrum.*, vol. 79, p. 10E533, 2008.

[144] A. R. Bell and J. G. Kirk, "Possibility of Prolific Pair Production with High-Power Lasers," *Phys. Rev. Lett.*, vol. 101, p. 200403, 2008.

[145] M. Vranic, T. Grismayer, R. A. Fonseca, and L. O. Silva, "Electron-positron cascades in multiple-laser optical traps," *Plasma Phys. Control. Fus.*, vol. 59, p. 014040, 2017.

[146] T. Grismayer, M. Vranic, J. L. Martins, R. A. Fonseca, and L. O. Silva, "Seeded QED cascades in counterpropagating laser pulses," *Phys. Rev. E*, vol. 95, p. 023120, 2017.

[147] T. G. Blackburn, A. Ilderton, C. D. Murphy, and M. Marklund, "Scaling laws for positron production in laser–electron-beam collisions," *Phys. Rev. A*, vol. 96, p. 022128, 2017.

[148] T. Grismayer, M. Vranic, J. L. Martins, R. A. Fonseca, and L. O. Silva, "Laser absorption via quantum electrodynamics cascades in counter propagating laser pulses," *Phys. Plasmas*, vol. 23, p. 056706, 2016.

[149] P. Zhang, C. P. Ridgers, and A. G. R. Thomas, "The effect of nonlinear quantum electrodynamics on relativistic transparency and laser absorption in ultra-relativistic plasmas," *New J. Phys.*, vol. 17, p. 043051, 2015.

[150] T. V. Liseykina, S. V. Popruzhenko, and A. Macchi, "Inverse Faraday effect driven by radiation friction," *New J. Phys.*, vol. 18, no. 7, p. 072001, 2016.

[151] C. S. Brady, C. P. Ridgers, T. D. Arber, and A. R. Bell, "Synchrotron radiation, pair production, and longitudinal electron motion during 10-100 PW laser solid interactions," *Phys. Plasmas*, vol. 21, no. 3, p. 033108, 2014.

[152] H. A. Lorentz, "La Théorie Électromagnetique de Maxwell et son Application aux Corps Mouvants," *Arch. Neérl.*, vol. 25, p. 363, 1892.

[153] M. Abraham, "Zur Theorie der Strahlung und des Strahlungsdruckes," *Ann. d. Phys.*, vol. 14, p. 236, 1904.

[154] O. Birnholtz, S. Hadar, and B. Kol, "Theory of post-Newtonian radiation and reaction," *Phys. Rev. D*, vol. 88, p. 104037, 2013.

[155] P. A. M. Dirac, "Classical Theory of Radiating Electrons," *Proc. R. Soc. Lon. Ser.-A*, vol. 167, pp. 148–169, 1938.

[156] G. Breit and J. A. Wheeler, "Collision of Two Light Quanta," *Phys. Rev.*, vol. 46, pp. 1087–1091, 1934.

[157] A. I. Titov, B. Kämpfer, H. Takabe, and A. Hosaka, "Breit-Wheeler process in very short electromagnetic pulses," *Phys. Rev. A*, vol. 87, p. 042106, 2013.

[158] C. Bamber, S. J. Boege, T. Koffas, T. Kotseroglou, A. C. Melissinos, D. D. Meyerhofer, D. A. Reis, W. Ragg, C. Bula, K. T. McDonald, E. J. Prebys, D. L. Burke, R. C. Field, G. Horton-Smith, J. E. Spencer, D. Walz, S. C. Berridge, W. M. Bugg, K. Shmakov, and A. W. Weidemann, "Studies of nonlinear QED processes in collisions of 46.6 GeV electrons with intense laser pulses," *Phys. Rev. D*, vol. 60, p. 092004, 1999.

[159] A. Ilderton, "Trident Pair Production in Strong Laser Pulses," *Phys. Rev. Lett.*, vol. 106, p. 020404, 2011.

[160] H. Bether and W. Heitler, "On the Stopping of Fast Particles and on the Creation of Positive Electrons," *Proc. R. Soc. A*, vol. 146, pp. 83–112, 1934.

[161] M. Lobet, X. Davoine, E. d'Humières, and L. Gremillet, "Generation of high-energy electron-positron pairs in the collision of a laser-accelerated electron beam with a multipetawatt laser," *Phys. Rev. Accel. Beams*, vol. 20, p. 043401, 2017.

[162] A. Sgattoni, L. Fedeli, G. Cantono, T. Ceccotti, and A. Macchi, "High field plasmonics and laser-plasma acceleration in solid targets," *Plasma Phys. Control. Fus.*, vol. 58, p. 014004, 2015.

[163] C. P. Ridgers, J. G. Kirk, R. Duclous, T. G. Blackburn, C. S. Brady, K. Bennett, T. D. Arber, and A. R. Bell, "Modelling gamma-ray photon emission and pair production in high-intensity laser-matter interactions," *J. Comp. Phys.*, vol. 260, pp. 273–285, 2014.

[164] V. Yakimenko, S. Meuren, F. Del Gaudio, C. Baumann, A. Fedotov, F. Fiuza, T. Grismayer, M. J. Hogan, A. Pukhov, L. O. Silva, and G. White, "Prospect of

Studying Nonperturbative QED with Beam-Beam Collisions," *Phys. Rev. Lett.*, vol. 122, p. 190404, 2019.

[165] C. McGuffey, M. Dozières, J. Kim, A. Savin, J. Park, J. Emig, C. Brabetz, L. Carlson, R. F. Heeter, H. S. McLean, J. Moody, M. B. Schneider, M. S. Wei, and F. N. Beg, "Soft X-ray backlighter source driven by a short-pulse laser for pump-probe characterization of warm dense matter," *Rev. Sci. Instrum.*, vol. 89, p. 10F122, 2018.

[166] K. V. Cone, J. Dunn, M. B. Schneider, H. A. Baldis, G. V. Brown, J. Emig, D. L. James, M. J. May, J. Park, R. Shepherd, and K. Widmann, "Development of a time-resolved soft x-ray spectrometer for laser produced plasma experiments," *Rev. Sci. Instrum.*, vol. 81, p. 10E318, 2010.

[167] B. Parry, C. J. Hooker, and Y. Tang, "Dual beam operation of the Astra-Gemini high power laser and upgrades to the Ti:Sapphire amplifiers," in *2012 Conference on Lasers and Electro-Optics (CLEO)*, pp. 1–2, 2012.

[168] C. W. Siders, J. K. Crane, M. C. Rushford, L. C. Haefner, J. E. Hernandez, J. W. Dawson, R. J. Beach, W. J. Clark, D. J. Trummer, G. L. Tietbohl, and C. P. J. Barty, "10-kJ Status and 100-kJ Future for NIF PetaWatt Technology," *University of North Texas Libraries, Digital Library; crediting UNT Libraries Government Documents Department*, vol. digital.library.unt.ed/ark:/67531/metadc895083/, p. accessed January 29 2019, 2007.

[169] K. Tietdke, A. Azima, N. von Bargen, L. Bittner, S. Bonfigt, S. Düsterer, B. Faatz, U. Frühling, M. Gensch, Ch. Ferth, N. Guerassimova, U. Hahn, T. Hans, M. Hesse, K. Honkavaar, U. Jastrow, P. Juranic, S. Kapitzki, B. Keitel, T. Kracht, M. Kuhlmann, W. B. Li, M. Martins, T. Núñez, E. Plönjes,

H. Redlin, E. L. Saldin, E. A. Schneidmiller, J. R. Schneider, S. Schreiber, N. Stojanovic, F. Tavella, S. Toleikis, R. Treusch, H. Weigelt, M. Wellhofer, W. Wabnitz, M. V. Yurkov, and J. Feldhaus, "The soft x-ray free-electron laser FLASH at DESY: beamlines, diagnostics and end-stations," *New J. Phys.*, vol. 11, p. 023029, 2009.

[170] W. Luo, W.-Y. Liu, T. Yuan, M. Chen, J.-Y. Yu, F.-Y. Li, D. Del Sorbo, C. P. Ridgers, and Z.-M. Sheng, "QED cascade saturation in extreme high fields," *Sci. Rep.*, vol. 8, p. 8400, 2018.

[171] C. Müller, K. Z. Hatsagortsyan, M. Ruf, S. J. Müller, H. G. Hetzheim, M. C. Koehler, and C. H. Keitel, "Relativistic Nonperturbative Above-Threshold Phenomena in Strong Laser Fields," *Laser Phys.*, vol. 19, pp. 1743–1752, 2009.